



Leibniz Institute
for Solid State and
Materials Research
Dresden



**TECHNISCHE
UNIVERSITÄT
DRESDEN**

Magnetocaloric properties and microstructure of FeRh-based alloys

DISSERTATION

zur Erlangung des akademischen Grades
Doktor rerum naturalium
(Dr. rer. nat.)

vorgelegt

der Fakultät für Mathematik und Naturwissenschaften
der Technischen Universität Dresden

von

Magister der Physik

Alisa Chirkova

1. Gutachter: Prof. Dr. Ludwig Schultz
2. Gutachter: Prof. Dr. Victorino Franco

Eingereicht am: 01.10.2018
Tag der Verteidigung: 19.12.2018

Abstract

The metamagnetic transition from an antiferromagnetic (AF) to the ferromagnetic (FM) state in FeRh alloys and the accompanying magnetocaloric effect (MCE) have been investigated with a particular attention to the sample preparation routes. Direct measurements of the adiabatic temperature change show that the MCE in FeRh remains partly reversible despite the hysteresis and exceeds the effect in the benchmark material Gd by 15 %. The AF–FM transition is strongly affected by the microstructure that is formed depending on the heat treatment parameters. This can explain the discrepancy in the reported data over 80 years of research. The effect on the magnetic properties is found to originate from the interaction of the major α' -phase with the secondary γ -phase that has been typically ignored for its negligible magnetic contribution. The nominal composition of the magnetic α' -phase is found to differ from the actual one for binary and substituted FeRh alloys. The elements can be redistributed within the two phases in such a way, that the actual amount of the doping element in the α' -phase that experiences the AF–FM transition is greatly reduced. This demonstrates the significance of microstructural studies, especially when comparing experimental results with theoretical calculations and developing routes to tune and optimize the magnetocaloric properties of materials.

Kurzfassung

Der metamagnetische Übergang vom antiferromagnetischen (AF) zum ferromagnetischen (FM) Zustand in FeRh-Legierungen und der damit verbundene magnetokalorische Effekt (MCE) wurde untersucht. Ein besonderes Augenmerk lag dabei auf der Probenpräparation. Direkte Messungen der adiabatischen Temperaturänderung zeigten, dass der MCE in FeRh trotz seiner Hysterese teilweise reversibel blieb und das Benchmarkmaterial Gd um 15 % übertrifft. Der AF–FM-Übergang ist stark von der sich bildenden Mikrostruktur, die von den Wärmebehandlungsparametern abhängt, beeinflusst. Dies könnte die Widersprüchlichkeiten in den Forschungsergebnissen der letzten 80 Jahre erklären. Der Einfluss auf den magnetischen Eigenschaften ergibt sich aus der Wechselwirkung zwischen der α' -Hauptphase und der, für gewöhnlich auf Grund ihres vernachlässigbaren magnetischen Einflusses ignorierten, γ -Zweitphase. Es zeigte sich, dass die nominelle Zusammensetzung der magnetischen α' -Phase von der der binären und substituierten FeRh-Legierung abweicht. Die Dotierungselemente können so in den zwei Phasen verteilt werden, dass keine oder nur geringe Mengen der Dotierungselemente in der α' -Phase, die den AF–FM-Übergang erfährt, auftauchen. Dies demonstriert die Notwendigkeit von mikrostrukturellen Untersuchungen, besonders wenn experimentelle Ergebnisse mit theoretischen Berechnungen verglichen und Methoden zur Beeinflussung und Optimierung der magnetokalorischen Eigenschaften entwickelt werden.

CONTENTS

INTRODUCTION	1
1 FUNDAMENTALS	3
1.1 Magnetocaloric effect from basics to materials	3
1.1.1 Thermodynamic approach	3
1.1.2 Magnetocaloric effect at first- and second-order transitions	6
1.1.3 Scaling and universality	8
1.1.4 Magnetic refrigeration	9
1.1.5 Modern magnetocaloric materials	10
1.2 Fe-Rh alloys	13
1.2.1 Phase diagram and crystal structure	13
1.2.2 Specifics of the magnetostructural transition	16
1.2.3 Giant magnetocaloric effect at the transition	22
1.2.4 Strain, deformation and disorder effects	25
1.2.5 Heat treatment effect	30
2 EXPERIMENTAL METHODS	33
2.1 Sample preparation	33
2.1.1 Synthesis and heat treatment	33
2.1.2 Metallographic preparation	34
2.2 Structural characterization	35
2.2.1 Phase identification	35
2.2.2 Determination of the degree of order	36
2.3 Magnetic measurements and calorimetry	37
2.3.1 Quasistatic magnetic field	37
2.3.2 Halbach magnets	38
2.3.3 Pulsed magnetic field	39
2.4 Microscopy	39
2.4.1 Scanning electron microscopy and quantitative analysis	39
2.4.2 Scanning transmission electron microscopy	40
2.4.3 Energy dispersive X-ray spectroscopy	41

2.4.4	Magnetic force microscopy	41
2.5	Modelling	42
3	DIRECT MEASUREMENTS OF THE MAGNETOCALORIC EFFECT	43
3.1	Measurements of binary FeRh under cyclic conditions	43
3.1.1	Structural characterization	43
3.1.2	Evaluation of ΔS from magnetic measurements and calorimetry . .	44
3.1.3	Direct measurements of ΔT_{ad} in the Halbach setup	48
3.2	Dynamics of the magnetocaloric effect in Ni-doped FeRh	52
3.2.1	Structural characterization	52
3.2.2	Dynamical effects evidenced from magnetization measurements . .	53
3.2.3	Evaluation of the MCE from magnetic measurements and calorimetry	59
3.2.4	Direct measurements of ΔT_{ad} in the Halbach setup and in pulsed fields	60
3.3	Conclusions	63
4	EFFECT OF MICROSTRUCTURE ON THE PHASE TRANSITION	65
4.1	Effect of annealing on magnetic properties of Fe ₄₈ Rh ₅₂	65
4.1.1	Shift of magnetostructural transition after heat treatment	65
4.1.2	Microscopy, structural and elemental analysis	67
4.1.3	Modeling of stress fields resulting from heterogeneous microstructure	72
4.2	Thermal history effects in Ni-doped FeRh	75
4.2.1	Suppression of magnetostructural transition after heat treatment .	75
4.2.2	Microscopy, structural and elemental analysis	76
4.2.3	Effects of hydrostatic pressure, tempering and thermal shock	81
4.3	Microstructure of FeRh alloys doped by <i>d</i> -metals	86
4.3.1	Microscopy, structural and elemental analysis	86
4.3.2	Effect on magnetocaloric properties	89
4.4	Conclusions	90
	SUMMARY AND OUTLOOK	91
	BIBLIOGRAPHY	95
	OWN PUBLICATIONS	111
	ACKNOWLEDGMENTS	112

“The art of progress is to preserve order amid change, and to preserve change amid order.”

— Alfred North Whitehead

INTRODUCTION

Magnetic properties of a material depend on the ordering and interaction of its elements. When under certain conditions the type of ordering changes, a magnetic phase transition occurs. There is a vast variety of different magnetic phase transitions that can be generalized into an order-disorder type from a magnetically ordered state to a paramagnetic state, and an order-order type with the change of magnetic structure. These transitions can be accompanied by drastic changes in physical properties, for example, resistivity, magnetization, heat capacity or volume. Such effects are of interest for basic research that reveals the mechanisms behind different magnetic ordering, as well as for the practical use in different technological applications. Magnetic transitions may occur at the change of intensive variables, such as temperature, pressure or magnetic field. A remarkable property of magnetic materials to emit or absorb heat under the action of a magnetic field is called the magnetocaloric effect (MCE). It was discovered in 1917 by P. Weiss and A. Piccard (for a while misleadingly attributed to E. Warburg, as shown in a historical review [1]).

The MCE is intrinsic to all magnetic materials and is due to the coupling of the magnetic sublattice to the magnetic field, which changes the magnetic part of the entropy of a solid [2]. Under adiabatic conditions, as a result of variation of the internal energy of the material, the MCE causes cooling or heating. It promoted an idea of its possible application for efficient refrigeration near room temperature, and the MCE has become a focus of significant research for the past 15 years. Magnetic refrigeration is a rapidly developing technology that is assumed to be capable of competing with and surpassing the conventional vapour-compression refrigeration in terms of efficiency, device volume and ecological impact. The search for new magnetocaloric materials and the optimization of known materials are growing fields of interest, and the new magnetic materials showing a large MCE with narrow hysteresis, particularly near room temperature, are a subject of intensive research activity [3]. Magnetic materials with phase transitions of the second order are beneficial since they show no hysteresis; however, materials with a first order transition can display a higher magnitude of the entropy change. In order to optimize the performance of these materials, detailed studies that help understanding

the nature of magnetic phase transitions are crucial.

FeRh alloys are well-known for the giant adiabatic temperature change $\Delta T_{ad} = -13$ K in 2 T magnetic field [4] that exceeds the values of the MCE in most known materials with a metamagnetic transition. The MCE in FeRh is due to a first order transition of the order-order type, when the magnetic structure changes from antiferromagnetic (AF) to ferromagnetic (FM), while the crystallographic symmetry is preserved [5]. In recent years the study of the AF–FM transition in FeRh has been intensified due to its other potential novel technological applications: a room-temperature AF memory insensitive to strong magnetic fields [6] or an electrically driven AF–FM transition in magnetic storage and spintronics using the magnetoelectric coupling in FeRh/BaTiO₃ [7]. The metamagnetic transition in FeRh is known to be sensitive to a variation of the composition, applied pressure and mechanical treatment. Unfortunately, due to the diverging approaches of materials science and fundamental considerations, the available data have difficulties of comparison, interpretation and reproducibility. The concentration of research mostly on the peculiarities of the AF–FM transition resulted in a deficiency of microstructural studies and a tendency of neglecting of minor phases, despite the re-occurrence of controversial data related to the phase diagram. It would be hard to overestimate the importance of microstructure, considering that it may affect the significant hysteresis accompanying the transition. Until recent it was believed that due to the hysteresis the MCE in FeRh after the first field application is eliminated, making this material useless for practical applications [8].

In this work, the MCE in binary and Ni-doped FeRh has been examined under quasistatic conditions and in a dynamic regime close to that in a potential magnetic refrigerator, including the cyclic field application. Furthermore, the kinetics of the MCE has been investigated through a variation of the magnetic field sweeping rate by several orders of magnitude. The experiments have combined direct measurements of the MCE with the estimation of ΔT_{ad} from the magnetization and heat capacity data. A particular attention has been given to FeRh sample production routes and a comprehensive characterization. During studies of samples with a different thermal history, a connection between magnetic properties and microstructure of the alloys has been discovered. Such factors as temperature, time of annealing and cooling path are shown to affect the phase decomposition in the FeRh-based alloys, strongly influencing the magnetostructural transition and the hysteresis. In FeRh alloys with substitutions by other *d*-metals, the nominal and final compositions of the major phase with the AF–FM transition have been found to vary considerably due to a retained high temperature phase and preferential segregation of the elements in it. This finding may introduce corrections to some suggested models [9]. The discovered effects can be used to tune the transition temperature, the value of the MCE and the hysteresis, that is, the region where the effect is reversible in the materials with a first order transition.

CHAPTER 1

FUNDAMENTALS

This chapter presents the phenomenon of magnetocaloric effect from thermodynamic basics to an overview of modern materials, followed by an introduction to the FeRh system and the features of the metamagnetic transition from an AF state to the FM state.

1.1 Magnetocaloric effect from basics to materials

1.1.1 Thermodynamic approach

Thermodynamics, initially being the study of heat and its potential to generate motion, evolved with time into a theory that describes transformations of states of matter in general. The concept of entropy, a new physical quantity as fundamental and universal as energy, was introduced by Rudolf Clausius. When matter undergoes transformation from one state to another, the total amount of energy in the system and its exterior is conserved; total entropy, however, can only increase or, in idealized cases, remain unchanged. Every process in nature increases the entropy, thus establishing a distinction between the past and the future [10].

A phase transition is an abrupt change in a system that occurs over a small range in a control variable. For thermodynamic phase transitions, typical control variables are the intensive variables of temperature T , pressure p , or magnetic field H [11]. The energy conservation principle can be expressed as $dU = TdS - pdV + \mu_0 HdM$, where the internal energy is a function of entropy, volume and magnetic moment: $U(S, V, M)$. More useful thermodynamic potentials as a function of other parameters are obtained by Legendre transformations [12]. For systems under constant pressure, the Gibbs free energy $G = G(T, p, H)$ is used: $G = U - TS + pV - \mu_0 MH$. Thermodynamic phase transitions in materials and condensed matter occur when there is a singularity in the free energy function of the material, or in one of its derivatives. Changes in some physical properties and the structure of the material accompany the transition, and usually this is

how a phase transition is discovered [11].

Considering the full differential $dG = V dp - S dT - \mu_0 M dH$, entropy S and magnetic moment M can be obtained:

$$dG(T, H, p) = \underbrace{\left(\frac{\partial G}{\partial p}\right)_{H,T}}_V dp + \underbrace{\left(\frac{\partial G}{\partial T}\right)_{H,p}}_{-S} dT + \underbrace{\left(\frac{\partial G}{\partial H}\right)_{T,p}}_{-M} dH \quad (1)$$

From the equality of the second derivatives the Maxwell relations will follow, the one used for an analytical expression for the MCE is:

$$\left(\frac{\partial S}{\partial H}\right)_{T,p} = \mu_0 \left(\frac{\partial M}{\partial T}\right)_{p,H} \quad (2)$$

Entropy can also be considered as a function of the thermodynamic parameters T , H and p , so that $S = S(T, H, p)$. The total differential of the entropy at constant pressure can be written as:

$$dS(T, H)_p = \left(\frac{\partial S}{\partial T}\right)_{H,p} dT + \left(\frac{\partial S}{\partial H}\right)_{T,p} dH \quad (3)$$

Considering adiabatic conditions $dS = 0$ and defining the heat capacity at constant magnetic field from the second law of thermodynamics as $C_{p,H} = T(\partial S/\partial T)_{p,H}$, from (3) with the Maxwell relation (2) applied, follows:

$$dT = -\mu_0 \frac{T}{C_{p,H}} \left(\frac{\partial M}{\partial T}\right)_{p,H} dH \quad (4)$$

Integrating (4), the expression for the total adiabatic temperature change is derived:

$$\Delta T_{ad} = -\mu_0 \int_{H_0}^H \frac{T}{C_{p,H}} \left(\frac{\partial M}{\partial T}\right)_{p,H} dH \quad (5)$$

Also, the MCE can be characterized as a magnetic entropy change due to a magnetic field change in an isothermal process ($dT = 0$). Then, applying the Maxwell relation (2) to (3) as following:

$$dS(T, H)_p = \left(\frac{\partial S}{\partial H}\right)_{T,p} dH = \mu_0 \left(\frac{\partial M}{\partial T}\right)_{p,H} dH \Rightarrow \Delta S_M = \mu_0 \int_{H_0}^H \left(\frac{\partial M}{\partial T}\right)_{p,H} dH \quad (6)$$

In order to use the Maxwell relation, the material should be in thermodynamic equilibrium and magnetization should be a differentiable function of temperature [13, 14]. Strictly speaking, for the first-order materials the Maxwell relation cannot be assumed to be valid, since the magnetization is discontinuous at the transition point, and thus non-differentiable, and there is a non-equilibrium state of two coexisting phases in the hys-

teresis region. However, real first-order materials are never perfectly discontinuous due to the spreading of the transition caused by, e.g., impurities or local non-stoichiometry. The hysteresis can be taken into account depending on the experimental procedure, to avoid appearance of spurious peaks in the entropy change estimated indirectly. Paying attention that the sample under certain conditions is in a mixed state, the Maxwell relation is used very frequently for first-order materials, since magnetization measurements are much easier to perform than direct measurements of the entropy change. Magnetization measurements can be done under isofield and isothermal conditions — $M(T)$ and $M(H)$, respectively. Mainly the isothermal measurements may lead to errors, because at some point the sample will be in a mixed state when the subsequent measurement begins. The errors can be avoided either by applying an experimental routine that avoids sampling the mixed states or by correction of retrieved data extracting equilibrium values for ΔS [14].

A rough estimation of the magnetic entropy change at the magnetization discontinuity associated with the first-order nature of the transition can be done using a magnetic analogue of the Clausius-Clapeyron equation: $|dT/dH| = \mu_0 |\Delta M / \Delta S_M|$. The difference between the entropies of the two phases ΔS is defined through the difference in magnetization before and after the discontinuity ΔM at a given temperature, dH is the shift of critical field with dT . However, the entropy change in this case may be underestimated, since the magnetic entropy change for magnetic fields below and above the critical field of the magnetic discontinuity is not accounted for [13].

Alternatively, ΔS_M can be calculated using temperature dependences of heat capacity in different magnetic fields. The total entropy from (3) at a constant magnetic field ($dH = 0$), correlated to heat capacity $C_{p,H} = T(\partial S / \partial T)_{p,H}$, can be expressed as:

$$S_H(T) = S_0 + \int_0^T \frac{C_{p,H}(T)}{T} dT \quad (7)$$

After the integration of the heat capacity data in different magnetic fields, $S_H(T)$ dependences can be derived and combined into an S - T diagram. From the S - T -diagram, the entropy change ΔS and the adiabatic temperature change ΔT can be obtained [15]. For the adiabatic temperature change the entropy curves have to be inverted.

$$\Delta S_M(T, \Delta H) = [S_H(T) - S_{H_0}(T)]_T; \quad \Delta T_{ad}(T, \Delta H) = [T_H(S) - T_{H_0}(S)]_S \quad (8)$$

The outcome of this procedure is illustrated in Fig. 1.1 for the conventional MCE, typical for many ferromagnets (for example, Gd) transitioning to the paramagnetic state: the applied external magnetic field aligns the magnetic moments, which increases the order in the magnetic system, and the magnetic entropy is decreased (dotted line, Fig. 1.1a). This decrease in entropy is observed under isothermal conditions. Under adiabatic con-

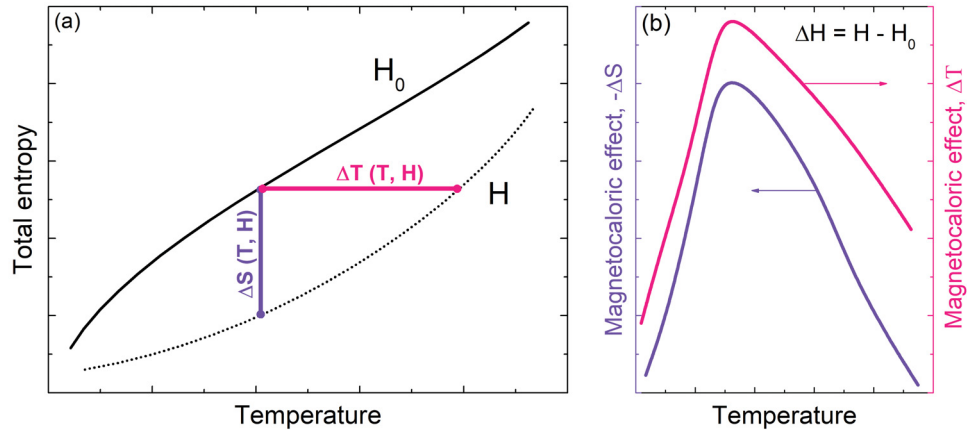


Figure 1.1 (a) Total entropy in the initial H_0 and final H magnetic field, and (b) magnetocaloric effect, ΔS and ΔT in the vicinity of the transition temperature for a ferromagnet with zero coercivity and remanence (adapted from [16]).

ditions, the total entropy stays constant, but the lattice entropy increases in order to compensate the decrease in the magnetic contribution. Therefore, the application of a magnetic field results in a heating of the material. The respective entropy change and adiabatic temperature change are plotted in Fig. 1.1b. In the ordinary MCE the material heats up upon magnetization and cools down upon demagnetization; the corresponding isothermal ΔS is then negative (positive) upon magnetization (demagnetization). In the inverse magnetocaloric effect the material cools down upon magnetization [14].

1.1.2 Magnetocaloric effect at first- and second-order transitions

In a thermodynamic classification, a first-order transition is accompanied by latent heat and a coexistence of the two phases at the transition, while a second-order transition occurs continuously and without latent heat. The general classification of phase transitions, proposed by P. Ehrenfest in 1933, is based on the discontinuities of thermodynamic quantities associated with the first and second derivatives of thermodynamic potentials in the case of first- and second-order transitions, respectively [17]. As the magnetization at a first-order transition changes very rapidly, the MCE (ΔS and ΔT) can reach much higher values than at second-order transitions with the same magnetization values.

First-order transitions often take place at magnetic order-order transitions. The effects of short-range order in the paramagnetic (PM) state and spin fluctuations, which smear magnetic order-disorder transitions, are absent at the first order-order transitions [18]. The order-order magnetic transitions are often accompanied by structural transitions, for example, of the martensitic type, i.e. a diffusionless transition between the two structures. In real systems, impurities and spatial variations in the stoichiometry may blur the first-order/second-order distinction by spreading out the transition and making the first-order transition continuous [14].

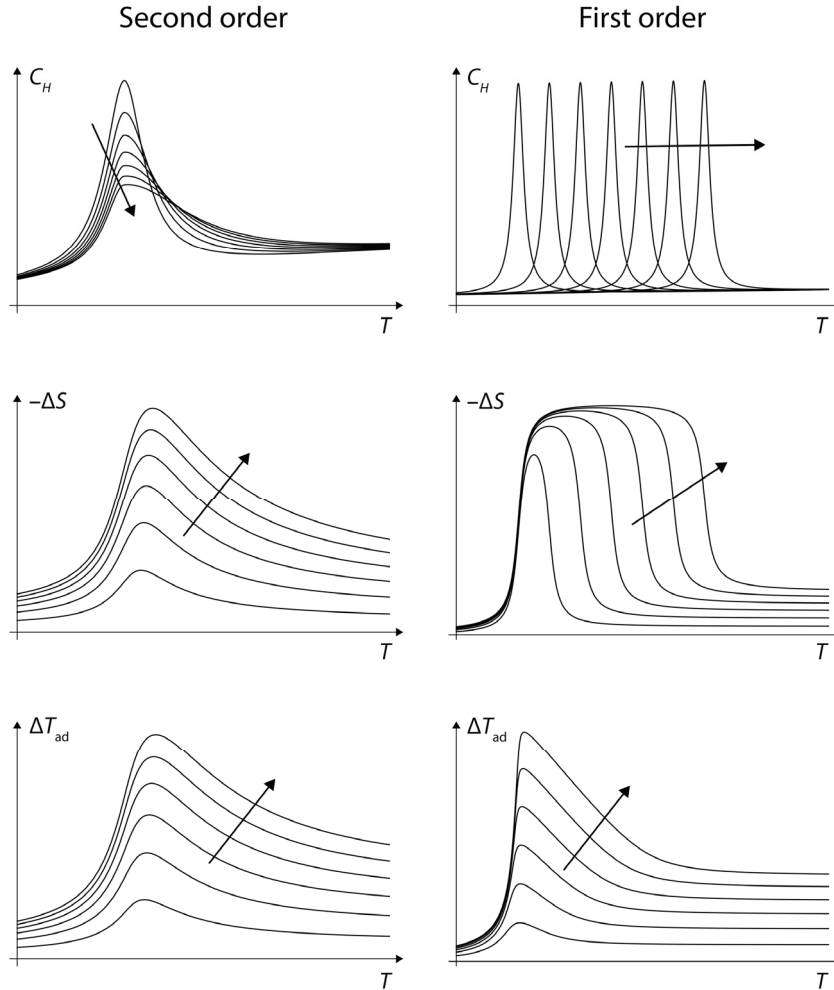


Figure 1.2 Heat capacity, isothermal entropy change and adiabatic temperature change for generic second-order and first-order materials in different external fields in the vicinity of their phase transition; ΔS and ΔT_{ad} have been calculated from the assumed form of C_H , the arrows indicate the direction of increasing H (from [14]).

The general behavior of the thermodynamic values defining the MCE is different in the case of the first- and second-order transitions, but follows particular trends. Modelled generic curves are shown in Fig. 1.2. For second-order materials the specific heat curve has a sharp peak that is lowered and broadened upon increased field, while the peak temperature shifts towards higher temperatures. The curves for ΔS and ΔT increase in height and width, while the peak positions change weakly. For first-order materials, the peak in the specific heat may move significantly with field while the width of the peak hardly increases. From this behavior follows the often observed characteristics of ΔS for a first-order material: the peak height is not very sensitive to the size of the external field while the peak width scales nearly linearly with magnetic field [14].

1.1.3 Scaling and universality

In different external magnetic fields, ΔS_M or ΔT_{ad} of a given material mapped out as a function of temperature, represent a series of curves with roughly similar appearance. Each curve has a peak near the Curie temperature; the peak height, width and temperature depend on the external field. The scaling behavior of these curves has been studied experimentally and theoretically. The construction of a universal curve has a theoretical background which relies on the scaling of second-order phase transitions. Even if the analytical expression of the equation of state is not known for a certain material, a phenomenological procedure allows to construct a universal curve for the MCE by using experimental data [19, 20]: the equivalent points of the $\Delta S_M(T)$ curves measured in different magnetic fields collapse onto the same point of the universal curve (illustrated in Fig. 1.3). This framework has been applied to a large number of materials, including Gd, and Fe-based amorphous alloys [14, 19]. However, the procedure may be affected by the demagnetizing factor that has an influence on the low temperature tails of $\Delta S_M(T)$ [21, 22] or by the existence of minority phases that prevent the construction of the universal curve with a single reference temperature [23].

Although the universal curve relies on the scaling of second order phase transitions, an approximate collapse to a single curve has been observed for a first-order model as well [24]. Moreover, both thermal and magnetic hysteresis of a martensitic transformation were described in terms of an effective temperature [25]. From a theoretical point, the universal curve requires the knowledge of the critical exponents of the material and its equation of state, while the phenomenological procedure can be followed without this *a priori* knowledge. This offers a possibility of different practical applications of the universal curve in the characterization of new materials: from a screening procedure of the performance of materials to corrections for the experimental noise, non-saturating conditions and contribution of magnetic minority phases [19].

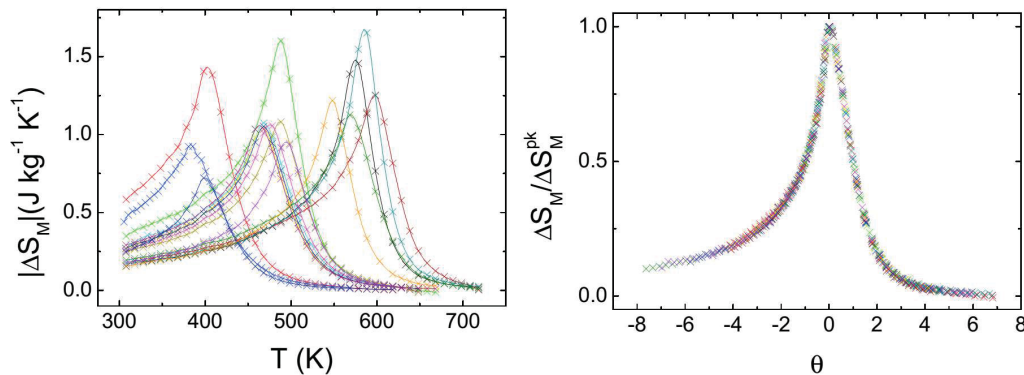


Figure 1.3 Phenomenological universal curve corresponding to experimental results for 16 different Fe-based amorphous alloys (from [19]).

1.1.4 Magnetic refrigeration

The MCE effect can be exploited in order to create a cooling cycle, what gave rise to a new technology known as solid state cooling — an environmentally friendly and efficient alternative to the traditional cooling technology. Magnetic refrigeration is more energetically efficient than the process based on the compression/expansion of gases (60 % vs. 40 % of ideal Carnot efficiency). Depending on the operating temperature, the heat-transfer medium may be water, air or for very low temperatures, helium [26]. Since no refrigerant gases are required for magnetic refrigeration, there is no concern about ozone depletion or greenhouse effect [27].

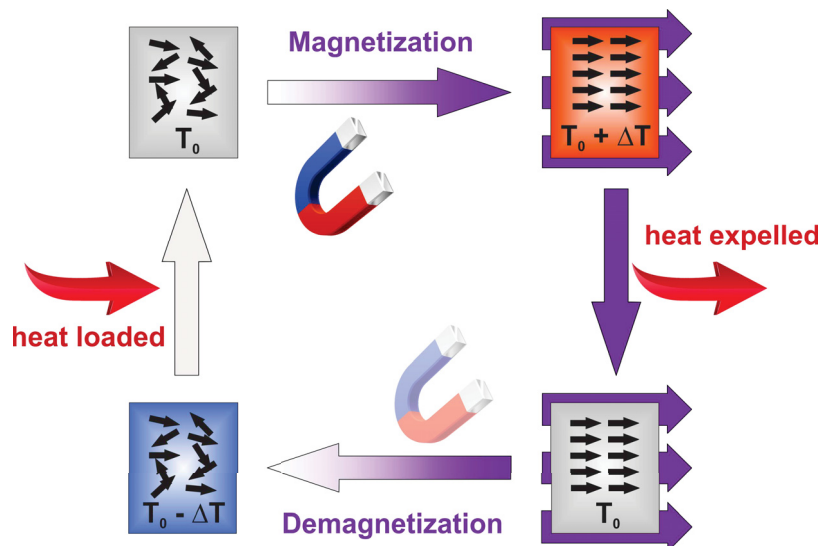


Figure 1.4 A schematic representation of a magnetic refrigeration cycle.

A magnetic refrigeration cycle of a material transforming between paramagnetic and ferromagnetic states is shown schematically in Fig. 1.4. In the absence of the external magnetic field, the magnetic moments are randomly oriented. When a field is applied, the magnetic moments orient parallel to the field, decreasing the entropy associated with the magnetic subsystem. If the magnetization process is performed adiabatically, the decrease in magnetic entropy is compensated by an increase in lattice entropy, resulting in heating of the magnetocaloric material. This heat can be removed from the material to the ambient environment using a heat transfer fluid and the material returns to its initial temperature. Then, during the adiabatic demagnetization process the magnetic entropy of the material increases, decreasing its lattice entropy which leads to cooling of the material below ambient temperature. Heat from the system to be cooled can then be extracted using a heat transfer. Performing these steps in a cycle, a magnetic refrigerator is constructed. It is impossible to separate the refrigerant from the device: a good material implemented poorly is no solution. However, the best material will allow the most headroom for device-centred losses [28].

1.1.5 Modern magnetocaloric materials

In order to develop an optimum material for application in magnetic refrigeration at room temperature, several features are crucial: large ΔS_M and ΔT_{ad} ; low cost of the material and its processing; small specific heat and large thermal conductivity; transition temperature in the vicinity of working temperature; ideally zero magnetic hysteresis to avoid losses for each refrigeration cycle; large spontaneous magnetization with an abrupt drop at the critical temperature; large resistivity to avoid eddy currents; harmless constituents. There are comprehensive reviews of magnetocaloric materials in different temperature ranges [12, 14, 16, 27], also underlining those particularly suitable for magnetic cooling applications. However, even if the material cannot be immediately employed in a magnetic refrigerator, the investigation of its magnetocaloric properties and their fine tuning remains useful for the future applications and a development of magnetic refrigerants.

An efficient magnetocaloric material should have high values of both ΔS and ΔT [28]. The absolute value of the maximum magnetic entropy change in a 5 T magnetic field mapped vs. the transition temperature for the main families of magnetocaloric materials is shown in Fig. 1.5 [27]. The adiabatic temperature change (in 2 T magnetic field) is shown in Fig. 1.6 for some of the most prominent ambient magnetic refrigerants with first- and second-order transitions [29]. At present, Gd remains a benchmark material for testing and using in the prototypes of magnetic refrigerators.

The properties of magnetocaloric materials are sensitive to changes in structure at all scales; from the atomic and nanoscale (exchange interactions) to the microscale (phase content, internal strain and homogeneity) and the macroscale (shape, demagnetization, and pressing) [28]. For example, tuning of the transition temperature and the hystere-

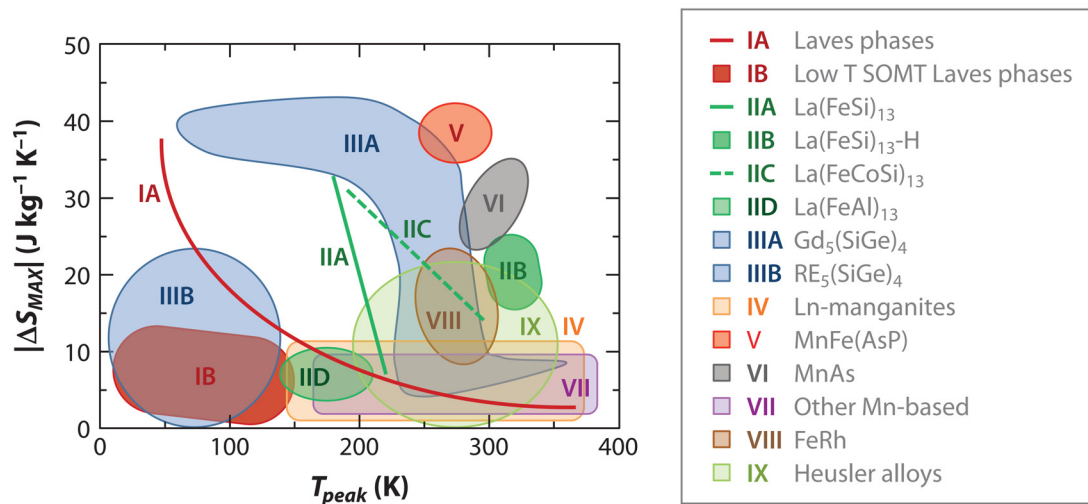


Figure 1.5 Maximum magnetic entropy change for $\mu_0 H = 5$ T vs. peak temperature for different families of magnetocaloric materials (from [27]).

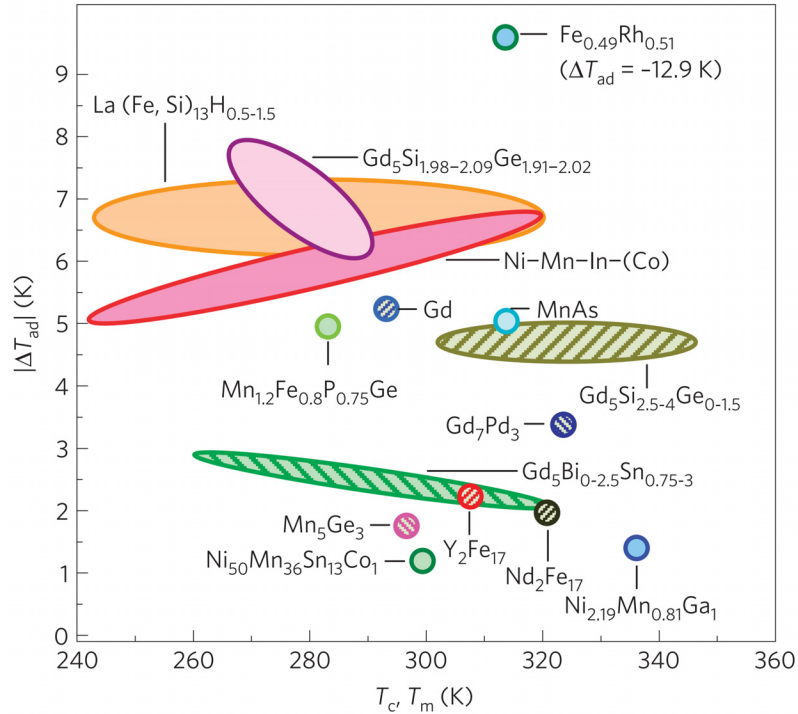


Figure 1.6 Chart of adiabatic temperature change in a 2 T magnetic field for magnetocaloric materials with the first- and second-order transition, marked with a solid fill and a hatched pattern, respectively (from [29]).

sis in $\text{La}(\text{Fe}, \text{Si})_{13}$ can be done using substitution by special elements or hydrogenation [30, 31]. Annealing temperature and time, resulting in different microstructure, influences dramatically the transition temperature, hysteresis and MCE [32]. Furthermore, the MCE of a particular sample can be tailored by controlling the anisotropy of a nanostructured system [33]. The surface morphology is shown to affect the nucleation path of the transition and hysteretic width, diverting or pinning the phase boundary between para- and ferromagnetic regions [34]. Considering reduced dimensions – thin films, melt-spun ribbons or microwires could be promising because of a high surface area to volume ratio, i.e., the geometry which is favorable for the heat transport, but so far the MCE in such materials is inferior to the corresponding bulk materials [35].

An additional problem of materials with a sharp first-order transition is the mechanical stress caused by the volume change, which leads to the occurrence of dislocations and micro-cracks, resulting in pulverization when the material undergoes several thermal or field cycles. This is certainly inconvenient, but still may have an advantage: the smaller fragments require less elastic energy to complete the transformation and, consequently, a reduced hysteresis is observed [3]. Magnetic coupling between adjacent sample fragments can affect the sharpness and the range of transition [36, 37]. There are different ways to produce magnetocaloric materials attempting to avoid mechanical stress and improve the MCE values: for example, placing magnetocaloric particles in an amorphous

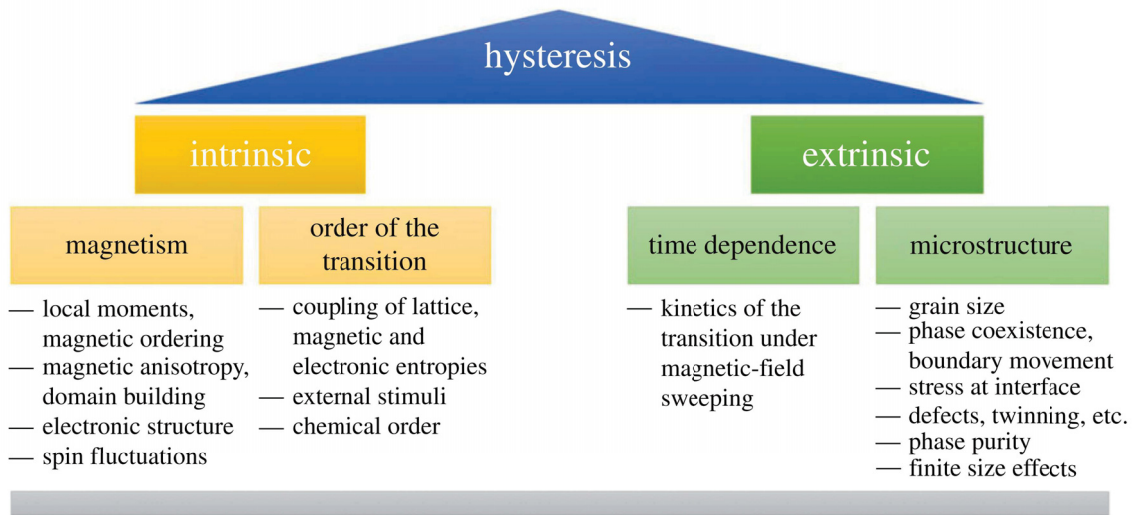


Figure 1.7 Possible intrinsic and extrinsic sources of hysteresis (from [3]).

metallic matrix [38], shaping magnetocaloric wires using powder-in-tube technology [39] or introducing porosity that reduces the hysteresis and prevents degradation after more than 600 temperature-field cycles [40].

The data in the literature are typically given for the first magnetization cycle and, therefore, do not account for the hysteresis in first-order materials. However, the presence of magnetic and thermal hystereses is critical for the refrigeration cycle efficiency. The reversibility of the MCE is mainly affected by the width of the hysteresis when applying and removing a magnetic field. The negative effect of thermal hysteresis can be reduced when following a minor loop of hysteresis instead of completely transforming the material [41]. In order to maximize the efficiency of magnetic cooling devices it is important to understand the mechanisms causing hysteresis. The origin of hysteresis can be from intrinsic (linked to the electronic properties on the atomic scale) and extrinsic influences (related to microstructure) [3], schematically presented in Fig. 1.7. Manipulating different components, it should be possible to affect the hysteresis and obtain an efficient first-order magnetocaloric material under cyclic conditions.

Comparing experimental data to the theoretical limits of $\Delta T_{ad,max}$ and ΔS_{max} for the known refrigerants, it has been found that the first-order materials can indeed provide better properties at a single temperature point than Gd [28]. Metamagnetic antiferromagnets (FeRh, MnGa₃C) are particularly interesting for the development of high performance magnetocaloric materials because they can exhibit a field-induced jump in magnetization that is almost equal to the saturation value. They show highly tunable metamagnetism based on giant magnetoelastic interactions and offer a testing ground for theory, which can predict metamagnetism based upon structural information [28].

1.2 Fe-Rh alloys

1.2.1 Phase diagram and crystal structure

The FeRh phase diagram seems relatively simple and contains cubic iron-like crystal structures. The equiatomic composition attracted attention after the report of a peculiar metamagnetic transformation near room temperature almost 80 years ago [42]. Since then, almost all research on FeRh alloys has been concentrated on that region. After 80 years since the discovery and the number of publications well over 300, the reported phase diagrams [43–50] still have discrepancies and require further studies. The latest version of the Fe-Rh phase diagram (used in Fig. 1.8) has been summarized by Okamoto in 2011 [44]. It has some small differences with the commonly used diagram suggested by Swartzendruber in 1984 [45], especially in the region of the equiatomic composition.

The phase formation process in the region of the equiatomic composition after solidification can be described as follows: the high temperature paramagnetic (PM) face-centered cubic γ -phase (or A1) solidifies approximately at 1600 °C, and transforms at about 1300 °C to an ordered CsCl structure (bcc-B2), or α' -phase. The α' -phase, which is characterized by a superstructure, is ferromagnetic (FM) below 400 °C (Curie tem-

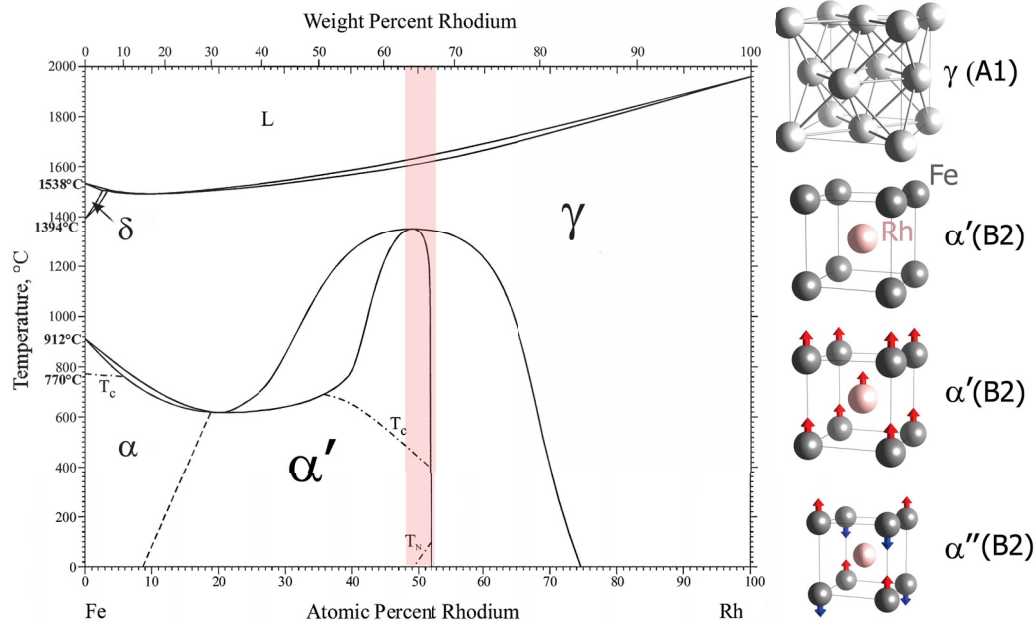


Figure 1.8 Phase diagram of Fe-Rh (after Okamoto, 2011 [44]), the equiatomic region is highlighted. Schematically on the right are shown transformations: from high temperature disordered fcc γ -phase (A1) to paramagnetic CsCl-type α' -phase (bcc-B2) that at 400°C orders ferromagnetically and, near room temperature, experiences a first order magnetostructural transition from the FM state to an AF state with alignment of magnetic moments in the planes of (111) type and 1 % reduction of the unit cell volume.

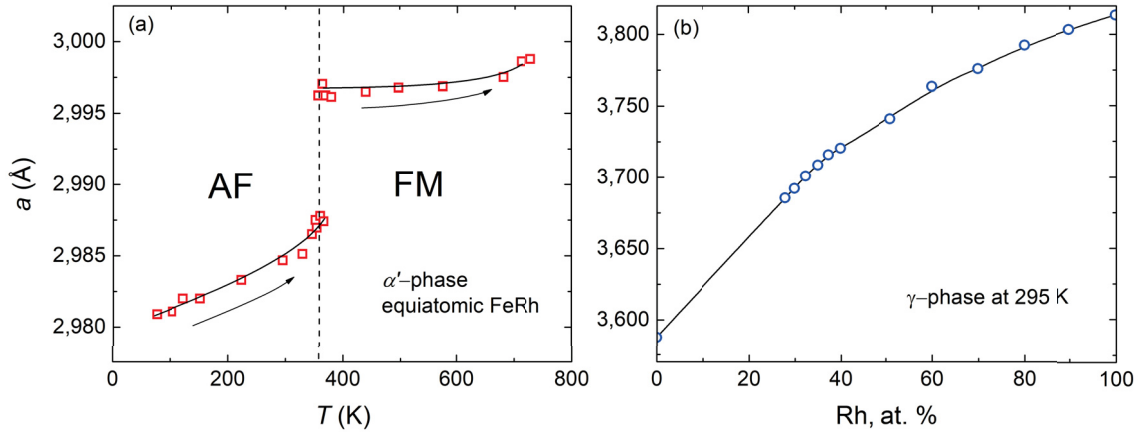


Figure 1.9 (a) Temperature dependence of the lattice parameter of α' -phase measured on heating (after [51]). (b) Dependence of the lattice parameter of γ -phase on Rh content (after [43]).

perature). It transforms by a first-order transition to the antiferromagnetic (AF) phase α'' with the same CsCl crystal structure, but a smaller volume of the unit cell by $\sim 1\%$. The jump in the lattice parameter occurring on heating for the α' -phase is shown in Fig. 1.9a, also the thermal expansion has been measured by the same authors [51]. The transition is accompanied by strong tetragonal distortions in the region of the two phase coexistence [52]. The lattice parameter of the high-temperature γ -phase is shown for the whole composition range in Fig. 1.9b, it increases with the Rh content.

Although the crystal symmetry remains the same, the magnetic structure changes from FM to an AF type-II with an antiferromagnetic coupling between successive layers of (111) iron planes. The magnetic moments were defined experimentally from neutron diffraction [53–55] and were calculated theoretically [56–58]: in the AF state the Fe-moment is $3.3 \mu_B$, whereas Rh is nonmagnetic; in the FM state the Fe-moment remains practically the same ($3.1\text{--}3.2 \mu_B$), the Rh moment, however, is about $1.0 \mu_B$.

There is a certain deficiency in detailed studies of the FeRh phase diagram, as well as of the microstructural aspects and phase formation processes. The existing phase diagrams,

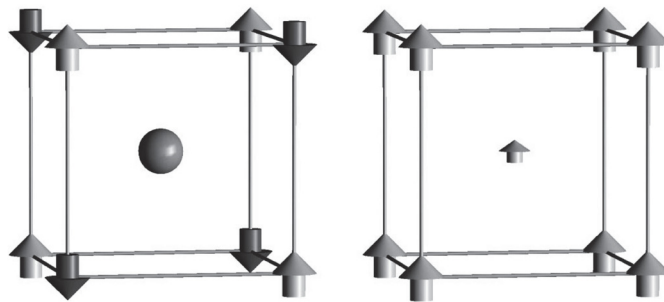


Figure 1.10 Magnetic structure in the AF (nonmagnetic Rh atom in the center and Fe moments of $3.3 \mu_B$ in the corners) and FM (Fe moments of $3.2 \mu_B$ in the corners and Rh moment of $0.9 \mu_B$ in the center) states [56].

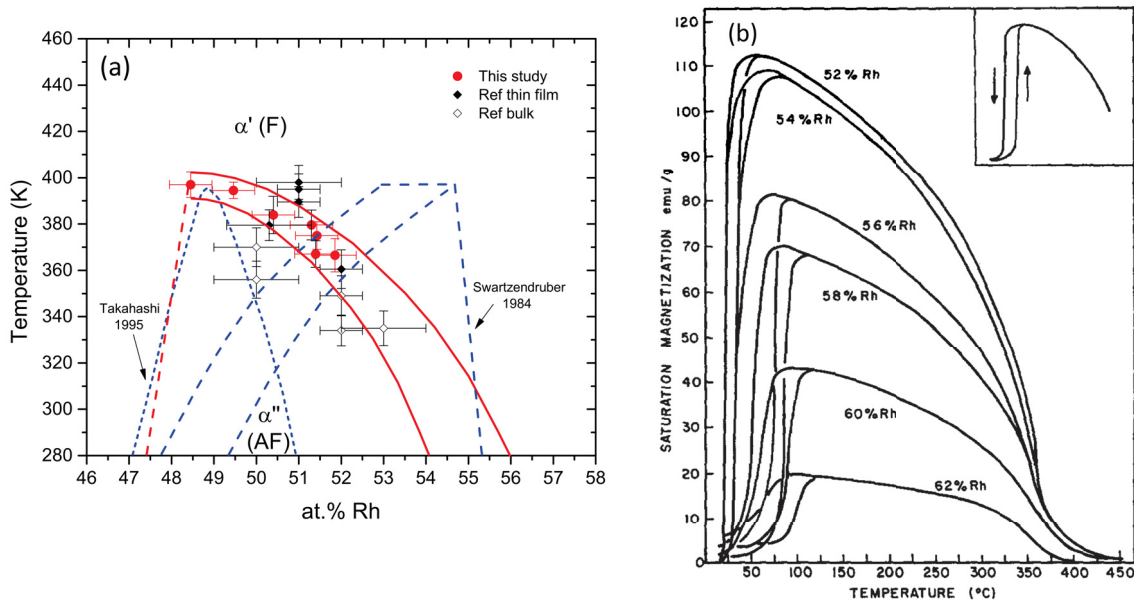


Figure 1.11 (a) Controversy of the FeRh phase diagram: solid red lines are based on experimental measurements of single crystal thin films [49], blue lines represent existing phase diagrams of 1984 ([45], dashed line) and 1995 ([46], dotted line) (b) Temperature dependences of magnetization of Rh-rich FeRh alloys.

being qualitatively alike, have controversial data in the small region of the AF α'' -phase (illustrated in Fig. 1.11a). This problem is indicated from time to time in the literature, e.g. precipitates of γ -phase have been reported to appear in equiatomic FeRh during the annealing process at high temperatures, which invoked a suggestion for a correction of the phase diagram [46]. In thin films, the presence of a spurious fcc γ -phase was observed by the same extra-reflections in all the films involved in the experiment, yet being close to equiatomic composition [59]. The authors note that the γ -phase is known to be paramagnetic and thus should not contribute to the magnetic transition, nor was it obstructing a very high quality order in all films or the AF–FM transition. However, the presence of this phase in precipitates throughout the films should induce both structural and compositional inhomogeneities, eventually accompanied by stress.

Furthermore, a systematic study of bulk Rh-rich alloys with the composition varied from 52 to 62 % Rh [60], revealed the AF–FM transition in all alloys with a reduction of saturation magnetization and an increase of thermal hysteresis (see Fig. 1.11b). A pure paramagnetic state was found only for the alloy with 64 % Rh. In the rest of the studied alloys, a mixture of a γ -phase and a fully ordered α' -phase was detected, while the lattice parameters of both phases were found to be the same.

When the data are retrieved from thin films, the film/substrate interaction and the production techniques can add more complications to the problem of the phase diagram clarification.

1.2.2 Specifics of the magnetostructural transition

The magnetostructural transition from the AF to the FM state in FeRh is detected by a drastic change in several physical properties: a magnetization increase by $130 \text{ A} \cdot \text{m}^2/\text{kg}$ and a resistivity drop [61]. First, a strong dependence of the magnetostructural transition properties on the composition was observed for the binary alloys diverging from the equiatomic composition [60, 62–64]. Then, it has been found that substitution by other d -metals can shift the transition temperature T_{tr} by hundred degrees (Fig. 1.12) and change the magnetization and resistivity values, as well as the hysteresis width [65–69]. The substitution effect can be utilized to tune the AF–FM transition towards the desired range of temperature and magnetic fields: replacing about 5 % of Rh atoms with Ir is applied to raise T_{tr} to 450–500 K for spin-valves applications [70], whereas in many experiments due to equipment limitations the transition should be below room temperature, which is achieved with Ni- or Pd-doping [69]. Substitution by various d -elements mostly affects the temperature of the AF–FM transformation, while the Curie temperature of the FM–PM transition changes only slightly [68, 69]. Summarizing, a few atomic per cent of Pt, Ir, Au, Ru or Os move the onset of the AF–FM transition to higher temperatures, while doping with Pd, Ni, Co and Cu is found to reduce T_{tr} [71].

It has been observed that $3d$ -elements decrease the FeRh transition temperature, while $5d$ -elements increase it, with no unique trend for $4d$ -elements [9, 68]. An attempt to correlate the AF–FM transition temperature and the average weighted valence band electron concentration ($(s + d)$ electrons/atom) has led to the development of an empirical model based on phenomenological grounds that should predict the influence of elemental substitution on the magnetostructural response of FeRh-based ternary alloys (see Fig. 1.13). However, the parameter e_v/atom (valence electron concentration) is

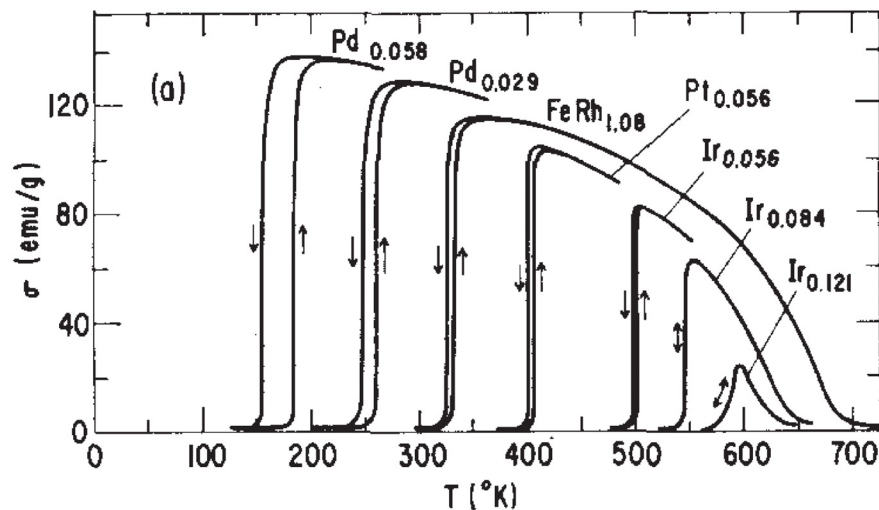


Figure 1.12 Magnetization of $\text{Fe}(\text{Rh}_{1-x}\text{M}_x)_{1.08}$ in 0.7 T field, where M is Pd, Pt or Ir [65].

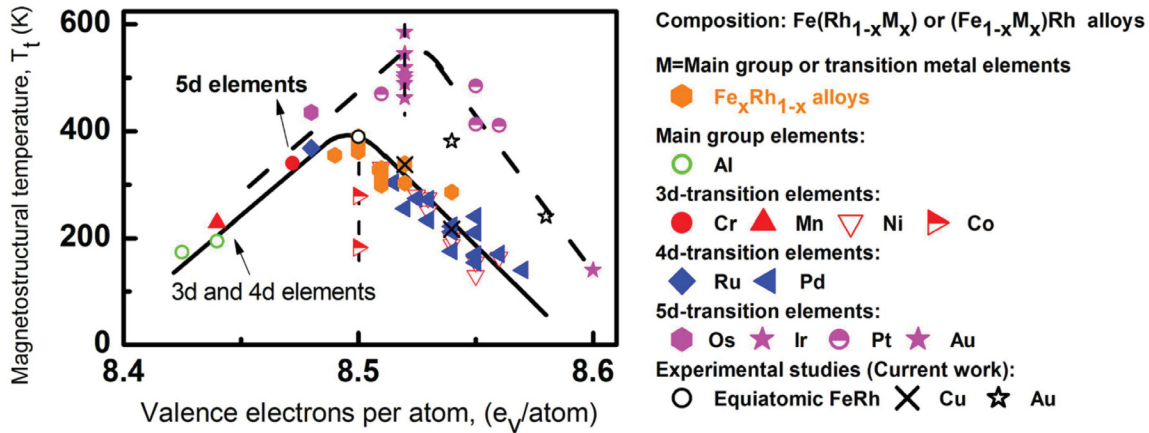


Figure 1.13 Zero-field normalized magnetostructural transition temperature vs. the average weighted valence band electrons ((s + d) electrons/atom) of FeRh-based ternary alloys [9].

suggested only as a guideline, since, as can be seen from Fig. 1.13, in the case of isoelectronic compounds obtained by substituting Rh for Co or Ir this parameter is the same, but AF–FM transition temperatures vary considerably [9]. Compared to the results of calculations of the electron density of states (DOS) at the Fermi level, the model is claimed to be consistent with the addition of electrons to the AF bonding states of a spin-split conduction band that reaches a stability maximum around 8.50 electrons per atom [9].

The effect of very small variations from complete B2 order and stoichiometry was studied from a theoretical point of view in several works [72–75]. First, it was revealed that an Fe impurity substituted for Rh creates a perturbation extending at least to the nearest neighbours of the impurity, and a total ferromagnetic moment close to $3.5 \mu_B$, whereas a Rh impurity substituted for Fe has a localized and less important effect [72]. Then, an *ab initio* DFT-based theory for materials with quenched static compositional disorder was found to account quantitatively for the strong effect of disorder on the AF–FM transition: a presence of just 2 % of Fe antisites, i.e., Fe atoms occupying a very small proportion of the Rh sublattice sites, results in a drop of T_{tr} by 290 K, whereas the calculated value of T_{tr} is 495 K [73]. Furthermore, the influence of impurities on the stability of AF and FM phases was investigated *via* first-principles total energy DFT calculations and Monte Carlo simulations [75]. Two competing effects of the temperature induced magnetic disorder were discovered: 1) a decrease of the magnetic moment induced on Rh that is responsible for the stabilization of the FM state *via* Fe-(Rh)-Fe FM exchange interactions 2) a decrease of the AF Fe-Fe exchange interactions. Suppressing the interplay of these effects leads to a shift of the point of metamagnetic transition in FeRh systems with with 1 at. % and 2 at. % substitution of Rh by Fe atoms (Fig. 1.14a). The presence of Ni impurities, due to the difference in the Fe-Ni compared to Fe-Fe exchange interactions, results in the stabilization of the FM state, and, as a consequence, to a decrease of the

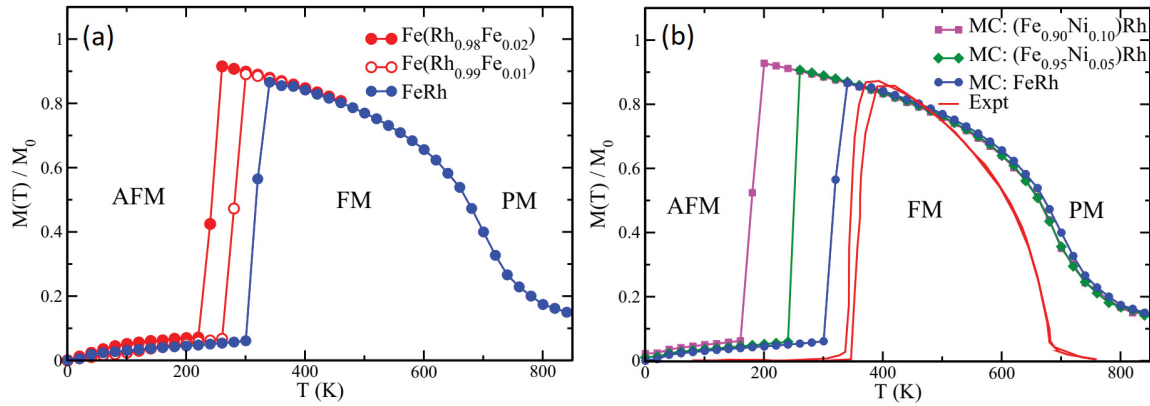


Figure 1.14 Temperature dependent relative magnetization $M(T)/M_0$ (M_0 is the magnetization at $T = 0$ K) obtained within the Monte-Carlo-simulations: (a) for FeRh with 1 at. % and 2 at. % of Fe in the Rh sublattice, in comparison with the results for the equiatomic FeRh; (b) for pure FeRh (circles, red solid line is the experimental result); for FeRh with 5 at. % (diamonds) and 10 at. % (squares) substitution of Fe by Ni atoms (from [75]).

AF–FM transition temperature: for 5 at. % and 10 at. % substitution of Fe by Ni atoms, $T_{tr} = 230$ and 180 K, respectively (Fig. 1.14b).

Quench disorder is thought to result in a local distribution of T_{tr} , which can be the cause of heterogeneous nucleation and growth of the new magnetic phase [76]. Some studies of the kinetics of the AF–FM transition by magnetic relaxation were performed on FeRh modified with a few at. % of Ni [77–79]. It is suggested that in the AF matrix there is a nucleation of FM clusters with a long-range dipolar interaction [78], which is supported by the coexistence of microscopic FM domains and areas that are still AF, their relative size changing with temperature, indicated from the studies of spin and orbital moments over the transition region [80]. Both temperature and field driven transitions are found to follow similar kinetics and have a close resemblance to the nucleation and growth behaviour typical for the crystallization of solids [78]. Furthermore, a combination of two types of relaxation processes can be observed: crystallization-like dynamics and viscous slowdown or glassy dynamics of the metamagnetic transition at low temperature [79]. A crossover from nucleation to growth, coinciding with a rapid increase of the arrested (glassy) fraction possibly results from the disorder influenced nature of the AF–FM transition. The observed magnetic viscosity has been attributed to the existence of the interfaces between the coexisting AF and FM phases, and their mobility [77, 79]. Similar conclusion has been reached for Pd-doped FeRh, considering the FM state at low temperature as glass-like arrested state that experiences devitrification with increasing temperature [76, 81].

Broadening of the hysteresis towards lower temperatures is systematically observed in substituted FeRh-type alloys [69, 81]. Although the non-monotonic variation in the

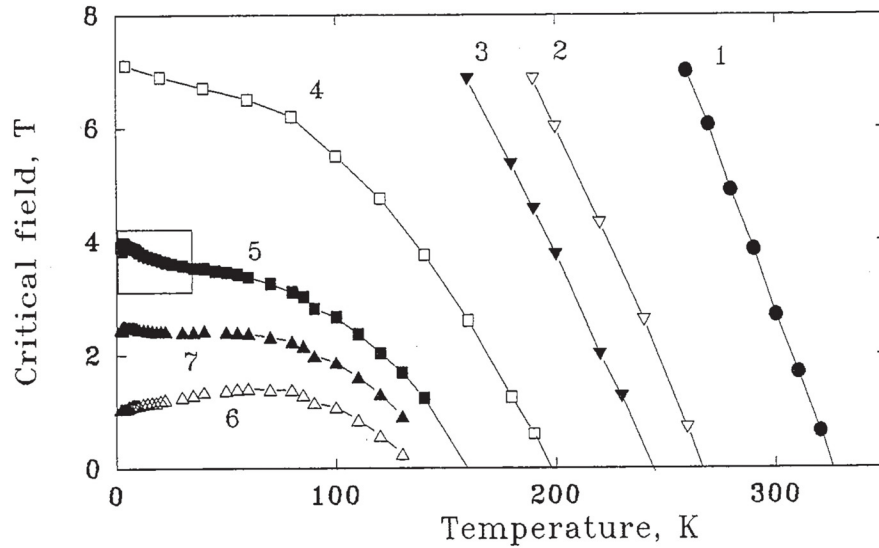


Figure 1.15 Temperature dependences of the critical fields H_c^\uparrow for $(\text{Fe}_{1-x}\text{Ni}_x)_{49}\text{Rh}_{51}$, 1: $x = 0$, 2: $x = 0.0125$, 3: $x = 0.0175$, 4: $x = 0.025$, 5: $x = 0.035$ and H_c^\downarrow , 6: $x = 0.035$ from [69].

critical field (see Fig. 1.15) can be addressed in terms of an interplay between transformation kinetics and supercooling [76, 78, 79, 81], the temperature dependence of the critical field is mostly considered to be quadratic [69, 82, 83]. Initially measured over the limited range of applied magnetic fields, the FM state in FeRh-alloys revealed an approximately linear T_{tr} shift, stabilizing at lower temperatures [51, 84]. However, experiments in pulsed magnetic fields up to 28-30 T [82, 83] established that the critical field depends on temperature roughly as T^2 : $H_c = H_0[1 - (T/T_0)^2]$, what is often observed in systems with itinerant magnetism and may be typical for first-order magnetic phase transitions of electronic origin [85]. This is also supported theoretically [86]. Only at low temperatures below 5 K, the behaviour of the critical field and hysteresis width becomes peculiar: the values deviate from the quadratic dependence and start fluctuating around some average value, as shown for Ni- and Pd-substituted FeRh [69, 87].

Many aspects of the nature and mechanism of the transition still remain under debate, in particular, the energy transfer between lattice, electron and spin subsystems and the complex interplay of their dynamics. The spin dynamics of the metamagnetic transition can be probed experimentally using femtosecond optical laser pulses that drive a material through the AF–FM transition by ultrafast generation of the FM order [88–93]. One suggestion is that the phase transformation is accompanied, but not driven, by a lattice expansion; the mechanism is attributed to the strong FM exchange *via* Rh moments induced by Fe spin fluctuations [89]. However, from time-resolved x-ray spectroscopy upon fs laser excitation, a lattice-driven magnetic phase transition was proposed [91]. Different techniques may provide a different view on the laser-induced magnetization dynamics: one can be sensitive to the perpendicular component of the vectorial aver-

age of magnetization while another one to the magnitude of magnetization only [90]. Therefore, the contradictory conclusions on the magnetic dynamics can be related to the different experimental techniques and their limited temporal resolution or differences in the sample structure, leaving the experimental proof of the driving force of the transition insufficient. In terms of the time scale, a rapid growth of magnetic moment within at most 10 ps is found to be followed by a gradual alignment of local magnetic moments in about 50 ps [90]. A direct observation of the AF–FM phase coexistence finds two intrinsic time scales: one for the initial nucleation of FM domains which is the same for both magnetic and structural dynamics (30 ps), and a second for the subsequent growth of FM domains (60 ps) [93]. By theoretical simulations, a FM response on a picosecond time scale was obtained (20 ps); the speed of the phase transition is likely to be faster than magnetovolume effects [94]. Time-resolved XRD shows that the structural changes associated with the magnetic phase transition are relatively slow and occur on a hundred picosecond time scale [92]. This is supported by a suggestion for the AF–FM-transition be driven by the electron system on a time scale similar to that observed for the loss of magnetization in simple FM materials, followed by a slower phonon-driven lattice expansion [88]. Although, it may just be that the magnetic and structural nucleations go hand in hand rather than one driving the other [93].

The binary metallic compound FeRh can be considered as a naturally occurring magnetic multilayer structure in which the coupling across the magnetically inactive layers can be switched from AF to FM by an applied magnetic field, the AF coupling resulting in high electrical resistance [57, 95]. First-principles DFT-based calculations demonstrate that the pronounced drop in resistivity at the AF–FM transition can be attributed partially to the difference in the electronic structure at the Fermi level of the FM and AF states, as well as to a thermally induced magnetic disorder (spin fluctuations) [96]. The reconstruction of the Fermi surface across the AF–FM transition may occur due to two factors: reduction of the area of the Fermi surface and a smaller Fermi velocity resulting from the superzone gap formation [97].

The electronic band structure of FeRh in its three magnetic phases is essentially dominated by the electrons of *d*-character, the contribution of the *s* and *p* electrons always being weak. The change of the electron DOS at the Fermi level is suggested due to a halving of the magnetic Brillouin zone on passing from the FM to the AF state and the change of magnetic symmetry [86]. The low DOS value for the AF phase and an appearance of a magnetic moment at the rhodium ions in the FM state occur due to splitting of a Rh *d*-subband by a resultant magnetic moment of the iron sublattice [67, 82, 98]. Significant electronic structure changes between the AF and FM states were observed experimentally across the entire valence-band spectrum via hard X-Ray photoemission in epitaxial FeRh thin films and were well reproduced using first-principles density functional theory (DFT) calculations [99].

Remarkable magnetotransport properties indicate the itinerant-electron metamagnetism in FeRh: it is experimentally observed that the transition is accompanied by a giant magnetoresistance (MR) effect $\Delta R/R = 80\text{-}85\%$ in binary FeRh [64, 100, 101], supported also by theoretical calculations [102]. The large MR at low temperature indicates that FeRh in the AF phase has a peculiar Fermi surface structure, suggesting the character of a semimetal [64] and signifies intrinsic spin-dependent scattering processes (e.g., electron-phonon and electron-magnon scattering) [101]. Minor deviations from stoichiometry affect the GMR values [64], as well as the electronic specific heat coefficient γ , especially when Fe and Rh are substituted by other d elements (Ni, Pd, Pt, Ir, Ru) [69, 103].

Measurements of γ allow to determine the value of the DOS at the Fermi surface. It has been reported to be significantly lower in the AF state, associated with the field-induced AF–FM transition, as well as as for the concentration dependent AF–FM transition [104]. This is also in agreement with $\Delta\gamma$ obtained from the analysis of the magnetization curves in FeRh alloys [69, 83], and theoretical calculations [98]. Therefore, the electron entropy was suggested as the main driving force for the transition [67]. However, there have been some concerns whether the off-stoichiometric FeRh in AF or FM state can be compared [64, 83]. The influence of chemical composition can be observed from measurements of low temperature specific heat of substituted FeRh: a few per cent of Ir increased it by an order of magnitude [63, 105]. The nature of the excess entropy of the FM phase over that of the AF phase was thought to arise from itinerant electrons associated with the moment on the Rh atoms [82]. Indeed, a linear dependence of magnetic entropy on temperature has been reported in many works [83, 106–108], which can be an indication of a significant contribution from the electronic subsystem. A phenomenological model attempts to relate the valence band electron concentration and the magnetic entropy change of $3d$ - and $4d$ -substituted FeRh compounds [107]. However, there are suggestions that the electronic contribution is, on the contrary, small and the entropy difference at the transition is dominated by magnetic fluctuations [58, 109].

The very first attempt to explain the nature of the AF–FM transition in FeRh used the exchange inversion model [110] based on the assumption that the sign of the exchange integral changes at a critical value of the lattice parameter, driven by the experimental evidence of the unit cell volume change of 1 % at the metamagnetic transition [51, 111]. However, serious numerical discrepancies were found: the lattice entropy from this model was significantly lower than the experimentally estimated value of the entropy change [65]. Eventually, the model was ruled out as acceptable [62, 82, 112]. Still, the volume-dependent interactions should not be completely discarded. Based on *ab initio* total energy calculations, a realistic description of the experimental magneto-volume effects in FeRh was done using a spin-based model that included distance dependent exchange parameters [56]. Thermal fluctuations of the Rh magnetic moments

provide the entropic stabilization of the FM phase, and the metamagnetic transition can be explained by a competition between AF Fe-Fe and FM Fe-Rh exchange interactions. The AF and FM states in FeRh are close in energy due to a strong compensation at a certain crystal volume of the different volume dependencies: the FM Fe-Rh exchange interaction is robust with respect to the crystal volume variation, whereas the AF Fe-Fe exchange interaction is strongly volume dependent [113]. The entropy associated with the lattice should be larger in the AF phase than in the FM one, due to the fact that the AF phase is elastically softer than the FM one, as found experimentally and theoretically [109, 114, 115]. The lattice vibration contribution is found to act so as to prevent the transition from taking place [86, 109]. Further theoretical advance suggested an equally important role for the magnetic and volume fluctuations as driving forces for the AF–FM transition [116]. Then, a combined *ab initio* and experimental approach allowed an independent assessment of vibrational contributions to specific heat and entropy, and essentially equal contribution of the magnetic and the combined electronic and vibrational degrees of freedom was proposed [117].

Although the discussions continue, it is accepted that the AF–FM transition in FeRh is driven by an excess of electronic and magnetic entropy while the lattice opposes the transition; in terms of different contributions to the entropy change, roughly speaking, $\Delta S_{lat} \simeq -70\%$ of ΔS_{mag} , and ΔS_{el} represents 40% of the total ΔS [118]. Regardless of its debatable origin, the experimentally observed value of the MCE in FeRh is one of the largest compared to other materials [28, 29]. Moreover, the experimental values of ΔS and ΔT_{ad} close to the theoretical limits [28] set FeRh apart from other alloys.

1.2.3 Giant magnetocaloric effect at the transition

The giant magnetocaloric effect of -12.9 K in 1.95 T near room temperature in $\text{Fe}_{49}\text{Rh}_{51}$ was experimentally observed in 1990 [4], a few years before the discovery of the giant MCE in $\text{Gd}_5(\text{Si}_x\text{Ge}_{1-x})_4$ alloys [119, 120] that has launched the solid state refrigeration research. Since the MCE in FeRh exceeded that of most known materials, especially near room temperature, it was originally suggested as a potential working material for magnetic refrigeration [121]. Then, it was assumed that the giant MCE in FeRh is irreversible and observed only upon the first application of the magnetic field [2], so in the following years FeRh attracted little attention for cooling applications. Due to the present high cost of raw materials it is unlikely that FeRh will be used as a commercial magnetic refrigerant, if only in micromagnetic applications in the form of thin films or nanoparticles [122]. Nowadays, FeRh is rather exploited as a model material for understanding of the first order metamagnetic phase transition, which should accelerate the development of novel, high performance magnetocaloric materials for solid state refrigeration near room temperature.

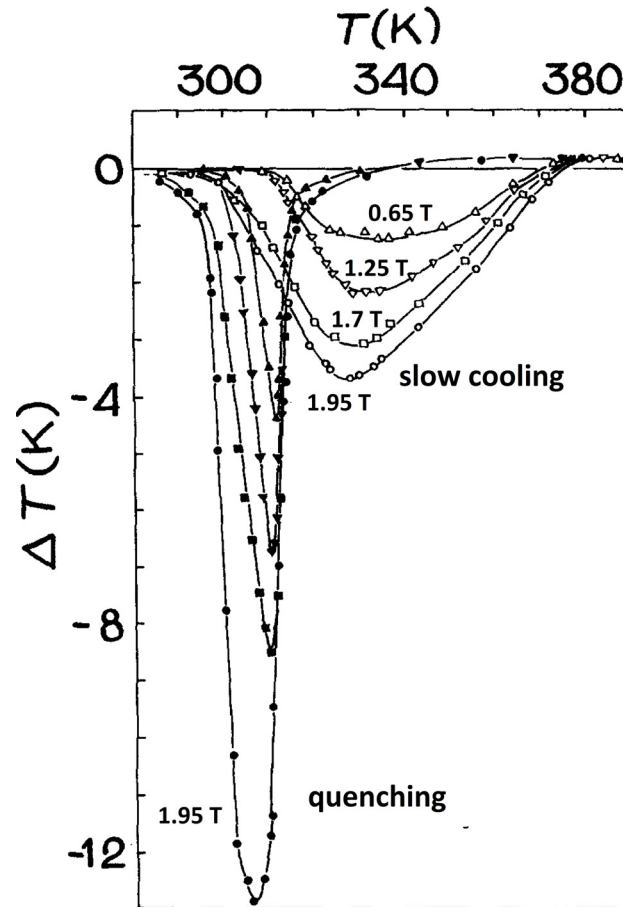


Figure 1.16 Temperature dependence of the magnetocaloric effect for slowly cooled and quenched samples of $\text{Fe}_{49}\text{Rh}_{51}$ alloy in various magnetic fields: 0.65 T; 1.25 T; 1.7 T; 1.95 T (after [121]).

In 2008, a study of the history dependence of magnetization across the first order transition revealed that contrary to the long held belief, the MCE in FeRh does not vanish if the field-temperature history of the sample is chosen properly [123]. Later in 2014, the reversibility of the MCE in FeRh has been confirmed by a direct determination of the field-induced entropy change from isothermal calorimetric measurements upon field cycling [114] (see Fig. 1.17a).

The adiabatic temperature change measured directly with a thermocouple and calculations by Maxwell relations from heat capacity and magnetization measurements were compared using Pd-substituted FeRh [124] (see Fig. 1.17b), which proved the estimation of the MCE in FeRh by Maxwell relations reliable. It was also found that the substitution of Pd for Rh can control the effective range of MCE in FeRh. In principle, the fact of compositional variation (substitution by Pd, Pt and Ir) affecting the entropy change has been known since early works on FeRh [65]. A study of the magnetocaloric response of FeRh-based compounds modified by Cu, Pd and Ni demonstrated that while elemental substitution consistently decreases magnetic entropy ΔS_M of the FeRh-based ternary al-

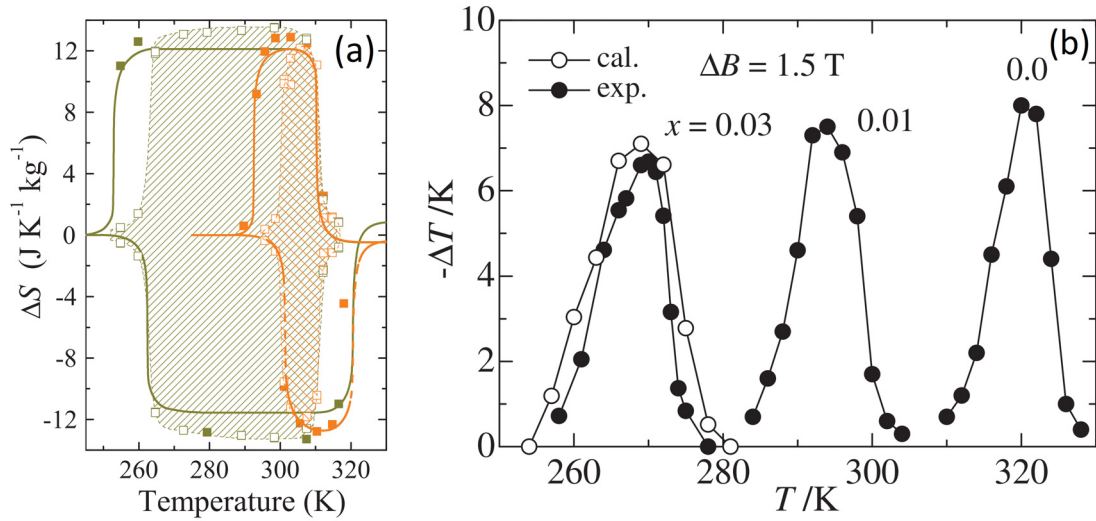


Figure 1.17 (a) Entropy change in $\text{Fe}_{49}\text{Rh}_{51}$ evaluated from isothermal thermal curves (symbols — solid for the first field application, open ones for the successive) and isofield thermal curves (solid lines) in 2 T (orange) and 6 T (green) magnetic field. The shaded area indicates the region of reversibility. (after [114]). (b) Adiabatic temperature change directly measured for the selected samples (closed circles), and a comparison of the estimated values (open circles) and directly measured ones for $\text{Fe}_{49}\text{Rh}_{0.97}\text{Pd}_{0.03}_{51}$ [124].

loys from that of the parent FeRh compound, the net refrigeration capacity (RC) of the modified systems is significantly higher [107]. The decrease in the peak of ΔS_M was attributed to changes in the electronic band structure of the FeRh system due to elemental substitution, and the enhanced RC in chemically-modified FeRh was ascribed predominantly to a local chemical-disorder-induced broadening of the magnetostructural phase transition. Similar to the analysis of the transition temperature dependence on valence band electrons [9] other data from the literature were taken into account to establish correlations between the valence band electron concentration and the magnetic entropy change of $3d$ - and $4d$ -substituted FeRh compounds, attempting prediction of the magnetic entropy change in this system.

The entropy change in FeRh under applied hydrostatic pressure or tensile strain becomes giant barocaloric [114] and elastocaloric [125] effects. The sharpness of the transition and the strong sensitivity of the transition to the external fields result in barocaloric and magnetocaloric strengths which compare favorably to those reported for other giant magnetocaloric and barocaloric materials. FeRh achieves its maximum isothermal entropy change at very low values of hydrostatic pressure and magnetic field, which makes this alloy particularly interesting in cooling applications where the external stimuli need to be restricted to low values [114]. The ability of FeRh to react to the tensile strain is considered in a dual-stimulus magnetic-electric refrigeration cycle in FeRh thin films via coupling to a ferroelectric BaTiO_3 substrate [126].

1.2.4 Strain, deformation and disorder effects

Hydrostatic pressure affects both the magnetostructural transition temperature T_{tr} and the Curie temperature of the FM–PM transition T_c : in the binary alloy the AF–FM transition shifts towards higher temperatures with $dT_{tr}/dp = 4.3\text{--}5$ K/kbar, while the Curie temperature is reduced only slightly, $dT_c/dp = -0.6\text{--}1$ K/kbar [51, 62, 127]. The transition temperature defines the dT_{tr}/dp value: the lower the transition temperature, the larger is the shift under pressure [62]. A typical behaviour of FeRh-based alloys under compression is shown in Fig. 1.18: a stabilization of the AF phase, i.e. an increase of the transition temperature can be observed in Fig. 1.18a; the initial FM state (in this case, induced by high magnetic field) and gradual appearance of the AF state upon increasing pressure are shown in Fig. 1.18b. Furthermore, this study of FeRh substituted by Pd revealed that the hysteresis and the transition width depend on T_{tr} irrespective of applied pressure and magnetic field [76]. In other words, except for a shift in the transi-

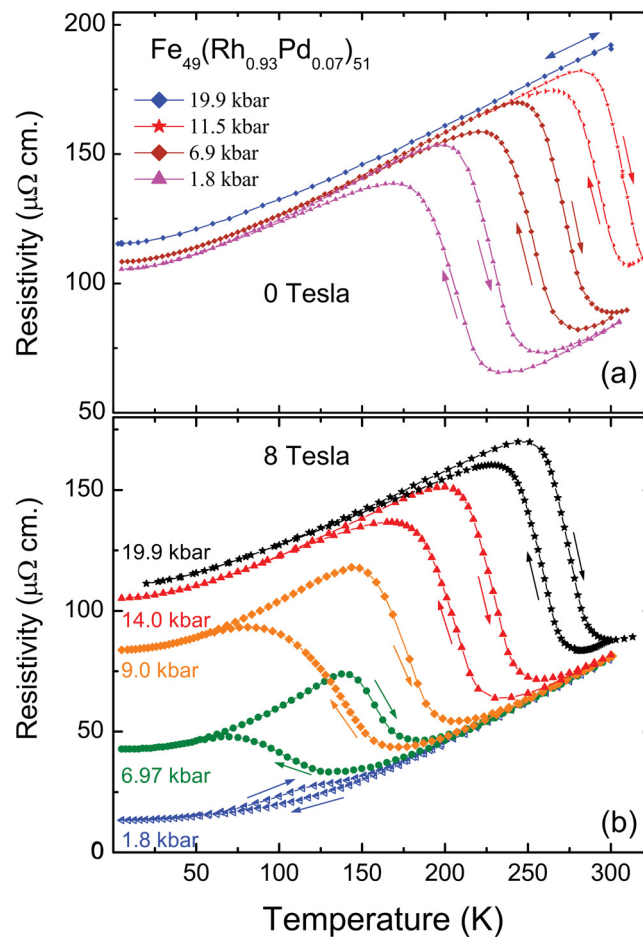


Figure 1.18 Resistivity ρ as a function of temperature for $\text{Fe}_{49}(\text{Rh}_{0.93}\text{Pd}_{0.07})_{51}$ at various constant pressure (a) in the absence of applied magnetic field and (b) in the presence of 8 T magnetic field. Both pressure and magnetic field are applied at room temperature [76].

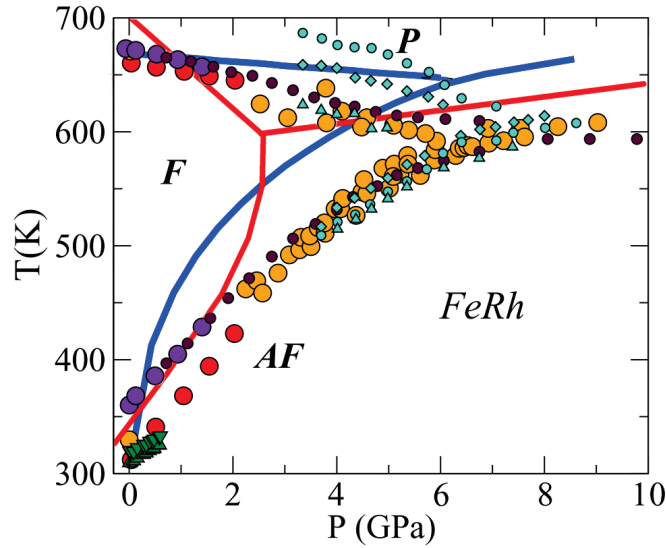


Figure 1.19 $p - T$ phase diagram for the equiatomic FeRh (after [118]), lines are simulations (blue from [118], red from [132]), points are experimental data summarized in [118].

tion temperature, no explicit role of pressure and magnetic field on first-order transition characteristics was found. Ternary FeRh alloys modified by Pd and Ni have a low transition temperature and a large temperature shift upon pressure and magnetic field, which places the investigation of the pressure effect on AF–FM transition in a more attainable experimental range, since it will require lower pressure and magnetic field. For example, the effect of suppression of the FM state and inducing the AF–FM transition in the binary FeRh requires pressures up to 100 kbar [128], whereas in a Ni-modified FeRh, the hydrostatic pressure up to 13 kbar is sufficient [129–131].

Due to the negative sign of dT_{tr}/dp and the positive sign of dT_c/dp , an existence of a triple point on the $p - T$ phase diagram between AF, FM and PM states was predicted at approximately 50-55 kbar and 630 K [62, 127]. In the beginning, most studies were limited to 25 kbar, so the triple point was confirmed experimentally much later, first for the Ir-doped FeRh [133] and then for the binary FeRh [134]. However, since the linearity of the $p - T$ -dependence was found to break down above pressures of about 25 kbar [133], the triple point is at 75 kbar, which is far beyond the predicted values. The complete magnetic phase diagram under pressure is shown in Fig. 1.19 containing experimental data as well as some simulations. The nature of the AF–PM transition at pressures above the triple point remains disputable. Although there is an assumption that this transition is of the first order [127] supported by a structural investigation of Ir-doped alloys [68], mostly the second order is assumed and expected [62, 135]. The simulations [132] and experimental data [133] seem to be in agreement with this idea. Furthermore, in binary and Ir-doped FeRh, no temperature hysteresis for the AF–PM transition at pressures above 68 kbar was found [134, 136].

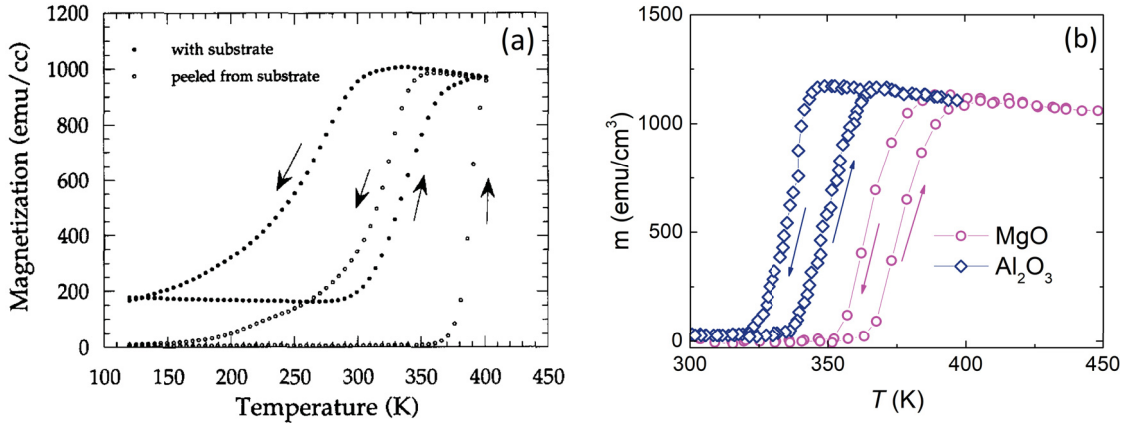


Figure 1.20 (a) Thermal hysteresis of magnetization in $\text{Fe}_{47.8}\text{Rh}_{52.2}$ thin film before and after peeling. [137] (b) Temperature hysteresis for the same 110-nm-thick FeRh films grown onto MgO(001) and Al_2O_3 (0001) (after [138]).

While the compressive strain stabilizes the AF state, a tensile stress suppresses it, shifting the transition temperature T_{tr} downwards or even partly inducing the FM state. This shift can be observed along with a giant elastocaloric effect in a bulk sample under tensile stress [125]. Tensile stress is commonly found in thin films at the interface between the film and the substrate. The AF–FM transition in FeRh thin films is known to differ from bulk samples: it takes place in a wider temperature interval and shows a larger temperature and field hysteresis [101].

FeRh films are usually deposited or annealed at high temperature, because it is a requirement to obtain the chemically ordered α' -phase [139]. During cooling, a significant difference in the thermal expansion coefficients of the film and the substrate results in a stress. This effect is illustrated in Fig. 1.20a: an initial FM phase fraction observed in an annealed film deposited on a quartz substrate disappeared after the film was peeled off the substrate, the hysteresis was reduced and T_{tr} increased by 50 K [137]. A detailed structural study confirms that the lattice parameters of a 100 nm FeRh thin film on a quartz substrate have a 1 % difference in out-of-plane and in-plane directions [101].

In epitaxially grown films, the mismatch between the lattices of the film and the substrate becomes a source of strain. In Fig. 1.20b, the AF–FM transition occurs at different T_{tr} in FeRh films grown on MgO and Al_2O_3 substrates under otherwise identical conditions [138]. It has been shown that when an MgO-based substrate has a closer match to the FeRh FM phase, it is naturally stabilized and T_{tr} decreases [140]. The strain is larger in the region of the substrate-film interface, so the magnetic state strongly depends on the film thickness as well [141, 142]. Likewise, the type of a capping layer can play an important role in the FM phase stabilization [143]; experimentally, this effect can be observed in capped and uncapped films through the difference in evolution of the FM domains near the surface [144].

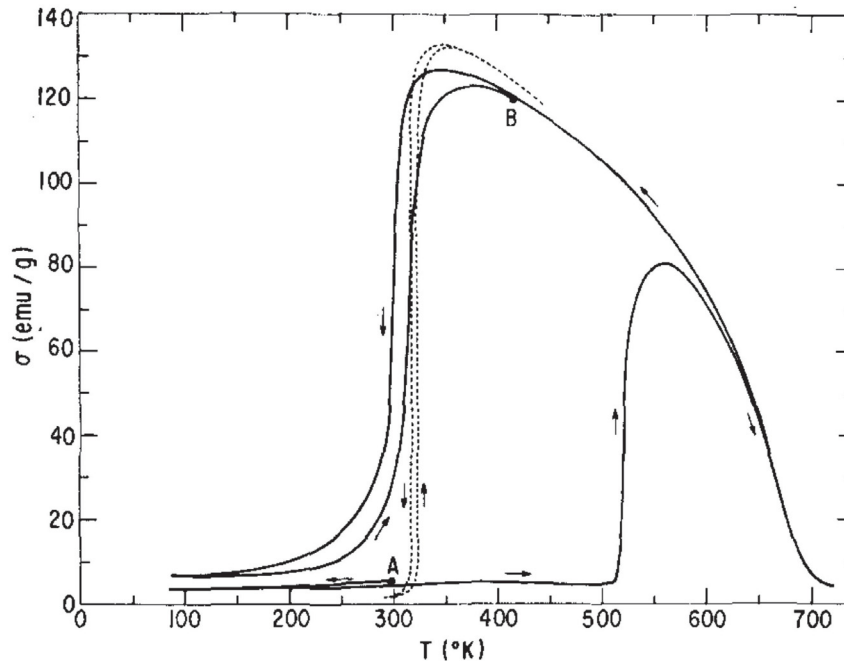


Figure 1.21 Magnetization dependence of FeRh filings on temperature showing paramagnetic behaviour and a transition to the FM state upon heating (A) [146], with a further recovery of the AF–FM transition (B) compared to the initial transition of the bulk FeRh (dashed line).

The exchange interaction in the strained layer plays an important role in determining the phase transition temperature, depending on whether it supports AF or FM interactions [145]. Depending on the choice of the substrate, it is possible to tune the transition temperature. First-principles calculations, accounting for epitaxial strain in thin films, indicate a strong spin-phonon coupling sensitive to the slight tetragonal distortions [117] and suggest that strained FeRh in the thin film form undergoes a spin-reorientation through the AF–FM transition [140]. Strain conditions must be considered explicitly in the comparison of bulk materials and epitaxial thin films [117].

The discussed tensile and compressive stress is elastic, and the magnetic state can be recovered after the stress removal. Plastic deformation (e.g. filing, cold work or rolling) converts the ordered CsCl-structure (α' , B2) of FeRh into a disordered fcc structure, which is only weakly magnetic and does not exhibit the first-order transition [146]. For example, 24 hours of ball-milling transform FeRh to a single-phase fcc nanocrystalline powder [147]. However, upon annealing disordered FeRh, the magnetic state can be recovered (see Fig. 1.21): first, an ordered B2 structure appears with the material being ferromagnetic down to low temperatures, then, a gradual return of the first-order transition is observed, which will further evolve in completeness and sharpness. These effects are attributed to a gradual attainment of the perfect long-range order and an annealing of the defects produced by plastic deformation [146].

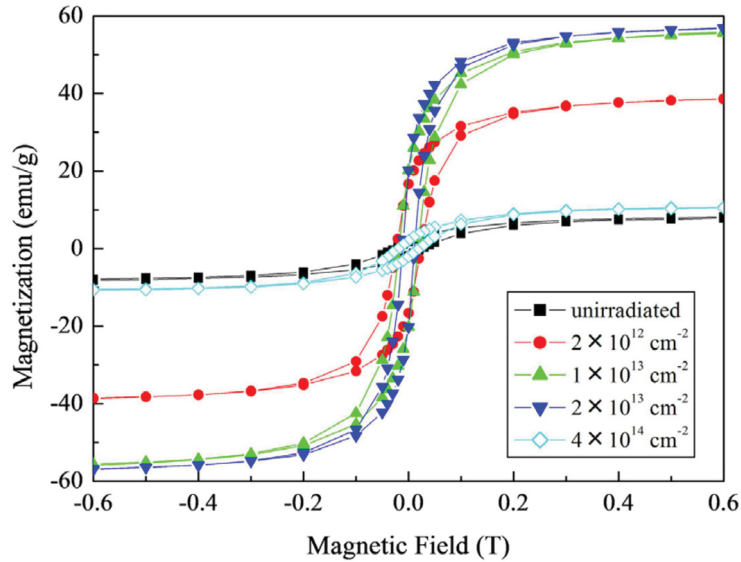


Figure 1.22 Magnetization loops of irradiated FeRh films that experience an induced FM state and its subsequent suppression as the ion energy rises [150].

An in-situ study of FeRh under pressures up to 19 GPa detects a partial transition of the B2-structure into fcc at a critical pressure of 9.8 GPa, accompanied by an approx. 1.5 % collapse of the lattice parameter. The newly formed fcc phase has an almost constant value of the lattice parameter that is much smaller compared to the fcc lattice parameter at ambient pressure, reflecting a rather compressed structure [148]. Apart from the stress-induced transformation of B2 into fcc, a transformation of B2 structure to L1₀ was also reported in a cold-rolled FeRh [149]; the final phase being dependent on the rolling rate (30 % and 5 %, respectively). While the formation of the fcc-phase is likely caused by the destruction of the B2-order, the origin of the L1₀ formation is not clarified.

The effect of disorder can be studied by irradiation of FeRh thin films with energetic ions (H, He, I). Depending on the density of energy elastically deposited by the ions (180 keV-10 MeV), the magnetic state can be modified from AF to FM and even paramagnetic [151]. Irradiation allows to study the effect locally (e.g. by MFM), producing precise micrometer-sized FM areas in an AF matrix by means of an ion microbeam [152].

Different magnetic states of irradiated FeRh thin films are shown in Fig. 1.22. The ferromagnetism in the ion irradiated FeRh is shown to be mainly dominated by the spin moment [150]. The increase in magnetization can be caused by irradiation-induced lattice defects, while the decrease is attributed to the structural change from the FM α' -phase (B2) to paramagnetic γ (A1) phase.

Alike with the severely deformed FeRh, after annealing (100-500°C) the irradiation-induced A1 structure thermally relaxes to the disordered B2 structure, changing magnetically from PM to FM [153]. When the ion fluence is not so large and the disordered B2 structure is induced, it thermally relaxes to the ordered B2 (α'), recovering the AF state.

1.2.5 Heat treatment effect

Thermal history strongly affects the magnetic properties of FeRh, as can be seen from Fig. 1.16. The temperature, the time of heat treatment and the cooling path are often chosen randomly: it creates a certain discrepancy in the reported data. This fact was noted at an early stage of FeRh research, comparing the reported transition temperatures and their shift with applied pressure [62]. The experimental evidence of thermal history effects is present in the literature but hardly explained: for example, observing the AF–FM transition in as-cast, annealed, remelted and cycled binary FeRh [154].

The effect of heat treatment on the AF–FM transition is illustrated for a bulk sample in the as-cast and the annealed state (Fig. 1.23a) and for thin films annealed at different temperatures (Fig. 1.23b). The heat treatment of FeRh is usually chosen in the region 500–1200 °C to achieve better ordering. In the case of thin films, heat treatment is particularly critical: to obtain a well-ordered bcc-B2 structure, the films should be deposited at high temperature or post-annealed, otherwise a film deposited at room temperature will have a paramagnetic disordered fcc structure [101, 139, 155, 156].

Among the few studies attempting to clarify the situation was an investigation of binary equiatomic FeRh at temperatures of 970 K and 1070 K upon varied time of annealing from 12 hours up to 2–3 weeks [46]. The evolution of the resistivity profile with the annealing time is shown in Fig. 1.24. A drastic change in the behaviour of the AF–FM transition can be observed, resulting in a shift of the transition temperature by more than 60 degrees along with the evidenced by TEM formation of fcc γ -precipitates in the main α' -phase. An update for the phase diagram was proposed (shown in Fig. 1.11a) and a suggestion that during the formation of the Rh-rich precipitates, a gradient of composition is formed; a possibility of existing strain between the two phases was discarded.

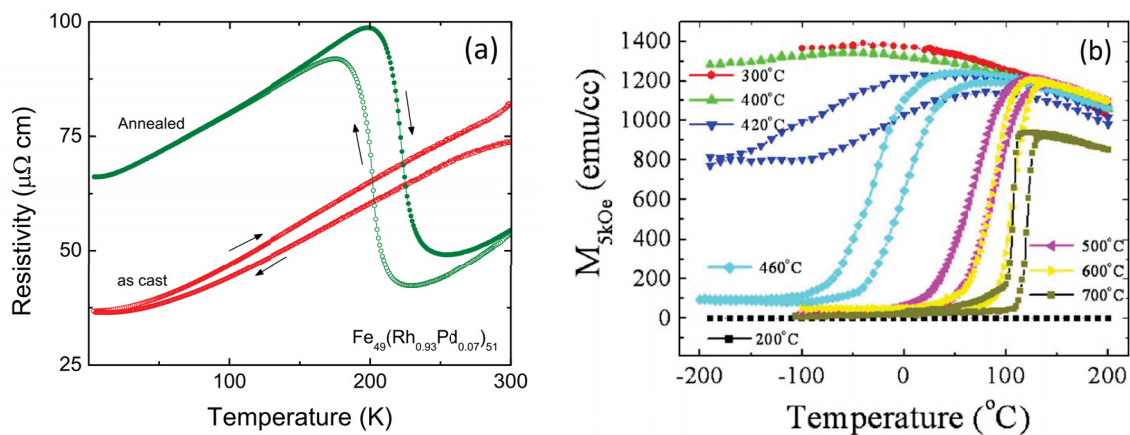


Figure 1.23 a) Resistivity behaviour as a function of temperature for as cast and annealed samples [81]. b) Temperature dependence of magnetization in the magnetic field of 0.5 T for FeRh thin films annealed at different temperatures [156].

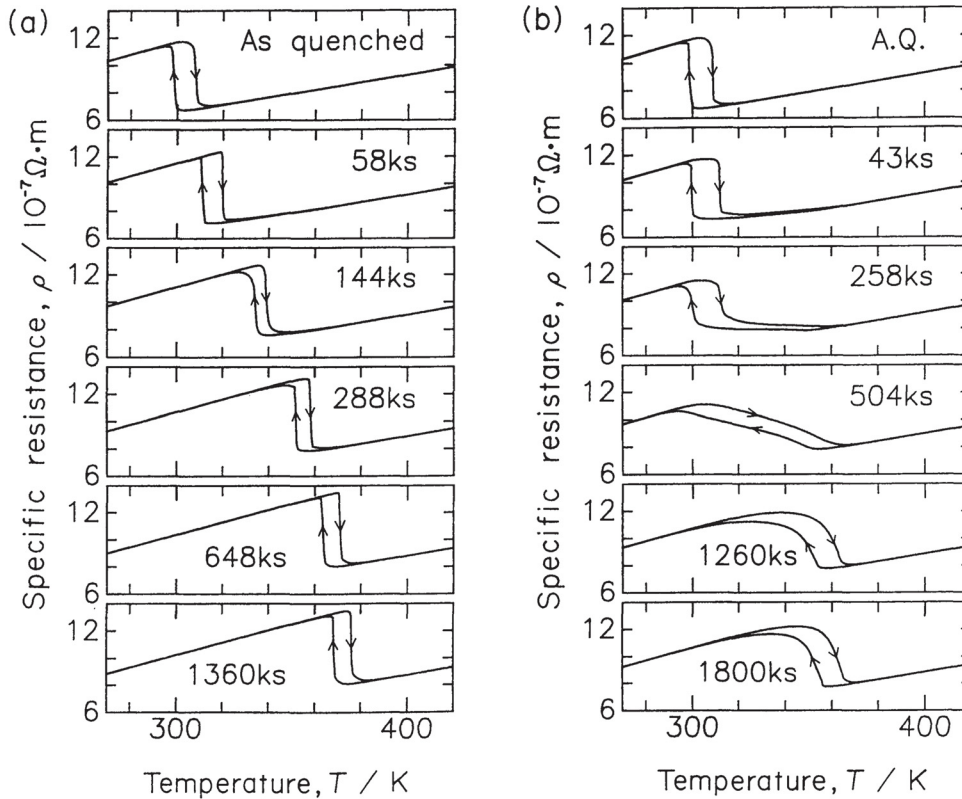


Figure 1.24 Changes in profile of T - ρ curves of Fe_{50.5}Rh_{49.5} alloys for different annealing temperatures at (a) 970 K and (b) 1070 K with annealing times [46].

Two studies of the binary FeRh close to the equiatomic region reported on lattice parameters, fractions and compositions of the α' - and γ -phases after systematic heat treatment [48, 50, 60]. An investigation containing 5 alloys with a nominal composition of 55 at. % Rh had the heat treatment varied from 800 °C to 1350 °C, simultaneously decreasing the time from 1680 h to 6 h [48, 50]. In all cases the B2 α' -phase had a similar Rh content of 50.1-50.4 at. %, and in the fcc γ -phase the Rh content varied from 54.7 to 61.5 at. %. These results introduced corrections to the phase diagram from 1984 [45]. Another study was done on compositions of 51-63 at. % Rh after annealing at 1000 °C for 50 hours [60]. The lattice parameters of both α' - and γ -phases in the alloys with 55-59 at. % Rh were found to be the same, however, the transition temperature still varied significantly by more than 50 degrees and the saturation magnetization was strongly reduced (Fig. 1.11b). The quantitative analysis of the diffraction data has revealed an increasing amount of the fcc γ -phase with higher Rh content. The temperature shift and increased hysteresis was attributed to inhomogeneous strain caused by the presence of the minor phase, and the reduction of magnetization to its increasing amount.

Overall, there is a deficiency of systematized experimental data on the material properties of FeRh and on a relation of the magnetic state to the details of microstructure and sample preparation procedure.

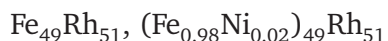
CHAPTER 2

EXPERIMENTAL METHODS

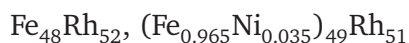
The experimental methods include systematic sample preparation (synthesis, heat treatment protocols, preparation for the structural and microstructural characterization); analysis of the phase content by means of XRD and microscopy, as well as measurements of magnetic and caloric properties.

Nominal compositions of the FeRh-based alloys used in this work (binary and pseudo-binary modified by other d-elements) are listed below along with the carried out experiments:

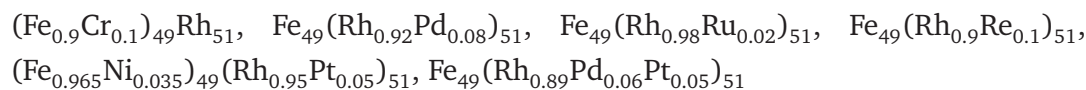
- **Direct measurements of MCE:**



- **Heat treatment effect + Microstructure + MCE:**



- **Microstructure + MCE:**



2.1 Sample preparation

2.1.1 Synthesis and heat treatment

Bulk polycrystalline samples of FeRh-based alloys modified with up to 6 at. % by 3d-metals (Ni, Co, Cr), 4d-metals (Ru, Pd) and 5d-metals (Re, Pt) were prepared by arc melting of the pure elements in a helium atmosphere in a water-cooled copper crucible*. In order to ensure good homogeneity, the pellets were turned and remelted several times. Due to the sample placement on a cooled crucible, the ingots experience a strong directional cooling effect during the solidification, which results in a dendritic structure.

*Carried out by Prof. Dr. N.V. Baranov, Ural Federal University and Bernhard Gebel, IFW Dresden

Sample preparation

Homogenization of the samples was done in evacuated quartz ampules, generally at 1000°C for 1-2 weeks followed by quenching into water. In order to investigate the effect of three factors of heat treatment (time, temperature and cooling rate) on the magnetic state, pieces of the same as-cast ingot of the nominal compositions $\text{Fe}_{48}\text{Rh}_{52}$ and $\text{Fe}_{49}(\text{Ni}_{0.035}\text{Rh}_{0.965})_{51}$ were subjected to a special heat treatment at three chosen temperatures 850°C, 1000°C and 1150°C; the time of the annealing was either 3 or 14 days, the cooling was either water quenching or oven cooling with a rate of 1°C/min down to 400°C and with the furnace switched off. Then, samples of typical thickness ~ 1 mm in the shape of plates or rectangular rods were cut out. The surface was subjected to metallographic preparation to remove the deformed layer for correct structural and microstructural characterization.

Additionally, Ni-doped samples were exposed to a post-annealing at 500°C for 3 hours with 1°C/min cooling to remove stress after rapid cooling from high temperature. Alternatively, rapid cycling between liquid nitrogen and water of room temperature was applied as a thermal shock, to induce as much stress as possible.

2.1.2 Metallographic preparation

For scanning electron microscopy and X-ray diffraction, the samples were prepared using standard metallographic techniques: grinding on SiC paper by hand (P800, P1200, P2500) and polishing with diamond suspension (3 μm , 1 μm and 0.25 μm) for short times (3-5 minutes) and in some cases Al and Si oxide slurries as a final step. A low

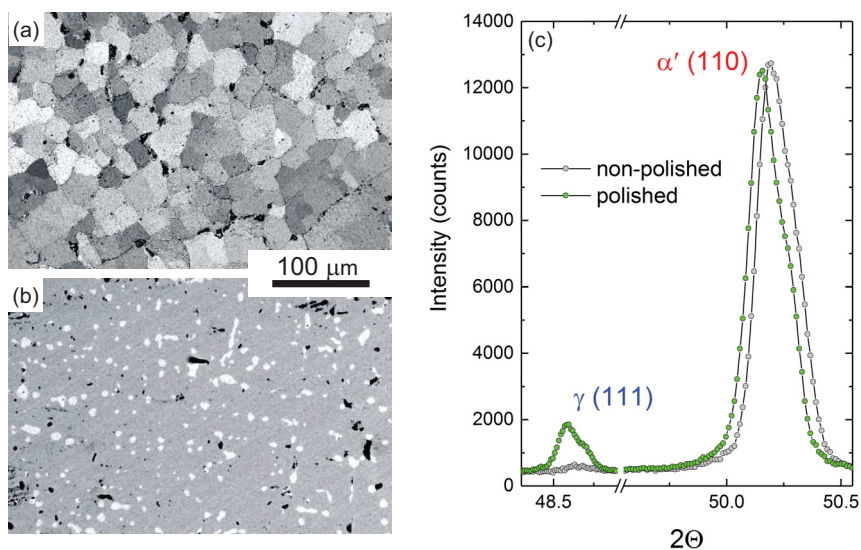


Figure 2.1 Effects of sample surface preparation observed by X-ray diffraction and SEM of the same sample: directly after heat treatment (a, grey XRD data) and polished (b, green XRD data).

polishing speed (~ 30 rpm) was used to avoid deformation of the surface*. The surface deformation may affect magnetic properties, moreover, the structural and microstructural data. During longer polishing times, hard inclusions of the minor phase tend to fall out and leave noticeable scratches in the softer B2 phase. The diamond suspension was found to be the most efficient polishing agent. The heterogeneous microstructure is visible only after polishing the sample – the surface layer present after annealing seems to affect both XRD and microscopy, providing misleading results. The examples are shown in Fig. 2.1: the characterization of the sample after the heat treatment without polishing probes the recrystallized surface layer and yields a single-phase pattern with a lattice parameter differing from the one after the polishing. In the polished sample, the secondary phase is revealed in both XRD and SEM.

For scanning transmission electron microscopy (STEM), a lamella was prepared by focused ion beam (FIB) technique from an $\text{Fe}_{49}\text{Rh}_{51}$ sample**. The front side of the sample was protected from the ion beam by a deposited Pt layer. Thicker support bars were left in between thinner windows to stabilize the sample. The lamella was attached to an M-shaped sample holder and thinned down until the appearance of holes.

2.2 Structural characterization

2.2.1 Phase identification

The as cast and heat treated samples were characterized by means of X-ray diffraction (XRD) in order to determine the phase content, lattice parameters and the degree of

*Carried out in collaboration with Katja Berger, IFW Dresden

**Carried out by Almut Pöhl, IFW Dresden

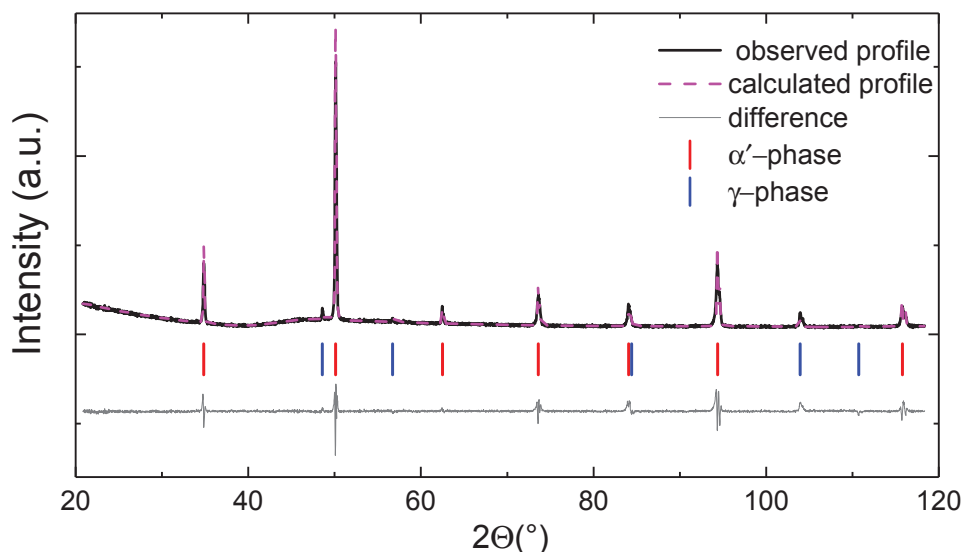


Figure 2.2 An example of the Rietveld refinement carried out in FullProf Suite [157] for a typical pattern of FeRh consisting of α' -phase (B2) and γ -phase (A1).

order. The measurements were performed on bulk samples at room temperature using a Bruker Advance X8 diffractometer (Co- K_{α} radiation). The XRD scans were done using the $\theta/2\theta$ scheme, where θ is the rotation angle of the incident beam, and 2θ is the rotation angle of the detector. The sample in-plane rotation with 30 rpm was enabled in order to ensure random orientation of the exposed grains. X-ray diffraction patterns were collected in the 2θ angle range between 20 and 120 degrees with a step size of 0.03° and a time per step of 4 s for the standard characterization, and 0.02° and 20 s for the determination of the degree of order. In the case of the as cast sample, for better fitting, a double exposure time (40 s) was chosen due to a very low intensity of the α' -phase peaks.

The XRD patterns were analysed using Fullprof Suite software [157] that employs the Rietveld refinement algorithm. Typical real and calculated patterns, as well as the difference in the result of refinement are shown in Fig. 2.2. As far as FeRh alloys are extremely sensitive to mechanical treatment, it is problematic to carry out diffraction experiments using powder. Therefore, the XRD patterns were obtained from bulk samples. The samples had a small size and considerably large grains — it causes strong texture effects and the shown example has a good fit for such a case. Due to the conditions of exposition, the refined profile is unsuitable for a precise determination of phase fractions, but sufficient for determining lattice parameters. The error for the determination of lattice parameters was $\pm 0.001 \text{ \AA}$.

2.2.2 Determination of the degree of order

FeRh alloys are ordered in a CsCl-type structure: Fe occupies $\{0,0,0\}$ Rh occupies $\{1/2,1/2,1/2\}$. That is, Rh replaces the central atom in the bcc α -iron lattice. A per-

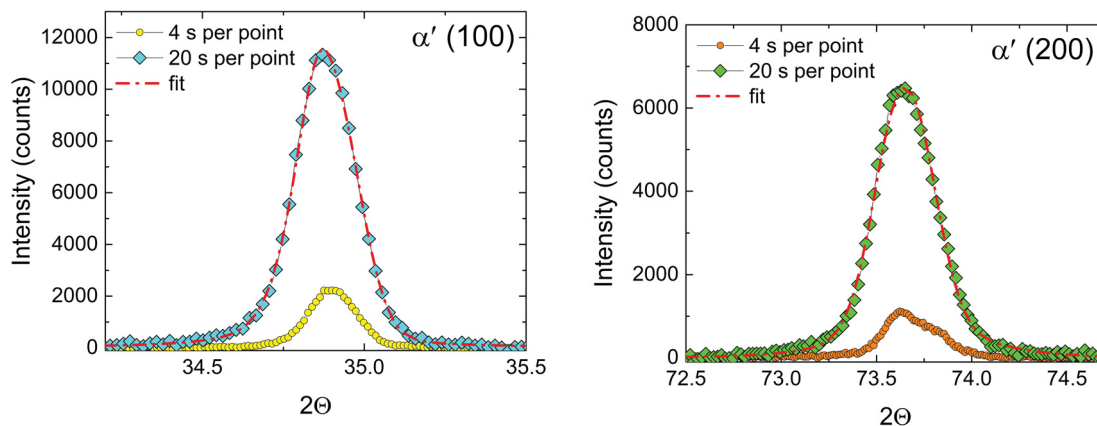


Figure 2.3 Superlattice (100) and fundamental (200) peaks intensities acquired at different counting times and the fit of the peaks that were used in the determination of the degree of order.

fect order results in the appearance of superlattice peaks additional to the fundamental diffraction peaks that are allowed for a bcc lattice. In the situation of a complete disorder one can observe only the fundamental peaks. The degree of order can be estimated using the ratio of the integrated intensities of the superlattice and fundamental peaks, for example (100) and (200), respectively. The order parameter s is proportional to this ratio, and varies from 0 to 1, where 1 describes the perfect order and 0 the complete disorder. In the case of the peaks from the same family of planes, for example (100) and (200), the result should be unaffected by the texture, which is beneficial for the samples that were investigated in this work. In order to improve the accuracy, the peaks were measured with 5 times longer exposure times compared to the conditions chosen for the phase analysis patterns. The difference is illustrated in Fig. 2.3; the long exposure time provides a better resolution for the two peaks in comparison with the exposure used for the simple lattice parameter determination. The red dashed line shows the fitting.

2.3 Magnetic measurements and calorimetry

2.3.1 Quasistatic magnetic field

For magnetic measurements the following devices were utilized*: 1) MPMS-XL Quantum Design (Magnetic Property Measurement System) magnetometer with magnetic fields up to 7 T created by a superconducting magnet and a temperature range of 1.8-400 K. The MPMS device employs a superconducting quantum interference device (SQUID) for measuring the magnetization with the absolute sensitivity 10^{-8} emu. 2) PPMS-14T Quantum Design (Physical Property Measurement System) with magnetic field up to 14 T created by a superconducting magnet and a temperature range of 1.9-400 K, equipped by a VSM-option (Vibrating Sample Magnetometer). The accuracy is better than 10^{-6} emu.

The samples were not exceeding 100 mg in size and the sweeping rate was 2 K/min. For testing purposes, a measurement was carried out with sweeping rates of 1 K/min and 5 K/min, but no significant difference was found. Still, the sweeping rate 2 K/min was considered more appropriate for maintaining equilibrium conditions.

Magnetic measurements under fixed hydrostatic pressure have been carried out with a rate of 1 K/min in a CuBe EasyLab Mcell10 high-pressure cell for the MPMS allowing a pressure up to 10 kbar. The pressure was applied by using the screws at the end of the cell and monitored by the reaction of superconductive phase transition temperature in Sn placed in the chamber along with the sample.

The $M(T)$ dependences for characterization of the AF–FM transition were measured at 1 T magnetic field; magnetic measurements for the entropy change calculations were done in fields from 0.1 T up to 2 T with 0.25 T steps. Normally the dependences were measured on heating with subsequent zero field cooling (ZFC) before the next field

*Carried out in collaboration with Dr. K. Nenkov, IFW Dresden

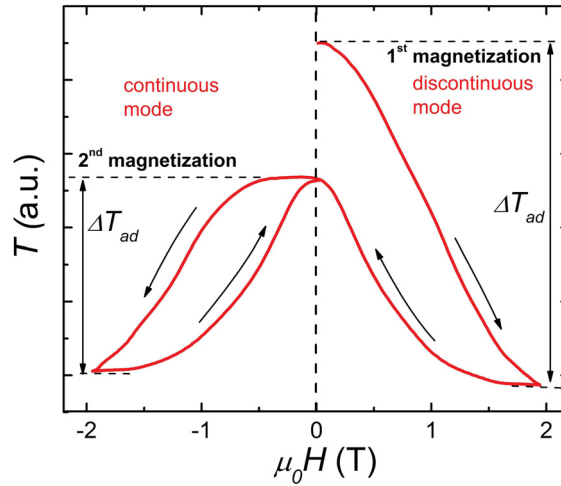


Figure 2.4 Adiabatic temperature change in FeRh during one magnetic cycle $0 \text{ T} \rightarrow 1.9 \text{ T} \rightarrow -1.9 \text{ T} \rightarrow 0 \text{ T}$: the discontinuous mode results in the maximal value reached at 1.9 T , the continuous mode corresponds to the second magnetization or the value at -1.9 T .

application at low temperature. In order to estimate the hysteresis, dependences on cooling were measured as well. The entropy change was calculated from the $M(T)$ data using the Maxwell relation, numerically represented as:

$$\Delta S_{mag}(T)_H = \frac{1}{2} \sum_i \left[\left(\frac{\partial M_i}{\partial T} \right)_{H_i} + \left(\frac{\partial M_{i+1}}{\partial T} \right)_{H_{i+1}} \right] (H_{i+1} - H_i) \quad (9)$$

Heat capacity measurements were carried out in a PPMS-14T Quantum Design using the standard relaxation calorimetry (2- τ method) [158] before and after the transition, and for the quantitative estimation in the transition region the method described by Suzuki *et al.* [159] was applied. The temperature dependences of the heat capacity $C_H(T)$ measured in different magnetic fields were integrated to obtain the dependences $S(T)_H$ that were combined into S - T -diagrams. The S - T -diagrams were used for calculation of ΔS and an alternative evaluation of the adiabatic temperature change [15], as demonstrated in (8) and Fig. 1.1.

2.3.2 Halbach magnets

The direct measurements of the adiabatic temperature change ΔT_{ad} in a Halbach setup were done in a home-built experimental setup that allows fast altering of the magnetic field with a rate of 0.5 T/s going through the magnetization-demagnetization cycle ($0 \rightarrow 1.93 \text{ T} \rightarrow 0 \rightarrow -1.93 \text{ T} \rightarrow 0$) so that experiments under cyclic conditions can be done*. The temperature was controlled by a copper-Constantan thermocouple attached to the sample by silver-based epoxy.

*Carried out by Dr. K.P. Skokov, TU Darmstadt

The adiabatic temperature change at a certain temperature can be measured in a discontinuous mode or continuously. The discontinuous mode is a measurement that starts every time from the same initial state and provides the highest values of ΔT_{ad} . It is illustrated by the right branch in Fig. 2.4. A subsequent field application (the continuous mode) will result in the second branch (the left branch in Fig. 2.4) and a reduced value of ΔT_{ad} , which characterizes the reversible behaviour. This is caused by the existence of a hysteresis in materials with a first order transition, originating from a mixed magnetic state in that region. To return to the initial state it is necessary to heat the sample up or cool down beyond the hysteresis region. The discontinuous mode represents measurements that are independent of each other and can be viewed as a characterization of fundamental properties of a material. The measurements under cyclic conditions are relevant for the evaluation of the material performance as in a real magnetic cooling cycle.

2.3.3 Pulsed magnetic field

Magnetic pulsed fields up to 48 T were provided by the Dresden High Magnetic Field Laboratory (HLD) [160]. The magnetization in pulsed fields is measured by integrating the voltage induced in a compensated coil system surrounding the sample [161]. The total pulse duration is 10-20 ms for the magnetic and magnetocaloric measurements. The direct adiabatic temperature change measurements were carried out in a home-built experimental setup [162] in pulsed fields varying in the range of 2-48 T (with a field change rate of 100-2500 T/s respectively)*. The temperature change of the sample was controlled by a copper-Constantan thermocouple attached to the sample by silver-based epoxy. The measurements were carried out in the discontinuous mode only, when every measurement starts from the same initial state that is not affected by the hysteresis.

2.4 Microscopy

2.4.1 Scanning electron microscopy and quantitative analysis

Scanning electron microscopy (SEM) and energy dispersive X-ray spectroscopy (EDX) measurements were carried out in JEOL JSM-6510 and Zeiss LEO Gemini 1530 microscopes both equipped with a Bruker EDX system. The electron micrographs were obtained in a BSE-mode (backscattered electrons). This allows the best detection of the γ/α' -phases with high contrast since the γ -phase in this region typically has an excess of rhodium.

For quantitative metallography, backscattered electron images from randomly selected regions were recorded from each sample. The total analysis area per sample was approximately 10-15 % of the total sample area. Phase fractions were determined from

*Carried out in collaboration with Dr. Y. Skourski, Helmholtz-Zentrum Dresden-Rossendorf

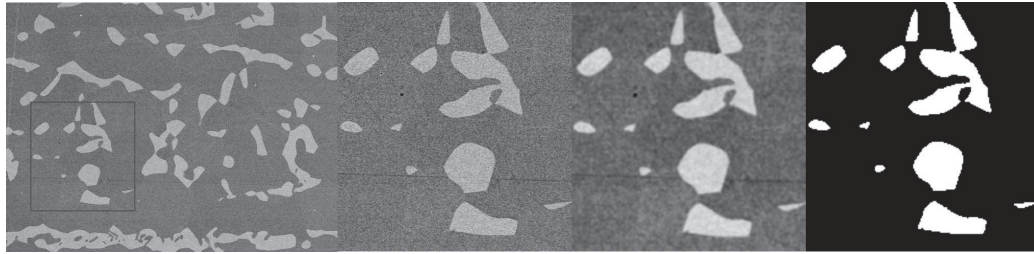


Figure 2.5 Image binarization process: after applying Gaussian blur, the threshold between two grey values is chosen to distinguish the two phases.

these images and in order to be able to separate the two phases, the images were first smoothed by convolution with a Gaussian kernel and then binarised using a threshold chosen manually for each image*. The phase fractions were determined by counting the white pixels. The process is illustrated in Fig. 2.5.

In this microstructural study, it has been observed that a final polishing with Al or Si oxide slurries produces a great surface quality that could be practical for such techniques as EBSD. However, for the quantitative analysis, the orientational contrast of both phases in backscattered mode can produce the same grey values (see Fig. 2.6, the micrograph). Therefore, a coarser polishing with diamond suspension was applied. It can be observed on the micrographs in Fig. 2.5 and Fig. 2.6 obtained from the same sample.

2.4.2 Scanning transmission electron microscopy

Scanning transmission electron microscopy (STEM) was carried out in an FEI Technai T20 with a LaB6 filament, operating at 200 kV**. EDX linescans were carried out across phase boundaries. The step size used was 10-12 nm.

*The quantitative metallography program designed and written by Dr. T.G. Woodcock, IFW Dresden

**Carried out by Dr. T.G. Woodcock, IFW Dresden

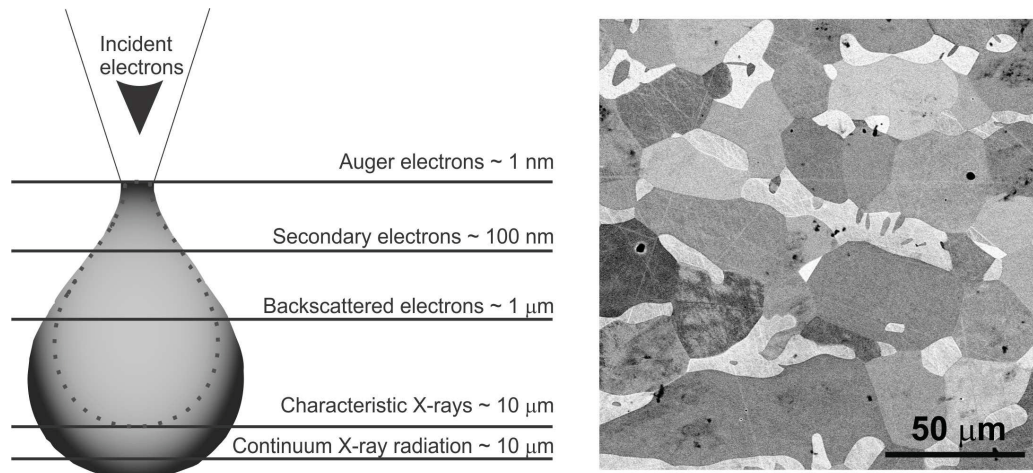


Figure 2.6 Electron interaction volume and example of microstructure in binary FeRh.

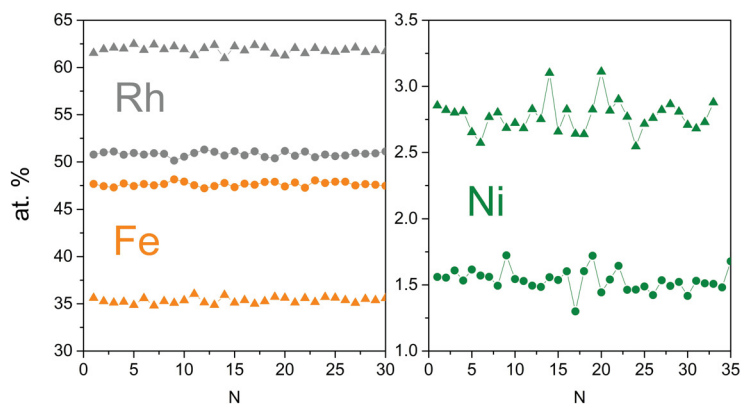


Figure 2.7 Scatter of N data points in EDX measurements of a Ni-doped FeRh sample. Circles and triangles show the major α' - and minor γ -phase, respectively.

2.4.3 Energy dispersive X-ray spectroscopy

Energy dispersive X-ray analysis was performed to determine the local composition of different phases. In order to achieve sufficient statistics, there were at least 25 EDX measurements for each reported phase. The scatter in these composition measurements was under 0.2 at. % for each phase (Fig. 2.7), which is less than the systematic absolute error of 1 at. %. The information about the composition becomes especially relevant for FeRh due to the known sensitivity of the magnetic state to variations in composition.

However, it has to be considered that the accuracy of the method does not ensure validity of a detected change in composition of only fractions of atomic percents. One must be careful with the explanation of the observed magnetic effects using small values below the systematic error. Besides, the interaction volume of the backscattered electrons and characteristic X-rays for EDX is comparable with the size of the Rh-rich secondary phase (see Fig. 2.6) which introduces a certain degree of ambiguity in the analysis, since the z-direction is not seen.

2.4.4 Magnetic force microscopy

The MFM measurements have been carried out in a Bruker Dimension Icon atomic force microscope*. MFM images of bulk Ni-doped samples at room temperature were obtained in the tapping mode at a scan height of 100 nm. Magnetic domains were easy to observe because the chosen samples had the AF–FM transition below room temperature, and therefore were in the FM state. It was discovered that the polishing procedure can strongly affect the MFM image. In principle, it is known that the polishing procedure may affect the magnetic domains [163]. In Fig. 2.8 it can be seen that the magnetic domains show different types of patterns. Different domain patterns in each sample

*Carried out by Katja Berger, IFW Dresden

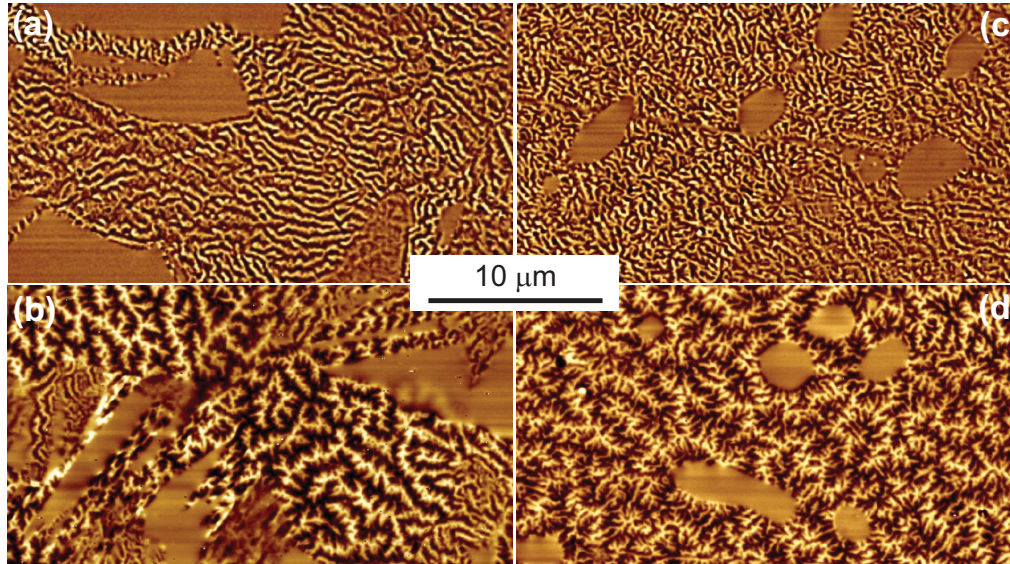


Figure 2.8 MFM images of the same as-cast (a, b) and annealed (c, d) FeRh-based samples after different polishing: (a) and (c) have similar domain patterns and represent the effect of a deformed surface layer. (b) and (d) are believed to be genuine magnetic domains.

were caused exclusively by a change of the polishing procedure, no other treatments were done in between. Final polishing steps are most important in the case of FeRh, because the material is soft and easy to deform. The result is not always straightforward: a strongly deformed but seemingly flat surface may result in an appropriate topographic image but show practically no magnetic contrast, whereas a surface with some scratches can still show clear and bright magnetic domains.

2.5 Modelling

The simulations of the elastic stress fields during the metamagnetic transition caused by a heterogeneous microstructure were done by means of the finite elements method (FEM) software Marc Mentat*. Two-dimensional models with different morphologies of γ grains in an isotropic α' matrix were created. As the mechanical properties of the phases in FeRh alloys are not known in detail, Young's modulus and Poisson's ratio of pure iron (200 GPa and 0.3, respectively) were used to represent both γ and α' phases, while a length variation of 0.33 %, equivalent to a volume change of 1 %, was assumed for the α' matrix according to the metamagnetic transition. The FEM models contain approximately 3500 elements; a heterogeneous node distribution was chosen to enhance the calculation performance near the γ/α' boundary. Continuous boundary conditions were applied.

*Carried out by Dr. F. Bittner, IFW Dresden

CHAPTER 3

DIRECT MEASUREMENTS OF THE MAGNETOCALORIC EFFECT

This chapter presents direct measurements of the adiabatic temperature change ΔT_{ad} in binary and Ni-doped FeRh*. Two measurement protocols were applied: 1) approaching each temperature point from the pure AF state to estimate the maximal value at the metamagnetic transition to the FM state; 2) cyclic conditions, when the next application of the magnetic field occurs immediately after demagnetization to account for the hysteresis losses. The ΔT_{ad} values from the direct measurements are compared to those determined from conventional quasi-static magnetocaloric measurements. The dynamics of magnetic properties of the Ni-doped FeRh has been studied using different sweep rates of the magnetic field: in the Halbach setup up to 2 T and in pulsed magnetic fields up to 14 T**.

3.1 Measurements of binary FeRh under cyclic conditions

3.1.1 Structural characterization

The sample of Fe₄₉Rh₅₁ composition was heat treated for 7 days at 1000°C in a sealed quartz tube under vacuum and then quenched into water. The sample characterization is presented in Fig. 3.1: an XRD diffraction pattern and the lattice parameters calculated from it; an SEM micrograph taken in the BSE mode and elemental composition determined by EDX. The sample consists predominantly of the CsCl-type (α') phase and a small amount of the paramagnetic fcc (γ) phase; the composition is close to the targeted 49-51 ratio. The amount of the fcc phase was found to be 3 vol %; that could possibly be a reason why the final composition is slightly off the intended one. The minor phase is typically neglected, especially in magnetic measurements, since it is paramagnetic and does not carry any significant contribution to the total magnetization.

*The experiments were carried out in collaboration with Dr. K.P. Skokov, TU Darmstadt

**The experiments in pulsed field were carried out in collaboration with Dr. Y. Skourski, HZDR

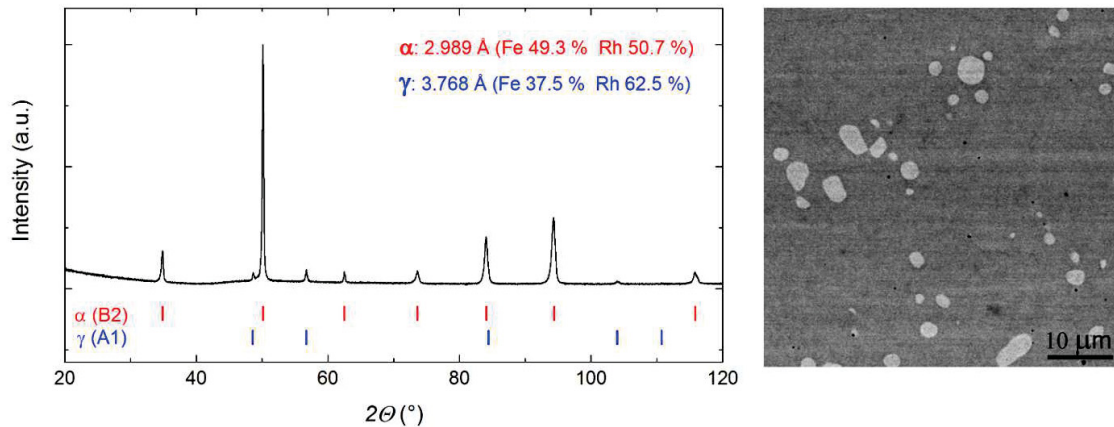


Figure 3.1 Room temperature X-ray diffraction pattern and lattice parameters of the major α' -phase and minor γ -phase, SEM-image taken in the BSE-mode and EDX analysis of the binary $\text{Fe}_{49}\text{Rh}_{51}$ alloy.

3.1.2 Evaluation of ΔS from magnetic measurements and calorimetry

The temperature dependence of magnetization $M(T)_H$ of $\text{Fe}_{49}\text{Rh}_{51}$ (Fig. 3.2a) was measured in selected magnetic fields up to 2 T on heating and cooling to determine the phase transition temperature, the shift of the transition with magnetic field and the width of the thermal hysteresis. According to the estimations made from $M(T)_H$ curves, in this sample the AF–FM transition occurs in zero magnetic field at 324.5 K on heating; the transition temperature upon increasing magnetic field shifts towards lower temperatures with the rate $dT/dH = -8.5$ K/T; the hysteresis width at the transition in 2 T is 7.5 K.

In order to investigate the nucleation and growth of the ferromagnetic phase, the major thermal hysteresis loop in the magnetic field of 1 T in the temperature range of 290–330 K was complemented by minor hysteresis loops (Fig. 3.2b). In this temperature interval the transitions to the FM state on heating and back to the AF state on cooling are both complete. The measurements of $M(T)_H$ were carried out by heating the sample from 290 K up to 314 K, 316 K, 318 K, and 322 K with subsequent cooling down to 290 K. On heating, at 318 K (point 2) the AF–FM transition is not fully complete and some part of the AF phase is still present in the sample. It is necessary to heat the sample above 330 K to turn the whole sample volume to the FM state. On cooling, at 308 K (point 3) the main part of the sample is already in the AF state, but still the FM phase is present in the sample (3–5 %) and only at 297 K (point 1) the whole sample volume is occupied by the AF phase. Those residual FM or AF inclusions below or above the transition temperature may act as nucleation centers and affect the hysteresis width when the magnetic field is reversed near the transition temperature. Heating the sample up to 316 K (point 4) and starting to cool, the sample is transforming back to the AF phase before the FM–AF transition temperature is observed in the major hysteresis loop. At this point the

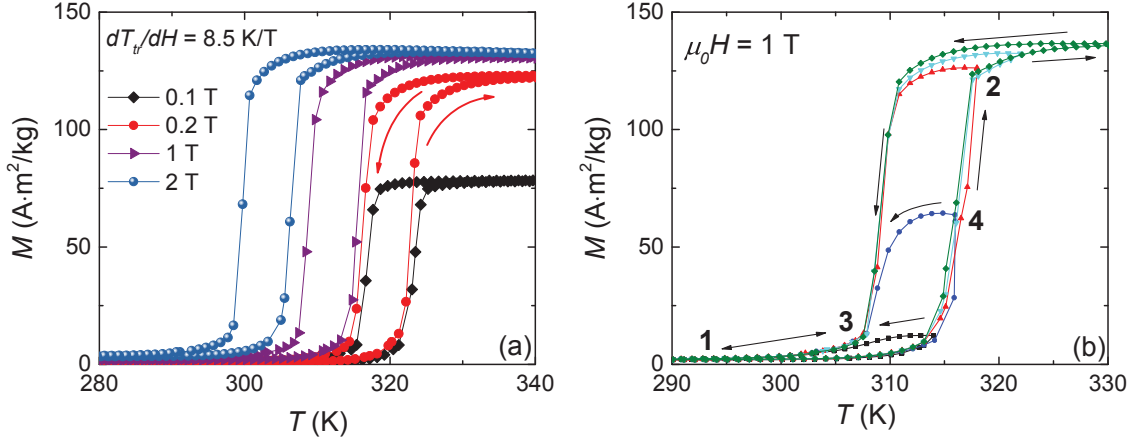


Figure 3.2 (a) Temperature dependences of the magnetization on heating and cooling in magnetic fields up to 2 T. (b) Minor thermal hysteresis loops in 1 T field.

sample volume consists of approximately equal amounts of the AF and FM phases. A similar behavior was reported earlier for Ni-Mn-In-Co [41] and was ascribed to a partial prevention of the nucleation of the martensite in the mixed phase region of minor loops which would require more energy than a simple phase boundary movement.

The entropy change at the AF–FM phase transition for the 2 T field was determined using three different methods: from magnetic measurements by the Clausius-Clapeyron equation, from magnetic measurements by Maxwell relations and from caloric measurements by integration of the heat capacity data. For the FeRh-type materials, it has been shown that the Maxwell relations can be successfully applied and the results of ΔT_{ad} measurements match perfectly the calculated values [124].

The simple estimation of the magnetic entropy change using the Clausius-Clapeyron equation ($dT/dH = \Delta M/\Delta S_{max}$) and the magnetization data ($dT/dH = -8.5$ K/T, $\Delta M = 129$ A · m²/kg) gives $\Delta S_{max} = 14.3$ J/(kg · K). In order to use the Maxwell relation

$$\Delta S(T)_{\Delta H} = \int_{H_I}^{H_F} \frac{\partial M(T, H)}{\partial T} \Delta H, \quad (10)$$

the magnetization dependence $M(T)$ was measured on heating and cooling with a magnetic field step of 0.1 – 0.25 T. In Fig. 3.3 the heating curves are shown, as well as the ΔS dependences calculated by the Maxwell relation. Upon increasing the magnetic field in the range of 0.1 T – 2 T, the effective range of ΔS broadens, while the ΔS value increases, and at $\Delta \mu H = 2T$ the entropy change $\Delta S_{max}(2T) = 13.6$ J/(kg · K). Calculating the entropy change using the $M(T)_H$ dependence measured on cooling, a set of $\Delta S(T)$ curves in the same fields is used that is similar in shape and value but opposite in sign. Combining the positive and negative $\Delta S(T)$ at a particular field, it is possible to define the temperature range to which the reversibility of the MCE should be restricted [114].

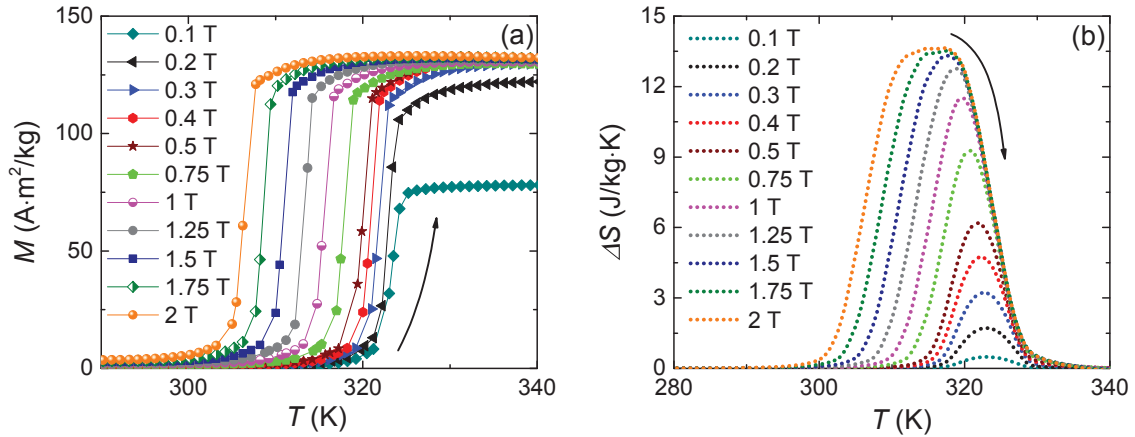


Figure 3.3 (a) Temperature dependence of the magnetization measured on heating in fields up to 2 T. (b) Entropy change calculated from $M(T)$ using Maxwell relations.

Further, for the calculation of ΔS from caloric measurements, the temperature dependence of the heat capacity was measured in different magnetic fields. The measurements before and after the transition were carried out using the standard relaxation calorimetry ($2\text{-}\tau$ method) [158], whereas for the quantitative estimation of the heat capacity in the phase transition region the method described by Suzuki *et al.* [159] was applied. The measured $C(T)_H$ dependences for $\mu_0 H = 0$ and $\mu_0 H = 2$ T are shown in Fig. 3.4a. The temperature dependence of the entropy $S(T)_H$ can be calculated by integration of $C(T)_H$:

$$S(T)_H = \int_0^T \frac{C_H(T)}{T} dT \quad (11)$$

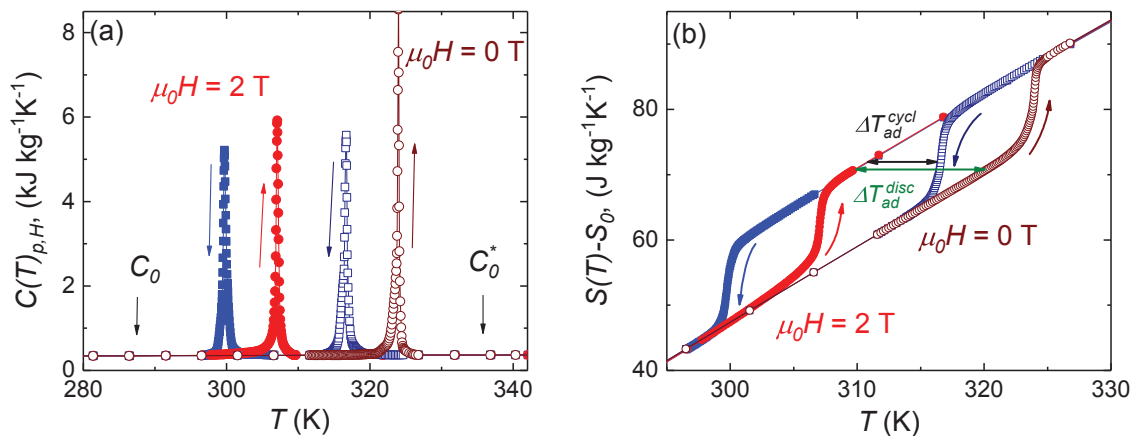


Figure 3.4 (a) Temperature dependence of the heat capacity measured through the phase transition on heating (red) and cooling (blue) without field application (open symbols) and in a 2 T field (closed symbols). (b) $S - T$ diagrams obtained by integration of the heat capacity data. The arrows show the direction of the temperature change.

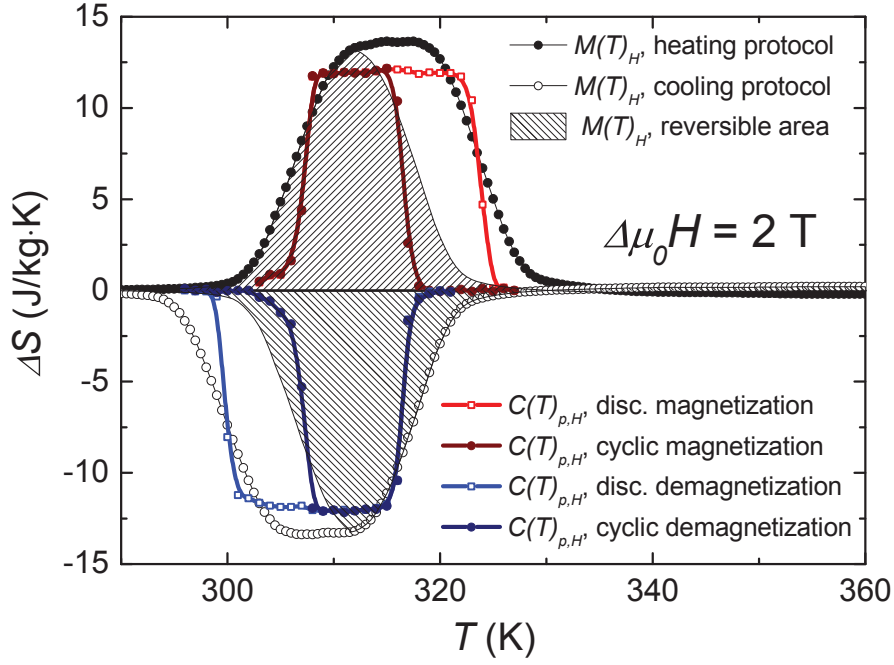


Figure 3.5 Magnetic entropy change estimated independently from magnetic measurements using Maxwell relations and from caloric measurements using $S-T$ -diagram built on the heat capacity data. The shaded area shows the range where the reversibility of the magnetocaloric effect is expected.

The calculated $S(T)_H$ data were used to construct the $S - T$ diagrams (Fig. 3.4b) with and without magnetic field, from which the adiabatic temperature change can be evaluated (as in [15], shown by the green arrow in Fig. 3.4b). The $S(T)_H$ dependences also allow a second way to calculate ΔS via:

$$S(T)_H^{0 \rightarrow H}(T) = \int_0^T \frac{[C_H(T)_{H=0} - C_H(T)_{H \neq 0}]_P}{T} dT \quad (12)$$

Just as in the case of ΔS derived from Maxwell relations, these temperature dependences correspond to the discontinuous protocol described earlier in Section 2.3.2: this value of $\Delta S(T)$ is possible to obtain only by (1) heating up the sample from the AF state in zero field to the temperature T and then applying the magnetic field or (2) cooling the sample from the FM state in magnetic field to the temperature T and then reducing the field to zero. These $\Delta S(T)$ values are important for the general characterization of the material and represent the entropy change of the sample at the completed AF–FM or FM–AF transitions. Under cycling in magnetic field, the transition may remain incomplete. For the determination of the reversible entropy change it is possible to use a procedure suggested by Skokov *et al.* [164] defining ΔS_{cycl} as the difference of $S(T)_{H=0}$ on heating and $S(T)_{H=2T}$ on cooling.

The temperature dependences of ΔS obtained from the discontinuous approach and

under cyclic conditions are shown in Fig. 3.5: the dependences derived from calorimetric measurements as $\Delta S = S(T)_{H=0} - S(T)_{H=2T}$ are shown as red open squares on heating (positive values) and blue open squares on cooling (negative values) along with the dependences derived from $M(T)$ measurements using Maxwell relations (circles) for a 2 T magnetic field. The cyclic values obtained from the difference of the $S(T)$ -curves on heating and cooling are plotted using closed squares. They match the shaded area that indicates the region where the reversibility of the MCE should be expected from magnetic measurements [114]. It can be seen that generally the calorimetric data agree very well with the calculations by Maxwell relations, however the maximal value ΔS obtained from the $S - T$ diagram is lower: $\Delta S_{max} = 12.1 \text{ J}/(\text{kg} \cdot \text{K})$. Obviously, the temperature range where the material exhibits high values of ΔS_{cycl} is limited to 309-319 K.

Using the values of the magnetic entropy change obtained by different methods $\Delta S_{max} = 14.3 \text{ J}/(\text{kg} \cdot \text{K})$ (from the Clausius-Clapeyron equation), $\Delta S_{max} = 13.6 \text{ J}/(\text{kg} \cdot \text{K})$ (from Maxwell relations) and $\Delta S_{max} = 12.1 \text{ J}/(\text{kg} \cdot \text{K})$ (from the $S - T$ diagram), an estimation of the highest possible adiabatic temperature change at the AF–FM transition can be done as:

$$\Delta T_{(ad,max)} = \frac{T_{tr}}{C_0} \Delta S_{max} \quad (13)$$

Here $C_0 = 353 \text{ J}/(\text{kg} \cdot \text{K})$ (or $C_0^* = 360 \text{ J}/(\text{kg} \cdot \text{K})$) is the heat capacity value right before or after the transition (see Fig. 3.4). Applying Eq. 13 to the obtained values, it can be seen that $\Delta T_{(ad,max)}$ should be in the range of 10.6-13.2 K. This is quite close to $\Delta T_{ad} = 12.9 \text{ K}$ (in $\Delta\mu_0 H = 2 \text{ T}$) reported by Nikitin *et al.* [4].

3.1.3 Direct measurements of ΔT_{ad} in the Halbach setup

The field dependence of the adiabatic temperature change $T(H)$ in the case of an idealized transformation scenario can be schematically presented using an $H - T$ diagram (Fig. 3.6a, see also [165]). In this diagram $T_{tr} = 324.5 \text{ K}$ corresponds to the AF–FM transition observed in $\text{Fe}_{49}\text{Rh}_{51}$ on heating in zero field, and $T_{tr} = 317 \text{ K}$ corresponds to the reverse FM–AF transition observed on cooling (temperature hysteresis 7.5 K).

In a magnetic field, both transition temperatures $T_{tr}(\text{AF–FM})$ and $T_{tr}(\text{FM–AF})$ are shifted down with the rate $dT/dH = -9 \text{ K/T}$ forming the phase boundaries that separate ferro- and antiferromagnetic states on cooling and heating (diagonal lines in Fig. 3.6a). Above the AF–FM line the sample will always be in the FM state, below the FM–AF line in the AF state, and in the range of fields and temperatures between those lines (white area) the AF and FM phases can coexist depending on the sample history.

The discontinuous protocol implies heating up the sample in zero field, for example, from 300 K to 324 K. So, at point 1 in Fig. 3.6a the whole sample volume still consists of the AF phase. Then the adiabatic cycle begins. First, upon field increase (section

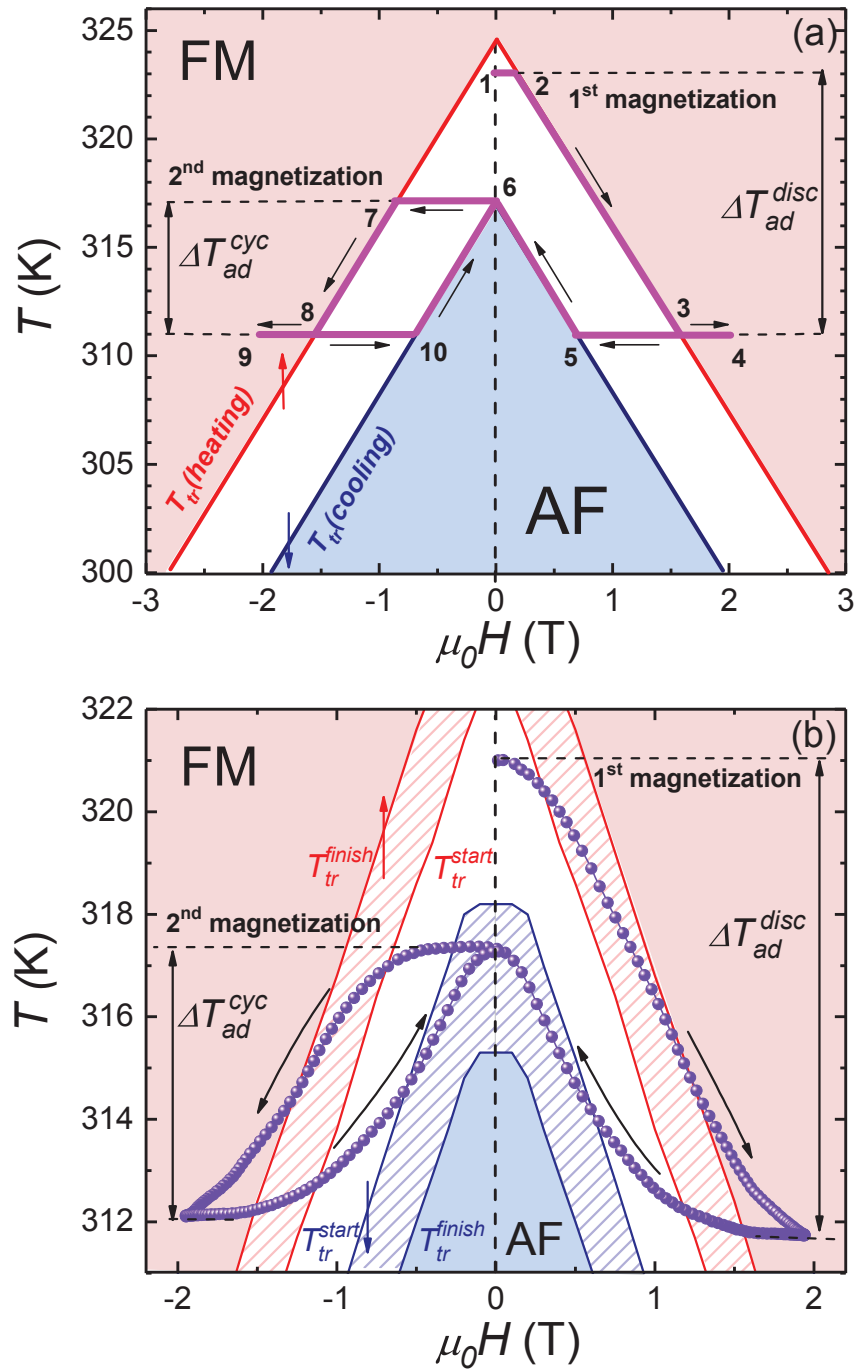


Figure 3.6 Temperature change obtained in adiabatic conditions during a magnetic cycle $0 T \rightarrow 2 T \rightarrow -2 T \rightarrow 0 T$ shown (a) for an idealized AF–FM transformation and (b) for an initial temperature $T = 321$ K in the real sample, where the hashed area shows temperature regions between the start and finish of the AF–FM transition, marked red on heating and blue on cooling.

1-2) there is no change in the sample temperature, but as soon as $T(H)$ approaches the AF–FM phase boundary (point 2), the AF–FM transition begins and the sample temperature lowers following the AF–FM line [165]. If the magnetic field is sufficient for the transition to be completed, the temperature will change until reaching the maximal $\Delta T_{ad} = 12$ K (point 3), and after that it should stop changing. The calculations of this maximal adiabatic temperature change ΔT_{ad} were carried out using Eq. 13 based on the value of ΔS_{max} estimated using Maxwell relations. At this point the whole sample volume consists of the FM phase and a further field increase does not lead to any significant temperature change (section 3-4). Upon a field decrease, the reverse FM–AF transition can only begin when the field dependence $T(H)$ approaches the corresponding phase boundary (point 5). Starting from that moment a further field decrease is accompanied by a rising temperature caused by the reverse transition. However, now that the magnetic field returns to zero (point 6), the reverse temperature change is significantly smaller because the transition is not complete and both AF and FM phases coexist within the sample. Applying a negative magnetic field (section 6-7-8-9), the maximal temperature change on section 7-8 will be defined only by the initial ratio of the AF and FM phases at point 6. A further field decrease (section 10-6) results in an equal by magnitude but opposite by sign temperature change of 6 K that can be considered as ΔT_{ad} under cycling.

The experimentally obtained $\Delta T_{ad}(H)$ dependence is shown in Fig. 3.6b. The measurements were carried out using the discontinuous protocol (heating up to 350 K, cooling down to 250 K and zero field heating to 321 K). At 321 K the magnetic cycle was carried out as $0 \text{ T} \rightarrow 1.93 \text{ T} \rightarrow 0 \text{ T} \rightarrow -1.93 \text{ T} \rightarrow 0 \text{ T}$. During the first magnetization, the maximal ΔT_{ad} is 9.2 K, which is considerably lower than the value of 12 K, derived from the analysis of the idealized $H - T$ diagram. As expected, after the field removal due to the hysteresis it is not possible to come back to the original point of 321 K, so the cycle proceeds from $T = 317.3$ K to negative fields yielding a smaller value of $\Delta T_{ad} = 6.2$ K. Comparing field dependences $\Delta T_{ad}(H)$ presented in Fig. 3.6a and Fig. 3.6b, it can be seen that qualitatively the experimental dependence fits well the model curve obtained using the $H - T$ diagram.

The relatively low experimental ΔT_{ad} at the first magnetization can be explained by several reasons, for example, a presence of strain that can cause an effective reduction of the transition temperature [40], a distribution of the transition temperature for different grains in the sample [166] or an influence of the demagnetizing factor [37]. The effect of the abovementioned reasons can be well seen on the temperature dependence of the magnetization (Fig. 3.2). For example, for a 1 T field on heating, the AF–FM transition begins at 313.6 K and ends at 319 K, giving a transition width of 5.4 K. As a result, on the real $H - T$ diagram AF–FM and FM–AF phase boundaries should be drawn not as lines but as regions of width 5.4 K as shown in Fig. 3.6b. This approach was earlier used to explain the hysteretic phenomena during isothermal processes [167–169].

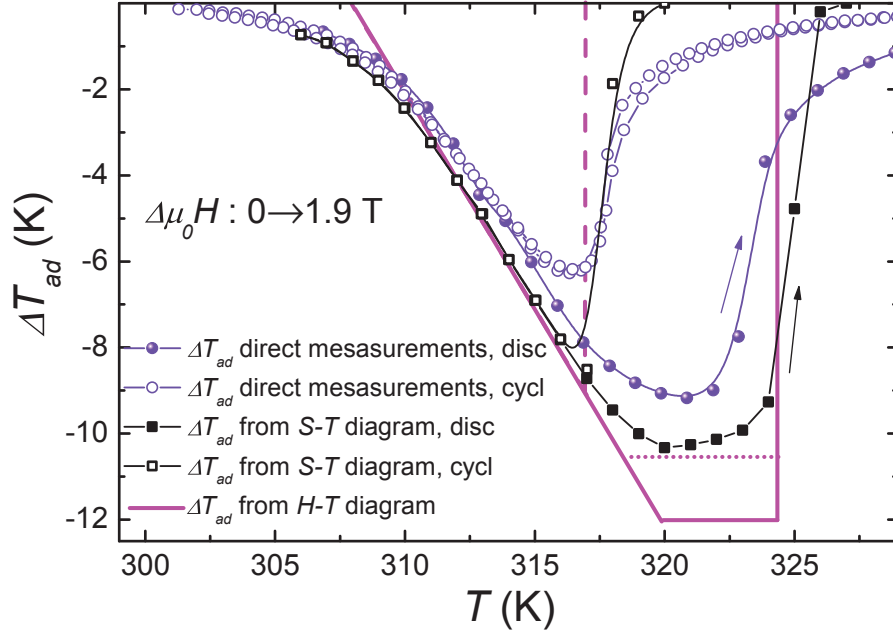


Figure 3.7 Adiabatic temperature change measured directly (circles) and evaluated from calorimetric and magnetic measurements (squares): at the first field application (closed symbols) and under cycling (open symbols). The solid and dashed lines are obtained from the $H - T$ diagram and estimate the maximal effect in an ideal case at the first field application and under cycling, respectively.

This broadening of the phase boundaries inevitably leads to a lowering of the $\Delta T_{ad}(H)$ slope and, as a result, lowers the real ΔT_{ad} value relative to the value of 12 K shown in Fig. 3.6a.

As demonstrated in Fig. 3.6, from each cycle two values of ΔT_{ad} are derived: ΔT_{ad}^{disc} representing the completed metamagnetic transition and ΔT_{ad}^{cyc} accounting for the hysteresis effect. These values comprise the temperature dependence of the adiabatic temperature change measured under discontinuous protocol and under cycling (Fig. 3.7). The experimental $\Delta T_{ad}(T)$ values obtained after the first magnetization (branch 0 T \rightarrow 1.93 T in Fig. 3.6) are shown as closed circles. The values obtained at the second magnetization (branch 0 T \rightarrow -1.93 T \rightarrow 0 T) and further under cycling are shown as open circles. The $\Delta T_{ad}(T)$ dependence determined from the $S - T$ diagram (squares) and the $H - T$ diagram (lines) can also be found in Fig. 3.7. Besides, the reversible $\Delta T_{ad}(T)$ defined from the $S - T$ diagram is shown, and also the reversible $\Delta T_{ad}(T)$ defined from the $H - T$ diagram.

There is a good agreement in the temperature range of 305-317 K, where a magnetic field of 1.9 T is not sufficient for a completion of the transition and the AF phase only partly transforms to FM. On the contrary, in the temperature range of 318-324 K where the AF-FM transition is almost complete, the curves obtained by different methods split

significantly. As can be seen, in the case of FeRh, the quasi-static calorimetry under the discontinuous protocol gives somewhat overestimated values ($\Delta T_{ad,max} = 10.3$ K) in comparison with the value obtained as a result of the direct measurements ($\Delta T_{ad,max} = 9.2$ K). On the other hand, considering the difficulties of the heat capacity measurements of samples with a first order transition and a broad temperature hysteresis, estimation of $\Delta T_{ad,max}$ from the $S - T$ diagram can be considered as quite appropriate. The upper limit of $\Delta T_{ad}(T)$ obtained from the idealized $H - T$ diagram also shows an overestimated value. This estimation is done for the case of $\Delta S_{max} = 13.6$ J/(kg · K) (Maxwell relations, solid line) and $\Delta S_{max} = 12.1$ J/(kg · K) (calorimetric measurements, dashed line). As discussed earlier, this discrepancy can be caused by the transition temperature distribution in the grains of a real sample, which lowers the possible MCE and which is not accounted for in the idealized $H - T$ diagram.

3.2 Dynamics of the magnetocaloric effect in Ni-doped FeRh

3.2.1 Structural characterization

The sample of $(\text{Fe}_{0.98}\text{Ni}_{0.02})_{49}\text{Rh}_{51}$ composition was heat treated for 10 days at 1000°C and then quenched into water. The structural analysis can be found in Fig. 3.8: an XRD diffraction pattern and the lattice parameters calculated from it; an SEM micrograph taken in the BSE-mode and the elemental composition determined by EDX. The sample consists predominantly of the CsCl-type (α') phase and a small amount of the paramagnetic fcc (γ) phase; the composition is close to the targeted ratio. The amount of the fcc phase is higher than in the binary sample (6 vol %). The lattice parameter of the main α' -phase is larger than in the binary alloy, but as can be seen further, this is due to a different magnetic state at room temperature: the Ni-doped FeRh has a lower transition

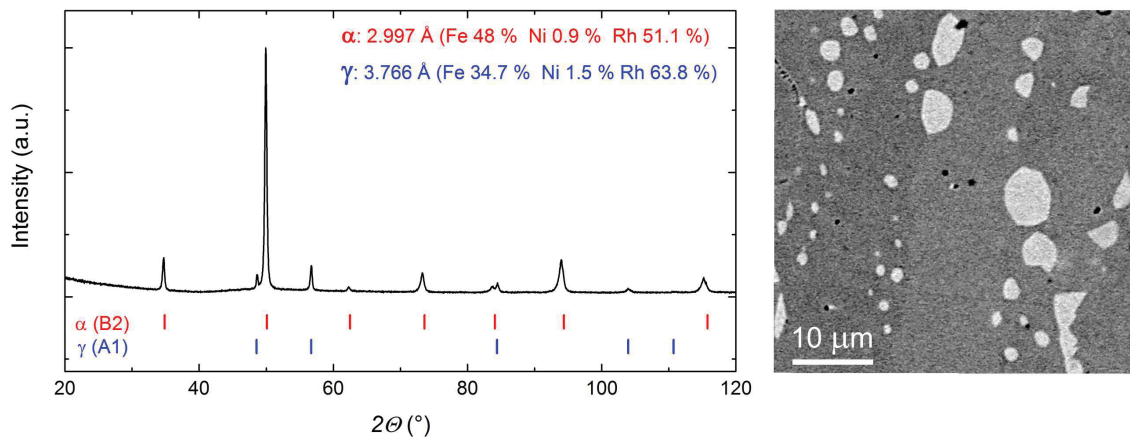


Figure 3.8 Room temperature X-ray diffraction pattern and lattice parameters of the major α' -phase and minor γ -phase, SEM-image taken in the BSE-mode and EDX analysis of $(\text{Fe}_{0.98}\text{Ni}_{0.02})_{49}\text{Rh}_{51}$ alloy

temperature and therefore is already in the FM state that is characterized by a 1 % higher volume of the unit cell.

3.2.2 Dynamical effects evidenced from magnetization measurements

The nucleation and growth of the ferromagnetic phase in the Ni-doped alloy observed by minor thermal hysteresis loops (Fig. 3.9a) occurs principally in the same fashion as in the binary FeRh (see Fig. 3.2b). The transition temperature is lower due to the Ni-doping that is known to reduce the AF–FM transition temperature [69]. The hysteresis has increased to 9.5 K. A larger hysteresis is somewhat typical for FeRh-based alloys when the transition is shifted towards lower temperatures [69]. A minor loop area can be used as an estimation of the transformed volume [78]. The mixed state between 240 K and 250 K can be quite interesting in terms of analysing the system response to the magnetic field and connecting the maximum of the reversible adiabatic temperature change with the volume of the FM phase at a particular temperature. For example, approximately at 317 K, the maximum of the reversible effect in the binary FeRh (Fig. 3.7) is observed, and exactly at this temperature is the highest magnetization point (i.e. FM phase amount) (Fig. 3.2b point 2) before the transition goes to saturation.

Due to a lower transition temperature of (Fe,Ni)Rh, the quasistatic magnetic field in the conventional QD 14T PPMS is sufficient to complete the AF–FM transition in this sample even at very low temperatures, as can be seen in Fig. 3.9b. The temperature dependence in different fields was first measured on field-cooling and then on heating. The magnetic field strongly affects the transition temperature and stabilizes the FM state. Beside the shift of the transition and the hysteresis broadening, there is an increasing amount of the residual FM phase at low temperatures when the sample is cooled down

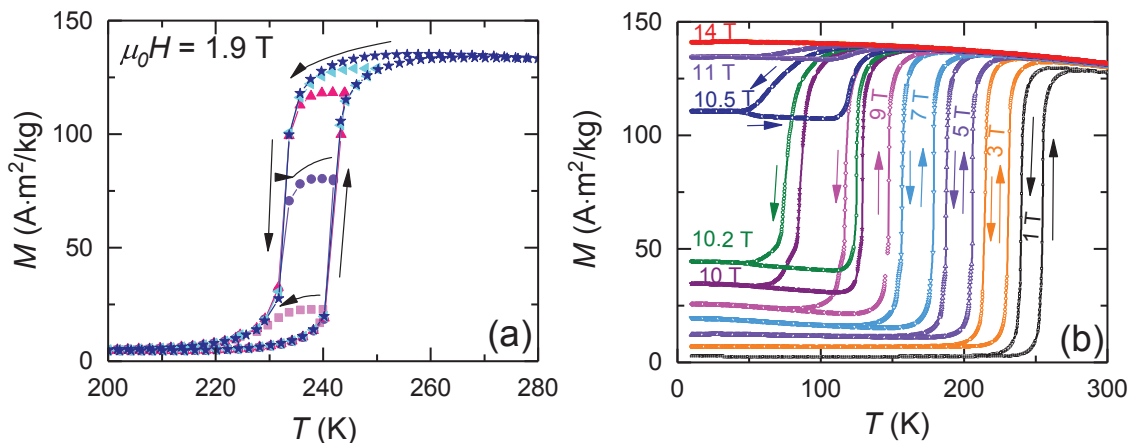


Figure 3.9 (a) Thermal minor loops of the Ni-doped FeRh measured in a field of 1.9 T. (b) Temperature dependences of magnetization measured on cooling and heating in fields up to 14 T.

from room temperature. At a magnetic field of 9 T and higher, the shift of the transition temperature slows down significantly, but the amount of the residual FM phase continues to increase rapidly; at 14 T only the FM state exists in the whole temperature region.

On one hand, this change in the transition temperature shift is in agreement with the quadratic dependence of the critical fields suggested for FeRh by McKinnon *et al.* [82], later also observed in Ni and Pd substituted FeRh [69, 81] down to low temperatures complemented by the data of the reverse FM–AF transition. Considering the magnetic phase diagram, it should occur due to the hysteretic region where the mixed state is present at particular values of temperature and magnetic field. Moreover, it has been noticed that it is typical for the magnetic transitions that are accompanied by significant changes in the electronic structure [85]. On the other hand, the attempts to explain the nature of coexisting AF and FM phases address the kinetics of the AF–FM transition, and claim a glassy dynamics or the arrest of the kinetics of the phase transition at low temperatures [79, 81]. However, there are few works on this subject and a lack of agreement, so further investigation is required. Without doubts, the behavior of the AF–FM transition in FeRh changes in the range of 80-120 K, and it can even be due to another phase transformation, as indicated from recent theoretical considerations [170].

At temperatures below 10 K, the character of magnetization curves changes to peculiar jumps, most pronounced at 2 K (Fig. 3.10a). At 30 K the magnetization curve looks conventional. This behavior below approximately 10 K seems to be characteristic of FeRh-type alloys, as shown earlier during experiments under pressure in Pd-doped FeRh [171], where this phenomenon was not further investigated. The low temperature region is poorly investigated compared to the most attractive range of the AF–FM phase transition where the giant magnetocaloric effect is observed, and this range typically is not lower than 120 K, according to the data reported over years.

Incidentally, the phenomenon of the avalanche-like magnetization behavior at low temperatures has been reported for different classes of materials with metamagnetic transitions. Extremely sharp magnetization steps separated by plateaus have been observed and discussed in polycrystalline and single crystal manganites below 5 K [172, 173], in a spinel oxide FeV_2O_4 between 5 and 2 K [174] and in an itinerant electron system $\text{LaFe}_{12}\text{B}_6$ at 2 K [175, 176]. Presumably, only a fraction of the sample transforms to the FM state during one step; the plateaus correspond to a metastable state. Relaxation measurements performed for $\text{LaFe}_{12}\text{B}_6$ at 2 K in magnetic fields near the first jump resulted in a spontaneous metamagnetic transition, which is an indication that the phenomenon of the avalanche-like magnetization is not solely driven by a change in the magnetic energy term [176]. The reproducibility of the staircase-like behavior was tested for several samples from the same batch of $\text{LaFe}_{12}\text{B}_6$ with Ce substitution, and was found to be remarkable [177].

A systematic investigation of magnetic polarization jumps observed in Sm-Co magnets

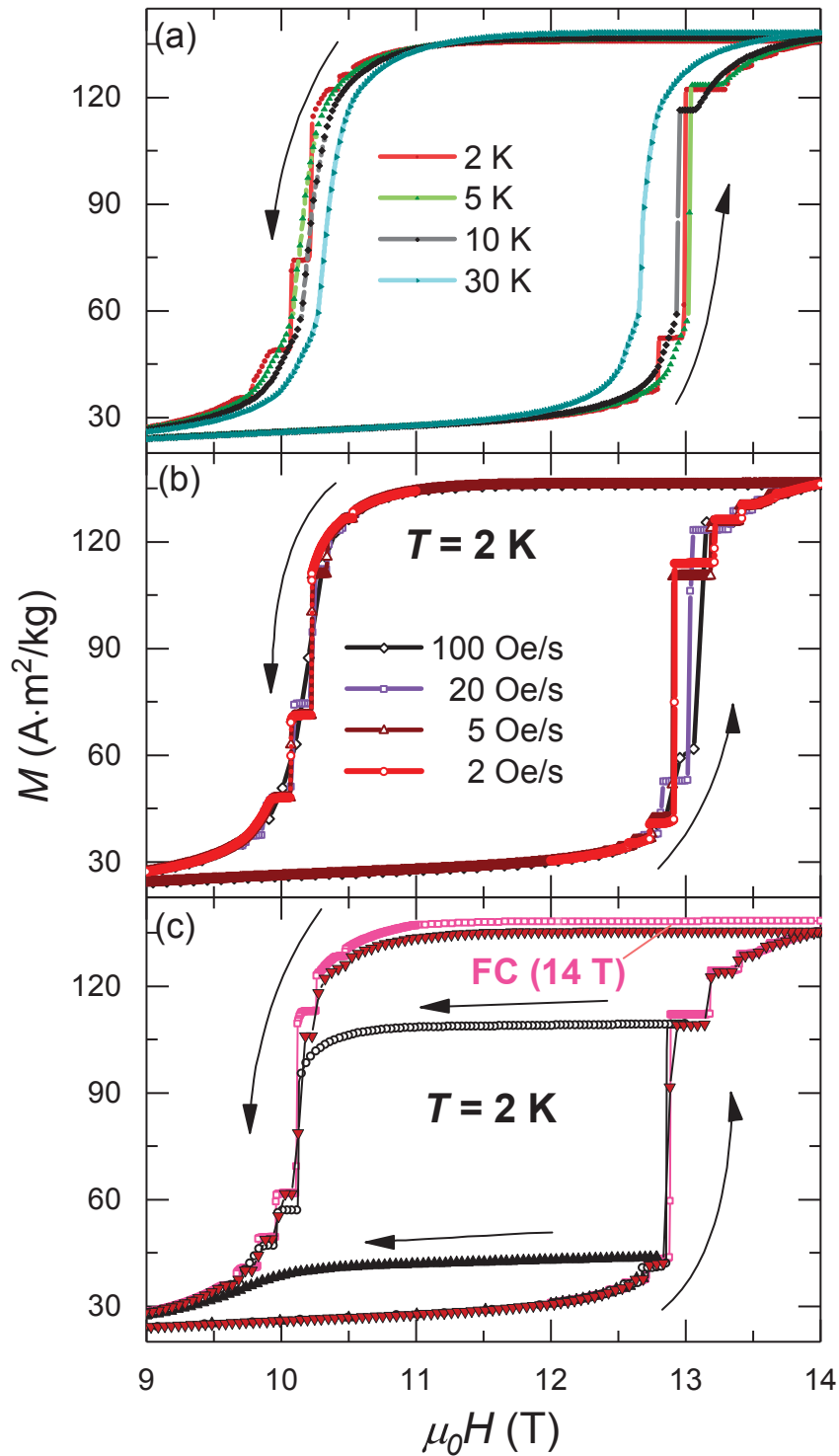


Figure 3.10 (a) Magnetization loops of Ni-doped FeRh measured at temperatures from 2 to 30 K. The jumps of magnetization are observed below 10 K (b) Magnetization loops at 2 K measured at different field sweep rates. (c) Minor magnetization loops at 2 K as well as the complete loop measured after field cool in 14 T to ensure the best ferromagnetic state.

showed that the emergence and the number of the jumps depend on the temperature, a field sweeping rate and sample dimensions [178], in particular, at a lower field sweeping rate the number of jumps was reduced. In Fig. 3.10b, a comparison for different field sweeping rates of 2-100 Oe/s is shown: the appearance of the magnetization jumps is not affected, at least at 2 K, but there is a difference in the transition field of the largest step. The resolution of the measurement at the sweep rate of 100 Oe/s was too low to detect any jumps. In any case, the fact that the magnetization steps appearance is independent of the sweep rate in the range of 2-20 Oe/s is an indication that this effect is not caused by a thermal effect, moreover, at the lowest field sweeping rate the jumps become particularly sharp and clear. To complete the picture, in Fig. 3.10c minor loops are shown, as well as a full magnetization loop after field cooling in 14 T (pink squares). A demagnetization curve after field cooling in 14 T occurs at practically the same magnetization, as after ZFC and magnetizing to 14 T, which means that the field of 14 T is enough to complete the transition at 2 K in the latter case.

The origin of the magnetization jumps is still a matter of controversy. Comparing to the magnetizing process in permanent magnets, similar jumps were generally attributed to thermal instabilities [178]. Thermal instabilities at a jump can be ascribed to a thermoactivated avalanche of irreversible magnetization rotations due to the small lattice specific heat at low temperatures [179].

The avalanche-like dynamics of the FM phase growth can also be discussed on the base of macroscopic quantum tunneling of ferromagnetic domain walls accompanied by pinning on impurities. It has been shown that the tunnelling of domain walls at temperatures of a few Kelvin is possible under certain circumstances: if the wall width is only a few lattice constants [180]. Quantum tunnelling through the barrier was also suggested as a trigger for the irreversible propagation of the domain walls that may explain the anomalies in the magnetization reversal curves below 10 K in Nd-Fe-B permanent magnets [181]. Additionally to the domain wall pinning effect, the stray field of the growing FM phase in a non-magnetic matrix may contribute to the plateau observed in the magnetization, compensating for the increase of the external field.

The most prominent interpretation of the avalanche-like field-induced transformation is a martensitic scenario [172, 175, 182]. The FM regions developing inside the non-magnetic matrix result in strain effects at the interfaces due to pronounced differences between the crystallographic unit cells of the coexistent magnetic phases. As the applied magnetic field is continuously increased, its driving force acts on the magnetic moments in order to extend the FM regions, but has to overcome the interfacial constraints. When the field is large enough to overcome the elastic constraints at the interfaces, the FM phase evolves in a catastrophic manner, generating an abrupt magnetization jump. During this process, a balance between the changing magnetic and elastic energies can lead the system to be frozen in a metastable state, corresponding to a plateau. Thus, the

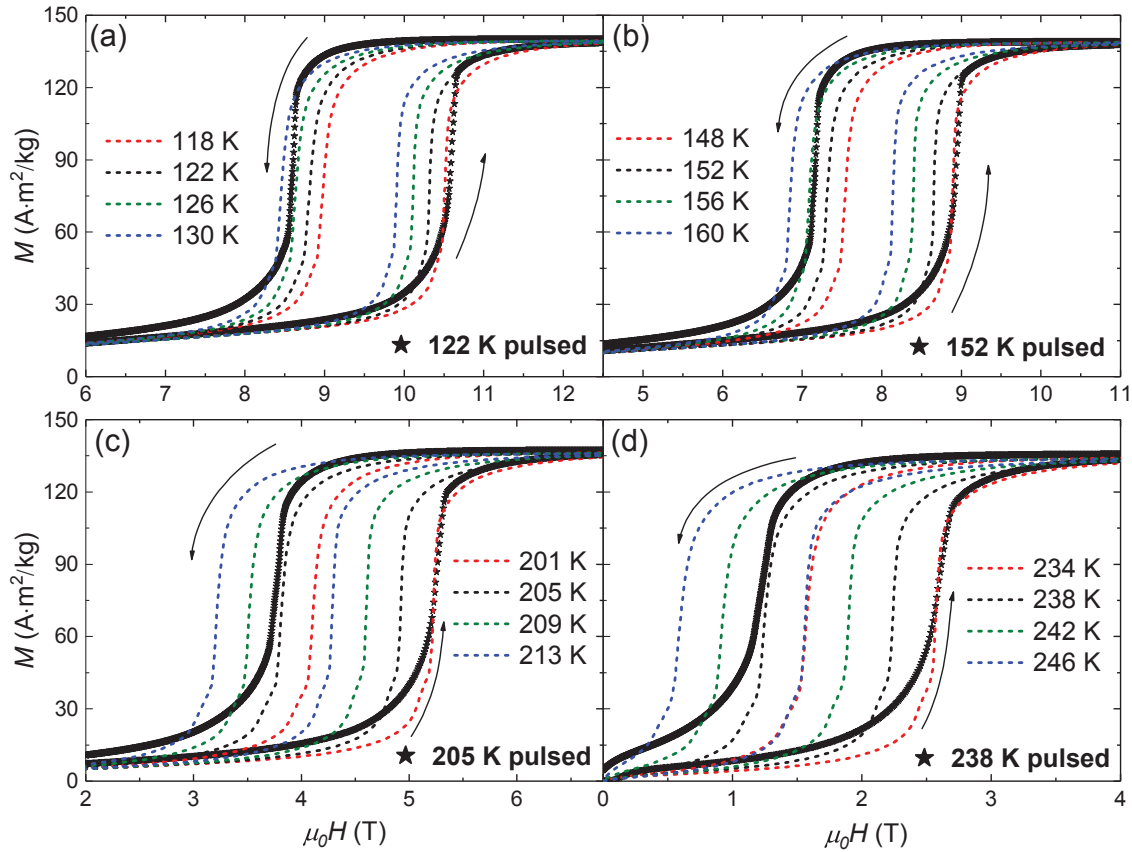


Figure 3.11 Magnetization loops measured under adiabatic conditions in pulsed fields (stars) and isothermal conditions in quasistatic fields (dashed lines) at selected temperatures. Black color is used for the same temperatures under different conditions.

transition proceeds by a succession of abrupt steps between metastable states.

Magnetization loops at higher temperatures have been measured under different conditions: in quasi-stationary field in QD PPMS in isothermal conditions, and under adiabatic conditions in pulsed fields of the HLD HZDR facility. Both kinds of magnetization loops are shown in Fig. 3.11. A difference in the shape of the loops can be observed. Earlier, a mismatch between the adiabatic curves measured in pulsed fields and the isothermic curves obtained using a superconductive magnet was found for $\text{La}(\text{Fe,Si,Co})_{13}$ [183]. Critical fields were higher for the pulsed field process, and the explanation was that the magnetization is affected due to the heating up of the sample at the critical field region due to the adiabatic conditions. This can also be used for an indirect estimation of the adiabatic temperature change [184]. In the case of $\text{La}(\text{Fe,Si,Co})_{13}$ it is a second order transition, and this assumption agrees well. However, in the case of FeRh, this approach does not seem to work because the critical field in the adiabatic process is higher, but the ΔT_{ad} in FeRh is negative, whereas in $\text{La}(\text{Fe,Si,Co})_{13}$ it is positive. Therefore, there must be another mechanism working additionally. Also, in $\text{La}(\text{Fe,Si,Co})_{13}$, the field is

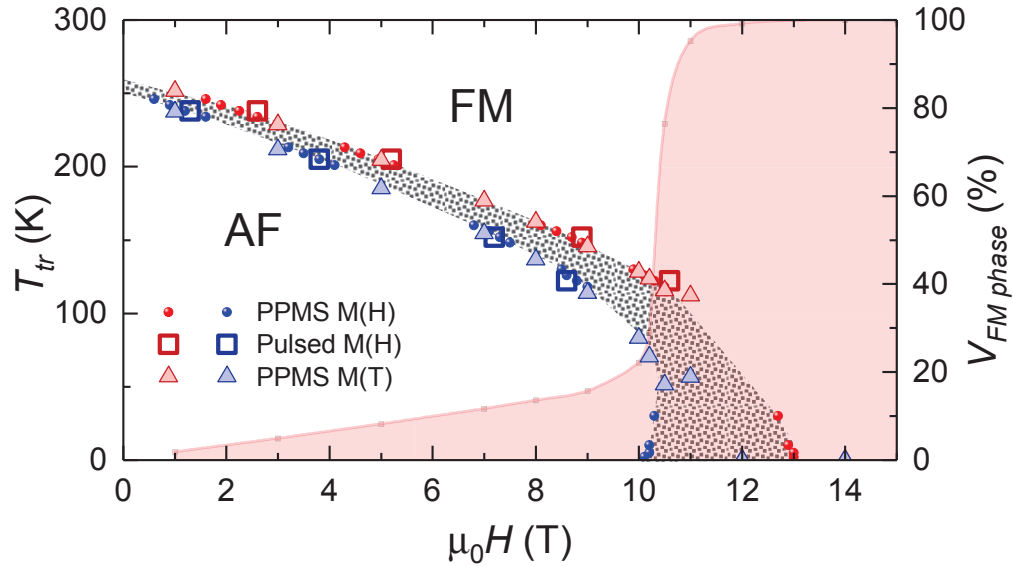


Figure 3.12 Magnetic phase diagram of $(\text{Fe}_{0.98}\text{Ni}_{0.02})_{49}\text{Rh}_{51}$. Red symbols mark the field/temperature "up" and blue – "down". Below the line traced by the blue symbols only the AF state exists, and above the red ones only the FM state. The hysteresis area is hashed. The red area shows the fraction of the retained FM phase observed at low temperatures upon the field increase from 0 to 14 T.

equally shifted to the higher temperatures, whereas in FeRh the up-field is shifted in that direction, but the down field is shifted to the lower temperatures making the hysteresis under adiabatic conditions much larger than in the isothermal case. If the hysteresis is considered as an analogy to work in the magnetization-demagnetization cycle, it seems like the pulsed field has to work more to complete the transition in both directions. Considering that the lattice resists the transition, one can imagine that this resistance at a higher field rate bears a resemblance to an internal friction.

Based on the measurements of magnetization in pulsed and stationary fields, a magnetic phase diagram has been constructed (Fig. 3.12). The diagram shows regions of existence of the AF state and the FM state, the red symbols show which magnetic field value is sufficient to transform the whole sample to the FM state, the blue symbols show below which field value only the pure AF state will exist. This is applied only to the part of the sample that actually transforms between the AF and FM states. The initial fraction of the retained FM phase at low temperature, increasing with magnetic field, is shown as a red area. At first both the critical field dependence and the growing amount of the FM phase follow a linear dependence, however, at approximately 100 K this behavior rapidly changes. Earlier the whole dependence of the critical fields was fitted by a quadratic dependence [82], although it can be questionable whether it is really so, since the low-field region looks suspiciously linear, but usually it was ascribed to the magnetocaloric effect in that region. In fact it may be that there are two different dependences and moreover,

a magneto/structural transition, as has been recently predicted theoretically [170]. Generally, the broadening of the hysteresis towards low temperatures and the deflection of the dH/dT from the linear character has been known since long.

3.2.3 Evaluation of the MCE from magnetic measurements and calorimetry

Measurements of the heat capacity in the region of the magnetostructural transition were carried out in 1.9 T and 14 T magnetic fields, as well as without field, as shown in Fig. 3.13a. The data integration allows to construct an $S - T$ diagram for these fields (Fig. 3.13b) and to estimate $\Delta S(T)$ and $\Delta T_{ad}(T)$.

The estimation of the entropy change in a 2 T field from the temperature dependence of the magnetization measured on heating and cooling with a step of 0.2 T was per-

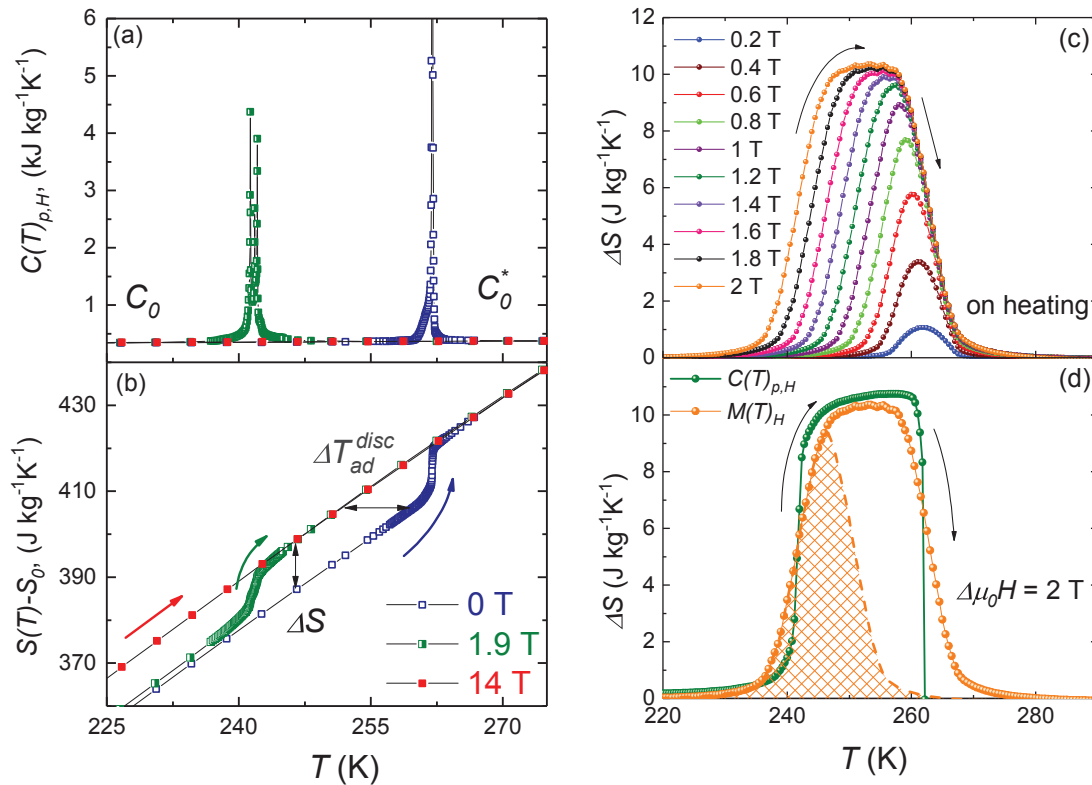


Figure 3.13 (a) Temperature dependences of the heat capacity measured through the phase transition on heating without magnetic field (blue), in 1.9 T (green) and 14 T (red). (b) $S - T$ diagrams obtained by integration of the heat capacity data. The arrows show the direction of the temperature change. (c) Entropy change calculated from magnetic measurements using Maxwell relations in various fields up to 2 T (d) Entropy change in 2 T field estimated from Maxwell relations and the $S - T$ diagram. Shaded area shows the range of the reversible MCE.

formed using Maxwell relations in the same fashion as in Section 3.1. The temperature range of the reversible MCE has also been estimated. The $\Delta S(T)$ on heating in different fields is shown in Fig. 3.13c. The magnetization curves are not shown; the zero-field AF–FM transition would occur at 266.5 K, and the shift of the transition with magnetic field is $dT/dH = -11$ K/T. The change of the magnetization at the transition is estimated as $\Delta M = 127$ A · m²/kg. Therefore, the estimation of the maximal magnetic entropy change using the Clausius-Clapeyron equation gives $\Delta S_{max} = 11.5$ J/(kg · K). The estimation done by Maxwell relations is 10.3 J/(kg · K), which is lower than for Fe₄₉Rh₅₁. In Fig. 3.13d, $\Delta S(T)$ at 2 T calculated by Maxwell relations is compared to ΔS estimated from the $S - T$ diagram: a very good agreement is found. These temperature dependences correspond to the discontinuous protocol, i.e. it is possible to obtain this value of $\Delta S(T)$ only by heating the sample from the AF state in zero field to the target temperature and then applying the magnetic field. In this Ni-doped FeRh sample, the maximal value of the entropy change is roughly 20 % lower than in the binary compound, although the temperature range where the material should exhibit high values of $\Delta S_{M,cycl}$ is two times broader and extends over 20 K from 236 K to 256 K compared to the 10 K range (309-316 K) in Fe₄₉Rh₅₁. Using the estimated values of the maximal entropy change and the heat capacity value before the transition $C_0 = 367$ J/(kg · K), the maximal expected $\Delta T_{(ad,max)}$ at the AF–FM transition should be 7.5-8.3 K.

3.2.4 Direct measurements of ΔT_{ad} in the Halbach setup and in pulsed fields

The dynamics of the MCE in (Fe,Ni)Rh was investigated by direct measurements of the ΔT_{ad} using two different sources of magnetic field: the Halbach setup with a field sweep rate of 0.5 T/s and pulsed fields up to 2 T and 14 T providing rates of 140 T/s and 1000 T/s, respectively. The experimental setup with pulsed fields had an uncertainty of the absolute temperature determination, however, the relative change in temperature is reliable. The values of the adiabatic temperature change were compared with the Halbach setup, and it is easy to observe a saturation of the effect that should occur irrespective of the field source. An example of 2 T field measurements in the pulsed field and in the Halbach setup is shown in Fig. 3.14.

The metamagnetic transition accompanied by the reduction of the sample temperature occurs much faster in the pulsed field. Furthermore, there is no hysteresis effect, since after cooling by 6 K, the temperature retreats to the starting point, making a fully reversible curve. However, the $\Delta T(H)$ dependence measured in the Halbach setup, shows the influence of hysteresis: after the demagnetization process, the sample is 1.6 K cooler than at the beginning of the cycle. The second field application affects the sample significantly as well, and the value of ΔT_{ad} under cycling at this temperature is 4.6 K. After the

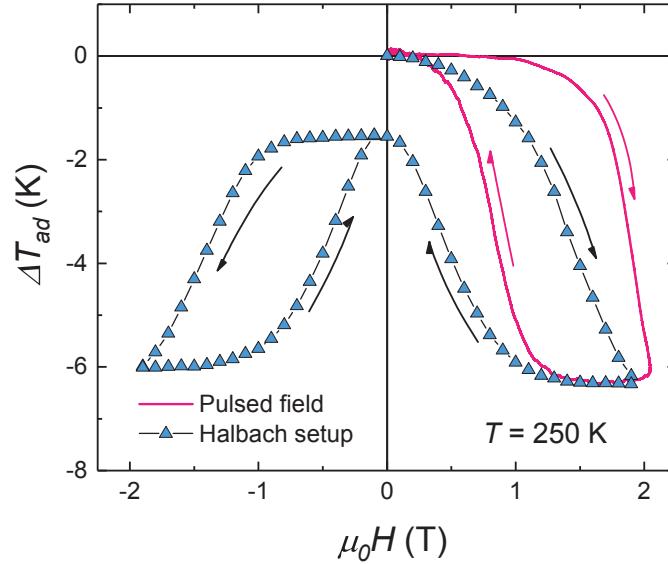


Figure 3.14 Field dependence of the adiabatic temperature change for the Ni-doped FeRh alloy measured in pulsed magnetic fields of 2 T (solid line) and in the Halbach setup (triangles). The sweeping rate of the pulsed magnetic field is almost 300 times higher.

second field application there is no further reduction of the effect, since the temperature did not reduce any further than 1.6 K compared to the initial temperature. The values of ΔT_{ad} from the first branch obtained at different temperatures produce a temperature dependence of the adiabatic temperature change in the discontinuous mode that helps to estimate the fundamental properties of the material. A more practical dependence under cyclic conditions is constructed using the values from the second field run, helping to estimate the behavior of the material in a cooling cycle close to the operational conditions of a cooling device.

The direct measurements in fields up to 14 T were carried out at 4 selected temperatures (the same temperatures at which the magnetization curves in pulsed fields up to 14 T were measured). The results of the measurements are shown in Fig. 3.15a: the MCE effect reaches saturation and does not increase further with field. The value of the adiabatic temperature change increases with temperature towards T_{tr} at zero field. The temperature after the measurement is higher than in the beginning, the effect is increasing towards lower temperatures. The mechanism of this irreversible heating is not understood, although technically it can be considered as hysteresis losses as in permanent magnets. This is not typical for magnetocaloric systems, for example, the direct measurements carried out in $\text{La}(\text{Fe,Si,Co})_{13}$ [183] or Ni-Mn-In-(Co) [185] do not show this effect. However, it has occurred in Mn_3GaC [186] that also experiences a magnetostructural AF–FM transition.

The irreversible heating in the end of the measurement was compared to the hystere-

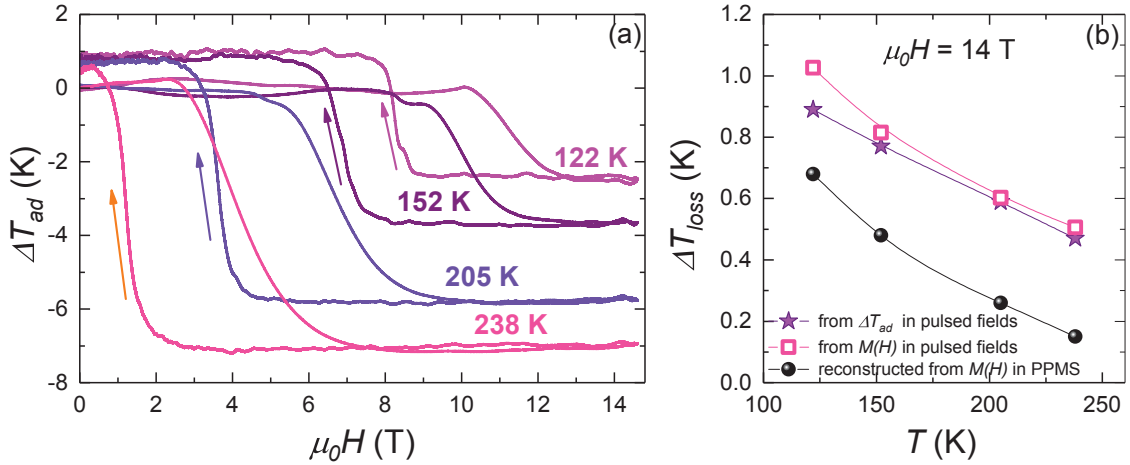


Figure 3.15 (a) Field dependence of ΔT_{ad} obtained by the direct measurements in pulsed field of 14 T (b) Estimation of the expected losses from adiabatic loops compared to the final overheating observed during direct measurements.

sis losses that could be expected based on the area of the hysteresis loop and the heat capacity value at particular temperature. Surprisingly, these values have a very good agreement (squares and stars in Fig. 3.15b). Since this heating takes place exclusively in pulsed fields, in order to estimate the effect of the sweep rate, quasiadiabatic curves were constructed from the isothermal measurements (see Fig. 3.11), imitating "slow" adiabatic curves. The assumption was that the transition during the field increase occurs at the set temperature of the measurement at particular temperature, while the transition during the field decrease should be shifted using a respective measured ΔT_{ad} value shown in Fig. 3.15a, i.e. using an isothermal curve at a lower temperature for the reverse transition. That way it was possible to estimate the hysteresis losses in a "slow" adiabatic process. The values corresponding to the losses calculated for this slow quasi-adiabatic process (black circles) trace the plot with the values calculated from the pulsed field magnetization data (fast adiabatic process), only with a parallel shift. Possibly, the difference (heating) can be related to some inductive microcurrents that are a feature exclusively of an order-order type material, also connected to the domain wall motion. The speed of the transition is the key: during slower transitions such currents will be neglectable. Also comparing the field values, a 14 T pulse would produce 7 times more heat than a 2 T pulse. The return of the temperature to the initial value as shown in Fig. 3.14 and the coincidence of the overheating and the calculated hysteresis losses can be an indication that in the pulsed field the interaction with the lattice changes its behaviour.

In Fig. 3.16 all temperature dependences for the Ni-doped sample can be found, for 14 T and 2 T magnetic field. The values obtained from the $S - T$ diagram are shown as dotted lines, stars represent the pulsed field data, and triangles the Halbach setup. In

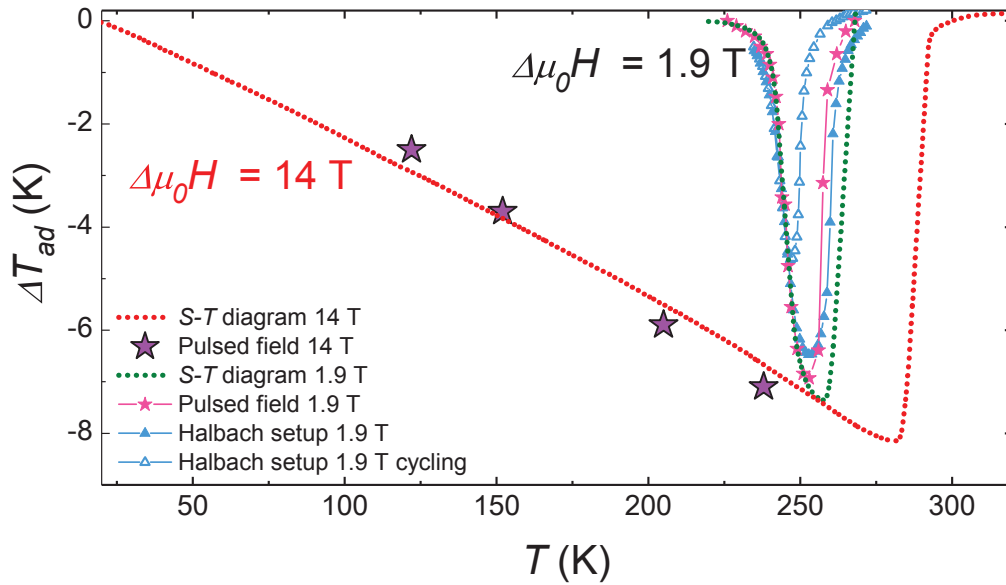


Figure 3.16 Temperature dependence of the adiabatic temperature change for 14 T field measured directly in pulsed magnetic fields (stars) up to 14 T compared with the values obtained from $S - T$ diagrams in 1.9 T and 14 T (dotted lines) as well as from the direct measurements in Halbach setup in 1.9 T (triangles, open symbols stand for the cyclic conditions)

principle, there is a good agreement between different methods. As in the case of the binary compound, there is a certain splitting of the continuous and discontinuous $\Delta T_{ad}(T)$ curves towards higher temperatures after passing the maximal value. The maximal value $\Delta T_{ad} = 7.1$ K was retrieved in both 14 T and 2 T pulsed fields at approximately the same temperature. This is very close to the estimation of the maximal adiabatic temperature change using the indirectly evaluated entropy change. The ΔT_{ad} value under cyclic conditions is quite high, and even experiences less reduction compared to the binary sample (35 % vs. 30 %).

3.3 Conclusions

Using indirect methods for the estimation of the MCE, the maximal possible adiabatic temperature change in $\text{Fe}_{49}\text{Rh}_{51}$ has been evaluated to be in the range of 10.5-13 K. The reported results fall into this region or are below it. The maximal ΔT_{ad} obtained in this work through a quasi-dynamic method of direct measurement is 9.2 K in a 1.9 T magnetic field; the discrepancy between the values obtained by different methods can be caused by the transition temperature distribution in grains of the real sample, which lowers the possible MCE.

Direct measurements of ΔT_{ad} and a conventional determination of ΔS from magnetic measurements showed that even under cyclic conditions, although ΔT_{ad} in FeRh is reduced to 6.2 K, it is only 30 % lower than the initial value, and 15 % higher than in Gd in

Conclusions

similar magnetic fields. Direct measurements in FeRh substituted by Ni revealed ΔT_{ad} of 7.1 K in the discontinuous mode and 4 K under cycling. The direct measurements under the first field application have been carried out in two magnetic field sources with varying sweep rate: the Halbach setup (~ 0.5 T/s) and a pulsed-field magnet (~ 140 T/s). The obtained values agree well, but there is a clear difference depending on the field rate: how fast the value is reached and to which value the temperature returns after the field removal. During the pulsed field measurements, a peculiar behavior of the adiabatic temperature change has been observed: having reached the value of 6 K after the first field application, the effect was completely reversed compared to the measurement in the Halbach setup. The origin of this can be in the interaction between the magnetic and lattice subsystems.

At temperatures below 10 K, an avalanche-like behavior of the field-induced metamagnetic transition in the Ni-doped FeRh has been discovered. The nature of it is not completely clear. The reported data on the low-temperature jumps of magnetization in different materials suggest further investigation of this phenomenon: the thermal instabilities may depend on cooling conditions, as is seen from a measurement at the same low temperature value using both liquid and gaseous helium environment [178]. Of interest could be relaxation measurements, studies of the field-rate effect [176–178] and direct detection of thermal instabilities [179].

CHAPTER 4

EFFECT OF MICROSTRUCTURE ON THE PHASE TRANSITION

This chapter contains results of an investigation of the structure and microstructure of FeRh-based alloys in relation to their magnetic properties. The observed magnetic and microstructural peculiarities are shown to depend on the parameters of a heat treatment, as well as on a doping element. An extended study of the heat treatment effect has been done on the binary and Ni-doped FeRh alloys, while the microstructure of the FeRh alloys doped with other d-metals (Re, Cr, Ru, Pt, Pd) is examined briefly.

4.1 Effect of annealing on magnetic properties of Fe₄₈Rh₅₂

4.1.1 Shift of magnetostructural transition after heat treatment

The phase diagram of FeRh in the high temperature region is defined only roughly. The annealing temperature for obtaining the α' -phase in binary and substituted FeRh is usually chosen in the region 800°C–1200°C where according to the approximate lines of the phase diagram [44, 45], only the α' phase should be stable. Beside the unprecise character of the high temperature region, a revision of the low temperature part of the phase diagram has also been suggested, due to an unexpected appearance of the γ -phase in the temperature range where only the α' -phase should exist [46, 59, 101]. Given this uncertainty, it is not surprising that some of the data in the literature on the binary compound, all the more on the doped FeRh, appear to be contradictory. The idea of the discrepancies being due to the difference in heat treatment protocols was expressed for the first time in 1968 [62]. Evidenced from magnetic and magnetocaloric measurements, a comparison of quenched and furnace cooled samples revealed a higher transition temperature in the furnace cooled sample [4], whereas in another work, the situation is opposite and the quenched sample transforms at higher temperature [52].

The effect of annealing duration and temperature was investigated for binary FeRh annealed up to three weeks at 700°C and 800°C, which resulted in a significant variation

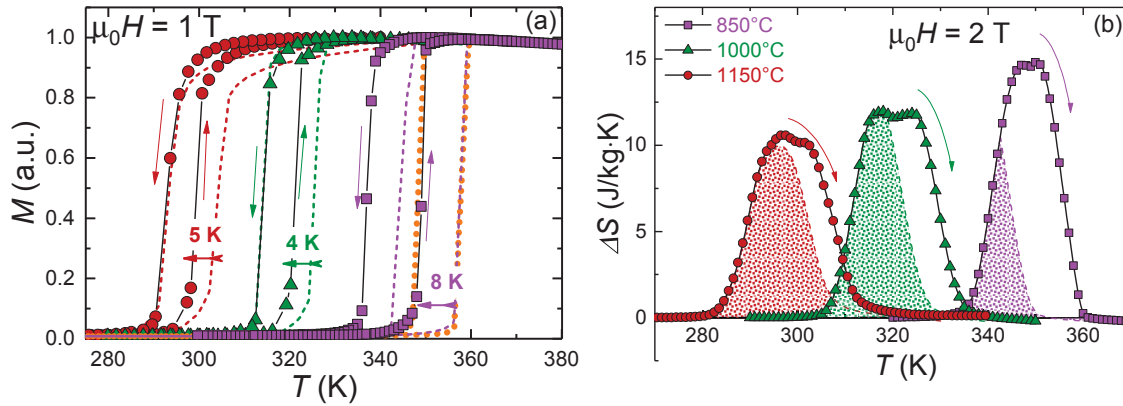


Figure 4.1 (a) Temperature dependence of magnetization of $\text{Fe}_{48}\text{Rh}_{52}$ heat treated at three different temperatures; the dashed lines of respective color are the measurements done during the first magnetization. Dotted orange line is after tempering (450 °C, 3 h) of the sample annealed at 850 °C. (b) Entropy change of $\text{Fe}_{48}\text{Rh}_{52}$ calculated from field-dependent $M(T)$ measurements. The filled area shows the region where the MCE is expected to be reversible.

of the transition temperature T_{tr} observed by means of resistivity measurements [46]; the sharpness of the transition was greatly affected as well. The proposed explanation of this behavior involved a redistribution of Rh in the magnetic α' -phase by diffusion, caused by the discovered growth of Rh-rich precipitates, unfortunately no experimental proof on the chemical composition was provided. These results indicate that the microstructure may play an important role affecting the magnetic properties. Therefore, the phase content and the chemical composition should be carefully examined, and the γ -phase should not be ignored for being paramagnetic, since it may have some mechanical effects interacting with the major phase.

With the purpose of clarifying how a heat treatment affects the magnetic state of FeRh alloys, a systematic investigation of the nominal composition $\text{Fe}_{48}\text{Rh}_{52}$ has been undertaken. The binary alloy of this composition according to the latest phase diagram should have the AF–FM transition temperature close to room temperature, and after a heat treatment near 1000 °C should be either in the region of a pure α' -phase or right on the border of the mixed ($\alpha' + \gamma$) region. From an as-cast ingot prepared by arc melting, three samples were cut out for annealing under the following conditions: 2 weeks at 850 °C, 1000 °C and 1150 °C, followed by water quenching. The annealing temperature (T_{ann}) was selected so as to cover the common annealing range for binary FeRh.

In order to observe the temperature and character of the magnetostructural transition, temperature dependent measurements of magnetization were performed. In Fig. 4.1 a strong effect of the annealing temperature T_{ann} on the transition can be seen. Measured on heating in a magnetic field of 1 T, the transition temperatures are: 349 K ($T_{ann} = 850^\circ\text{C}$); 321 K ($T_{ann} = 1000^\circ\text{C}$) and 300 K ($T_{ann} = 1150^\circ\text{C}$). That is, the higher T_{ann} ,

the lower the magnetostructural transition temperature. In other words, only due to the variation in the annealing temperature, in the samples from the same ingot the transition temperatures became distributed over an interval of 50 K. The transition looks somewhat sharper when the annealing temperature is the lowest (850°C). The hysteresis is affected as well, and reduces from 12 K to 6-7 K with increasing annealing temperature.

During magnetic measurements it was discovered that the magnetization curve at the first field application differs from the following measurements. For the next magnetization process, the transition is shifted by 4-8 K towards lower temperatures (the strongest effect is found for the 850°C-sample) where it stabilizes for all the following runs. In Fig. 4.1a the first magnetization curves are shown as dashed lines. This may be a result of some irreversible change within the sample during magnetization. Assuming that it could be related to strain accumulated in the samples during quenching or during the transition, which is known to be accompanied by 1 % volume change [51], a 3 hour tempering at 450°C followed by a furnace cooling of 1°C /min was done as a test for one of the samples (annealed at 850°C). After the tempering (dotted orange line in Fig. 4.1a), the transition occurs on heating exactly at the place of the initial curve. For some reason, the FM–AF transition now takes place at a higher temperature compared to the initial run, thus producing a smaller hysteresis.

The magnetic entropy change estimated by Maxwell relations from the temperature dependences of magnetization measured in constant magnetic fields up to 2 T is shown in Fig. 4.1b. The maximal value of the entropy change rises with the transition temperature of the samples, the filled area shows the region where reversibility of the MCE should be expected (as proposed in [114]). This region is related to the thermal hysteresis width, and as the highest hysteresis value is observed for 850°C annealing, it produces the lowest reversible area.

4.1.2 Microscopy, structural and elemental analysis

In order to understand what could be the reason of such an effect on the AF–FM transition after heat treatment at different temperatures, the structural and microstructural analysis of as-cast and heat treated FeRh samples was carried out. According to the XRD patterns (Fig. 4.2), the as-cast sample consists mostly of the fcc γ -phase, although the targeted α' -phase is detected as well. After annealing at temperatures 850°C–1150°C, the ordered α' -phase is dominant, but a small amount of the γ -phase is retained; the highest amount is found for $T_{ann} = 850^\circ\text{C}$ and almost no trace of it for $T_{ann} = 1150^\circ\text{C}$. The lattice parameters for both phases are given in Table 1. As can be seen, the α' -phase of all samples has the same lattice parameters, but the lattice parameter of the γ -phase reduces as the annealing temperature rises.

In Fig. 4.2 along with the XRD patterns, backscattered electron images of the as-cast

Table 1 Properties of FeRh samples annealed at different temperatures (T_{ann}): transition temperature (T_{tr}) in 1 T magnetic field on heating; chemical composition (from EDX, error ± 1 at. %); lattice parameter a and density, ρ of α' - and γ -phases (from XRD); degree of chemical order $S_{\alpha'}$ of the α' -phase (from XRD); volume fraction V_f of the γ -phase (from quantitative metallography).

T_{ann} [°C]	T_{tr} [K]	Phase	Fe [at. %]	Rh [at. %]	a [Å]	ρ [g/cm ³]	$S_{\alpha'}$	γ - V_f
as-cast	347	α'	49.0	51.0	2.989	9.95	0.95	~ 0.67
		γ	46.8	53.2	3.758	10.12		
850	349	α'	49.2	50.8	2.987	9.94	0.92	~ 0.08
		γ	33.3	66.7	3.768	10.83		
1000	321	α'	48.9	51.1	2.987	9.95	0.92	~ 0.12
		γ	35.9	64.1	3.766	10.70		
1150	300	α'	48.7	51.3	2.987	9.97	0.90	~ 0.15
		γ	38.7	61.3	3.760	10.58		

state and of samples annealed at given temperatures can be found. The as-cast state (Fig. 4.2a) exhibits a dendritic structure of two phases; the darker one is the ordered α' -phase and the brighter majority phase is the fcc γ -phase. The atomic composition of both phases is close to equiatomic, the lighter γ -dendrites exhibit a higher Rh content, but only 2 at. % more than the darker α' -phase (Table 1). The micrographs of the heat treated samples reveal a quite different microstructure (Fig. 4.2b,c,d) with bright globular regions of the γ -phase and large, darker grains of the α' -phase. It can be seen that, as the annealing temperature increases, both γ -phase and α' -phase grains coarsen. The distribution and shape of the inclusions change drastically. The γ -phase regions have equiaxed shape but different size for 850°C and 1150°C annealing temperatures, respectively, whereas at 850°C the γ -phase is more needle shaped and bears resemblance to a eutectoid reaction. Quantitative EDX measurements (Table 1) show that the mean Fe and Rh contents of the α' -phase are the same for all samples, within the limits of the experimental error (± 1 at. %), whereas the γ -phase composition differs noticeably.

The disordered γ -phase at such high temperature according to the phase diagram, if present (in the mixed region), should indeed contain more Rh than α' , so the variation of the lattice parameter is in accordance with the chemical composition: when the annealing temperature rises, the amount of Rh in the γ -phase decreases. Since Rh is bigger than Fe, so does the lattice parameter.

This microstructure is visible only after polishing. Otherwise, the surface layer after the annealing experiences recrystallization and seems to affect both XRD and microscopical images. As can be seen from Fig. 4.2, there may be no quantitative agreement of the

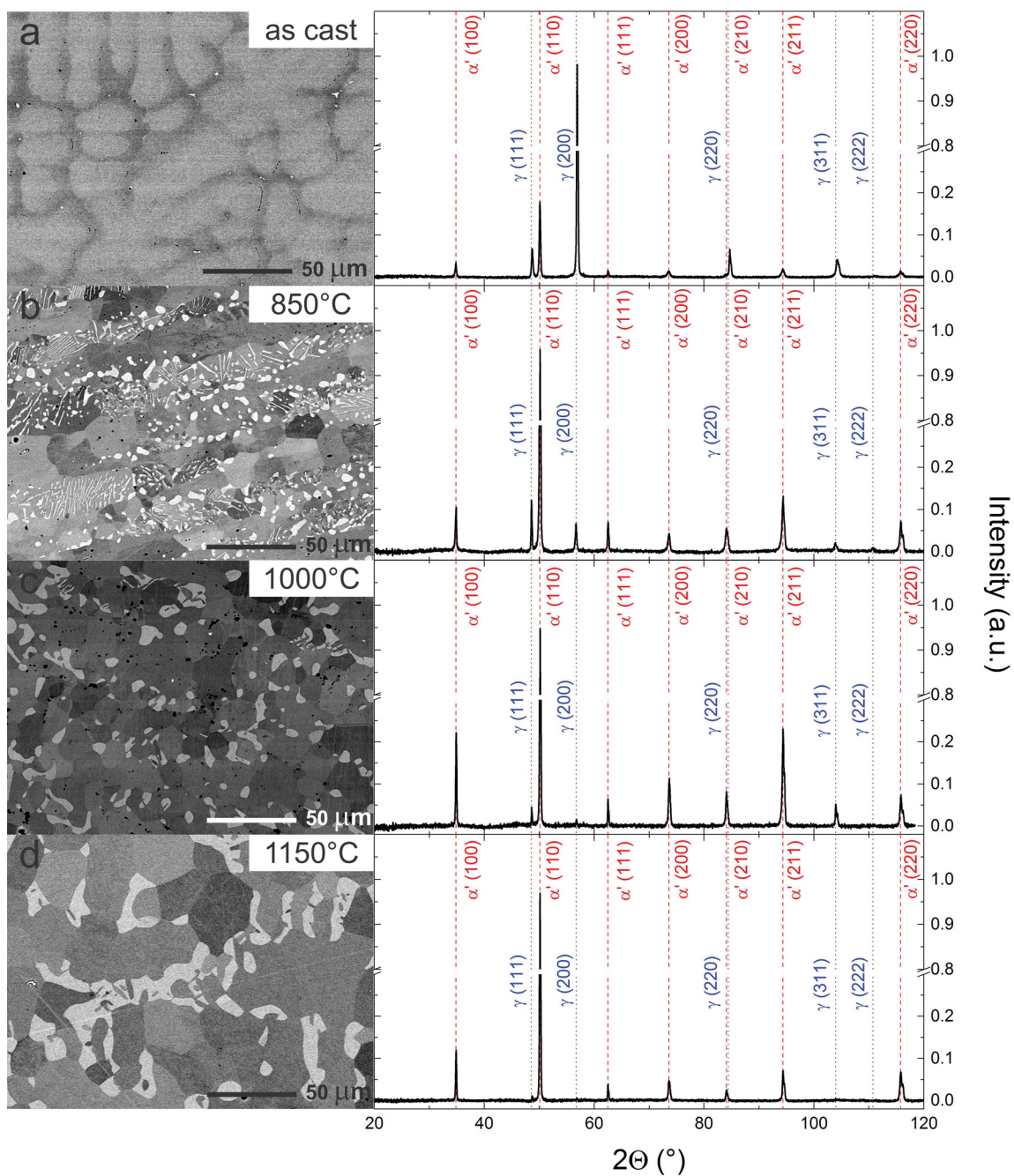


Figure 4.2 Backscattered electron images and X-ray diffraction patterns of the as-cast and heat treated FeRh samples (dark grains on the micrographs are α' -phase, the lighter grains fcc γ -phase).

XRD patterns with the electron images with regard to phase fractions. In particular, the sample annealed at 1150°C shows almost no γ -phase in the XRD, whereas from the SEM image it is clear that the sample contains a considerable amount of a Rh-rich phase that can only be the γ -phase. This may result in erroneous conclusions about the phase content when based only on the XRD data.

Regarding the volume fraction of the γ -phase implied from XRD and measured from SEM images, a significant discrepancy is noticeable. In the case of the 1150°C-sample, the reason why the (111) γ peak in the XRD is the smallest and almost negligible can be due to a strong texturing after the directional cooling during solidification originating from the arc melter geometry (a hot liquid metal drop on a cold tray) and highest coarsening of both phases at the highest annealing temperature. Alternatively, an estimation of the γ volume fraction determined by the quantitative metallography approach reveals the opposite. Although the distribution of the minor phase in all samples slightly varies from the edge towards the center, there is a general tendency for the γ volume fraction to increase with the annealing temperature (see [Table 1](#) for values and the SEM images in [Fig. 4.2](#) for visualization).

Small variations away from complete B2 order and stoichiometry, or Fe atoms occupying a very small proportion of the Rh sublattice sites, have been shown to have a strong effect on the transition [73]. In order to estimate the degree of chemical ordering of the α' -phase, extra patterns with high resolution were obtained for the superlattice (100) and the fundamental (200) peaks. The degree of order can be estimated through determination of the ratio of the integrated intensities of the superlattice (100) and fundamental (200) reflexes of the α' -phase that relate as $S_{\alpha'} \sim \sqrt{I_{(100)}/I_{(200)}}$, $0 < S_{\alpha'} < 1$, where 1 is the perfectly ordered state and 0 means complete disorder. The appearance of texture should not affect the result in this method. The actual composition measured by EDX was used to simulate an ideal, i.e. perfectly ordered, XRD pattern as a reference, in order to account for the disorder caused by the deviation from the equiatomic composition. The degree of order of the α' -phase in all samples was found to be very high ([Table 1](#)), did not differ strongly with T_{ann} and also remained equally high even for the as-cast state. Therefore, it is unlikely to make it responsible for the strong shift of the AF–FM transition.

It is known that the AF–FM transition in FeRh alloys is strongly affected by smallest changes of the chemical composition, within the binary system or due to doping by other d-elements [65, 66, 68, 69]. However, according to the EDX analysis, in these samples the α' -phase has the same composition, which also correlates with the lattice parameters found from XRD. Although a slight trend of Rh enrichment towards annealing at higher temperatures can be observed, this difference (0.2-0.3 at. %) lies within the systematic error of the method (± 1 at. %). The expected shift of T_{tr} with increasing Rh content [75] should be in the opposite direction to the one observed in this experiment, so it

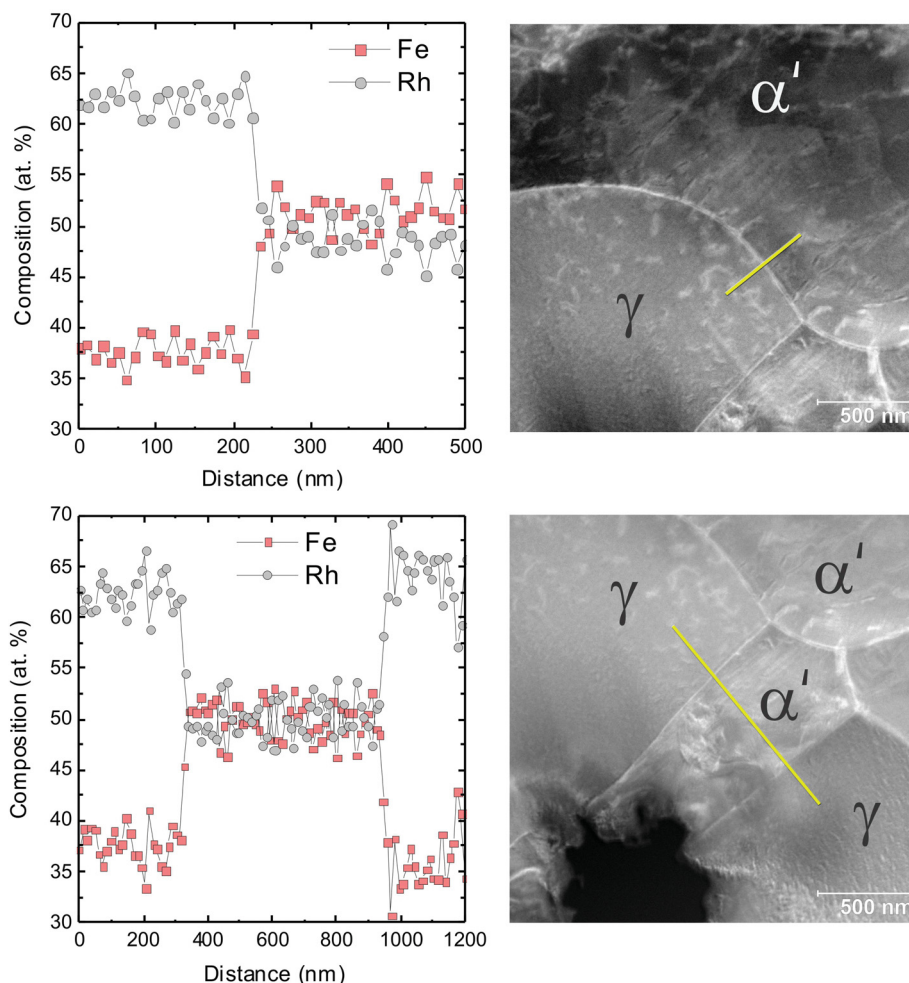


Figure 4.3 STEM dark field images of the FeRh sample annealed at 1000°C with the position of the EDX linescans marked with a yellow line and accompanying composition profiles for Fe and Rh.

is difficult to assume that the shift in the AF–FM transition can be explained by these small differences in the composition of the α' -phase. Even disregarding the systematic error and considering the difference in EDX data as sufficient, the drastic variation of the transition temperature over the 50 K range cannot be explained on the base of the latest phase diagram [44] where the temperature of the AF–FM transition changes as fast as 30 K/ 1 at. % Rh, whereas in this experiment the rate would be 100 K/ 1 at. % Rh.

Since the idea of a Rh gradient occurring in the α' -phase during the γ -phase growth [46] was not supported by experimental data, a TEM investigation of the FeRh sample annealed at 1000°C was carried out aiming to check the distribution of the elements in the grains of both phases*. The EDX linescans with accompanying dark field STEM images of the microstructure and the indication of the place where the linescan was done

*Carried out by Dr. T.G. Woodcock, IFW Dresden

The provision of the TEM facilities and support by Dr. B. Rellinghaus is deeply appreciated

are presented in Fig. 4.3. The interface appears to be very sharp, i.e. no gradient in the composition larger than the step size of the EDX linescans (10-12 nm) appears at the phase boundary, and over the length of the linescan from the phase boundary into the phases ($\sim 0.25 \mu\text{m}$) it was not possible to detect a gradient of atomic composition in the α' -phase or γ -phase. It is reasonable to believe that the system has reached thermal equilibrium during the annealing. Thus, the variation of the α' -phase composition both within the grain and the whole sample is negligible and averages to 51 at. % Rh.

4.1.3 Modeling of stress fields resulting from heterogeneous microstructure

The α' -phase of all three samples appears to be highly ordered, being of the same composition and lattice parameter (within the error). No composition gradient at the α'/γ -phase boundaries is observed. Therefore, none of these factors can explain why the transition temperature in the annealed samples varies so much. Still, there are obvious differences in the microstructure of the samples. Considering that the density, the structure and the thermal expansion of the γ - and α' -phase are quite different and the AF–FM transition itself is accompanied by a 1% volume expansion of the α' -phase, it seems reasonable to consider the idea of stress fields. Stress resulting from differential expansion of the two phases should occur regardless of the coherency of the boundaries and will depend on size, shape and distribution of the minor phase. It has been known that FeRh compounds react drastically to stress, for example, an applied hydrostatic pressure (compressive stress) stabilizes the AF state, raising T_{tr} and can even induce the AF state in an initially FM sample [62, 128]. Tensile stress caused by the substrate in thin films of FeRh lowers T_{tr} [125] or some part of the sample remains in the FM state [101, 137]. Evidence of extra phases in the bulk affecting the transition temperature was reported after annealing of Pd-doped FeRh [187]. In an early study of Rh-rich (> 55 at. %) alloys [60], a reduction of the magnetic moment and an increase of the transition temperature were reported. In the latter work the authors refer to the work of Zakharov [51] that expresses an idea that the variation in the transition temperature with composition and the larger thermal hysteresis at high Rh concentrations may be accounted to inhomogeneous strain in the α' -phase due to the presence of increasing amounts of γ -phase, which could delay the AF–FM transition.

In order to estimate the magnitude and the extent of possible stress fields resulting from the differential expansion of the two phases, 2D FEM simulations were carried out (see the details in the experimental methods description)*. Three different cases were considered: small and large circular γ grains to compare the size effect, and a needle-like γ grain for the shape effect. In each model, the γ grain is surrounded by

*Carried out by Dr. F. Bittner, IFW Dresden

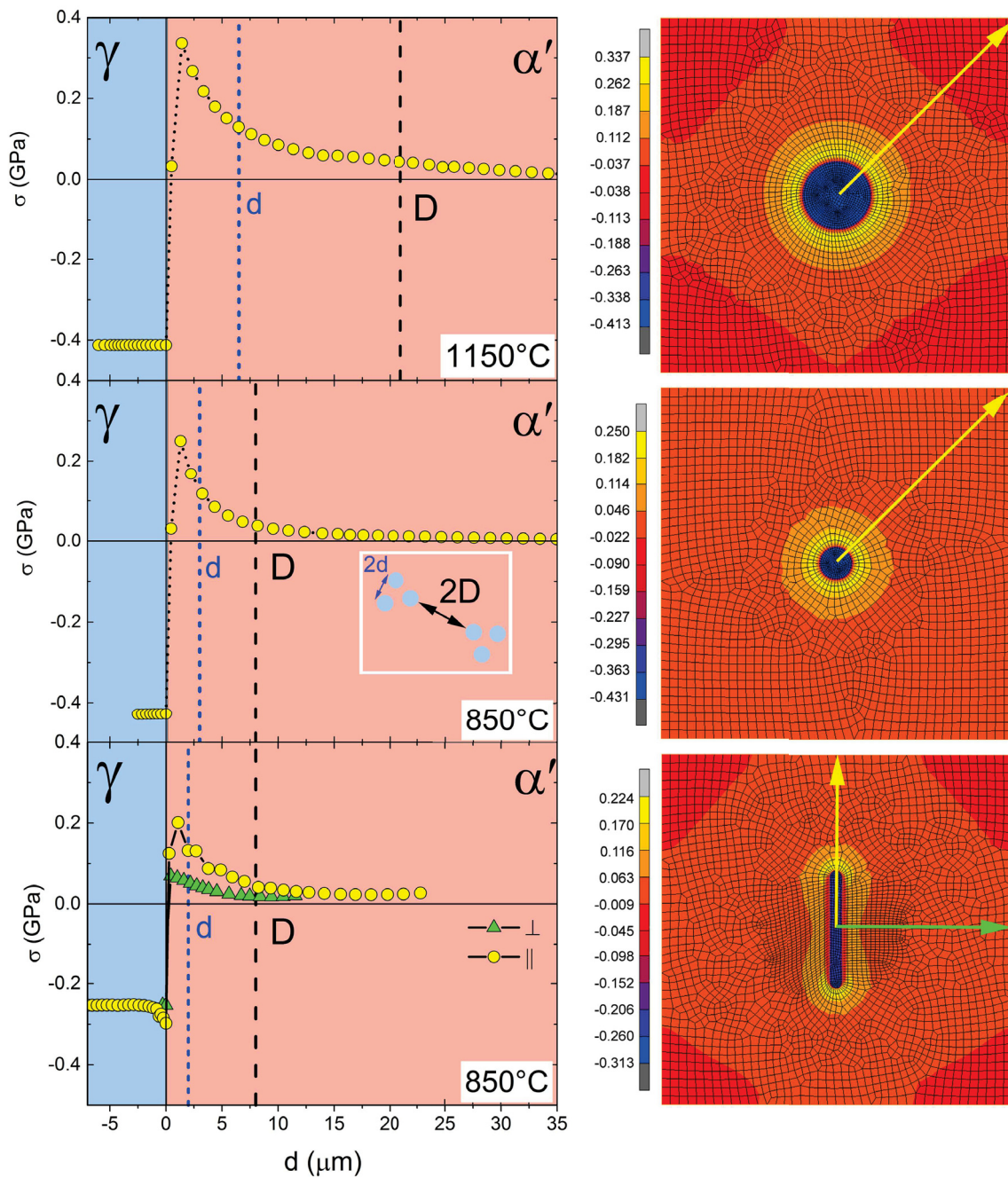


Figure 4.4 FEM simulations of the α' -matrix experiencing the AF-FM transition with 1% volume change in the presence of the secondary phase and the respective stress profiles.

the α' -phase. A length contraction of 0.33% of the α' -phase (equivalent to the 1 vol. % contraction on cooling the sample through the metamagnetic transition) was simulated. The resulting color maps in Fig. 4.4 represent the principal stress distribution in each model. The γ -grains are regarded to be under compression as the surrounding α' -matrix shrinks during the FM–AF transition (on cooling). Correspondingly, the α' -matrix will experience tensile stress that will depend on both shape and size of the inclusions.

The arrows on the color maps show the path along which the stress profiles were generated. In order to show the extent of the stress fields in the observed microstructures, the stress profiles are scaled to the average size of the γ grains, estimated from the SEM images: Fig. 4.2b (small circular and needle-like grains) and Fig. 4.2d (large circular grains). Due to the symmetry, two stress profiles have been made for the needle-like case: parallel and perpendicular to the needle axis. The diameters of the small and large circular grains were taken as 5 μm and 12 μm respectively, and the length and width of the needle-like grain were 15 μm and 1 μm , respectively. Although the absolute values of the stress must be taken as an estimate, the profiles (Fig. 4.4, left) clearly show that, as expected, the size and shape of the γ grains have an influence on the magnitude and extent of the surrounding stress field.

The γ grains are not homogeneously distributed within the microstructure (Fig. 4.2 b-d). As interactions between the stress fields of neighboring γ grains may occur, the characteristic separation distance between the minor phase grains is of interest. Here, two characteristic separation distances representing the typical shortest (2d) and longest separations (2D) of the γ grains have been defined in the schematic (see the inset on the stress profile in Fig. 4.4). The characteristic separation radii (i.e. d and D) are plotted on the stress profiles. The results show that for all the characteristic separations of the γ grains observed here, at least some interaction of the surrounding stress fields would be expected, which may result in higher stresses in the α' -phase. Although the magnitude of the stresses simulated here must be regarded as estimates, these values are comparable to the hydrostatic pressures which are known to shift T_{tr} at the rate of 60-70 K/GPa [128].

This information should be relevant not only for the Rh-rich FeRh compounds from the mixed ($\alpha' + \gamma$) region of the phase diagram but also for the equiatomic composition, since there were several indications [46, 59, 101] that the fcc precipitation was discovered in the FeRh alloys with less than 51 at. % Rh. A more detailed investigation of the phase formation in FeRh alloys could be of great significance, for example, an experimental observation of the stress fields.

4.2 Thermal history effects in Ni-doped FeRh

4.2.1 Suppression of magnetostructural transition after heat treatment

Doping of the binary compound FeRh by Ni, Co, Pd or Au lowers the magnetostructural transition temperature [9, 68, 69, 188]. One benefit of it is the availability of a comfortable experimental range for most conventional techniques. Another feature, in particular, for these alloys is that the effects associated with the first order transition become stronger: for example the hysteresis broadens [69, 188], the shift of the transition temperature with an applied hydrostatic pressure and/or a magnetic field increases [62, 69, 76, 129]. Therefore, it was of interest to carry out the same heat treatment experiment with such alloys, as in the previous section. A ternary alloy $(\text{Fe}_{0.965}\text{Ni}_{0.035})_{49}\text{Rh}_{52}$ was selected because this composition has the lowest AF–FM temperature among Ni-substituted alloys [69]; upon a further increase of the Ni content, only the FM state will exist. Therefore, this composition is on the border between the AF and FM states, and even small changes may result in drastic effects.

In the ternary Ni-doped FeRh, annealing at the temperatures of 850°C–1150°C also resulted in the AF–FM transition occurring at different temperatures (Fig. 4.5). Moreover, the sample annealed at 1000°C is ferromagnetic in the whole temperature range, that is the AF–FM transition was completely suppressed. This presence of the FM state does not allow to reveal a clear trend relating the transition temperature to the annealing temperature (the binary alloys had a clear linear trend). Most likely, several mechanisms might be responsible for this effect. As in the binary case, the first magnetization curve differs from the following runs: the transition temperature shifts towards lower values, and the largest shift (12 K) occurs also in the sample with the lowest annealing temper-

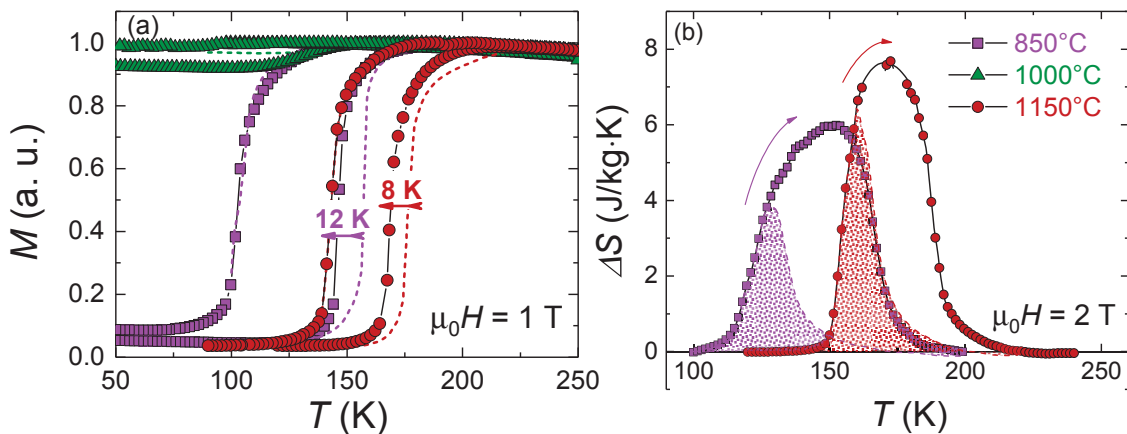


Figure 4.5 (a) Temperature dependences of magnetization and (b) magnetic entropy change in 2 T magnetic field of Ni-substituted FeRh. The samples were heat treated at three selected temperatures for 2 weeks followed by quenching. The filled area corresponds to the region where the MCE is expected to be reversible. The dashed lines show the first magnetization run.

ature (850°C). The magnetic entropy change is shown in Fig. 4.5b. The filled area shows the reversible region for the MCE, which is quite broad despite the large hysteresis. Both ΔS curves show lower maximal values compared to the binary FeRh, which is somewhat typical because the value of ΔS often tends to show a linear increase as the transition temperature rises [124].

The situation with Ni-doped alloys turned out to be more complex than the linear shift in the binary alloys. Therefore, additional samples of the same nominal composition ($\text{Fe}_{0.965}\text{Ni}_{0.035}$)₄₉Rh₅₂ were prepared in order to observe what happens under conditions of varying not only the annealing temperature, but also the cooling rate and the annealing time. Another point was to check the reproducibility of this strange suppression of the transition and, to observe annealing effects in an alloy that may be very sensitive even to minor changes in the thermal history. One sample was annealed for 2 weeks at 850°C and, instead of quenching, furnace cooled with a rate of 1°/min. Two more samples were annealed at 1000°C for only 3 days, and a cooling rate of 1°/min was chosen for one and quenching for the other sample. Then, a detailed structural and microstructural comparative study of all 6 samples was undertaken.

4.2.2 Microscopy, structural and elemental analysis

The room temperature XRD patterns are shown in Fig. 4.6 with the corresponding backscattered electron images. The lattice parameters (Table 2) are larger than for the binary FeRh: since the Ni-doped samples are all in the FM state at room temperature, the unit cell has already experienced a 1% expansion. In order to compare this Ni-doped FeRh with the parental binary compound properly and to observe the influence of the doping element, it would be necessary to have a low temperature XRD in the AF state. As in the previous section, the lattice parameter of the α' -phase has the same value for all heat treated samples, while the lattice parameter of the γ -phase differs but does not show the linear behavior, as in the binary case. The XRD patterns mismatch the SEM evidence of the minor phase fraction, probably for the same reasons of texturing and coarsening of grains. A quantitative analysis from XRD was not carried out due to the small size, random cut and texturing of the bulk samples. The degree of order determined as described in Section 4.1.2 is quite high in all cases, however, if to compare the samples annealed at the same temperature of 1000°C for 14 days and 3 days, it can be seen that the shorter annealing resulted in a somewhat lower degree of order (Table 2).

The microstructure shows the same tendency of coarsening towards higher annealing temperature, but the fcc phase looks more round and does not show traces of the eutectoid reaction, as it was the case for the 850°C binary FeRh (Fig. 4.2b). The ratio of the α'/γ phases in the as-cast state is different: the binary alloy had a larger amount of the high temperature γ -phase retained. Quantitative metallography reveals that the

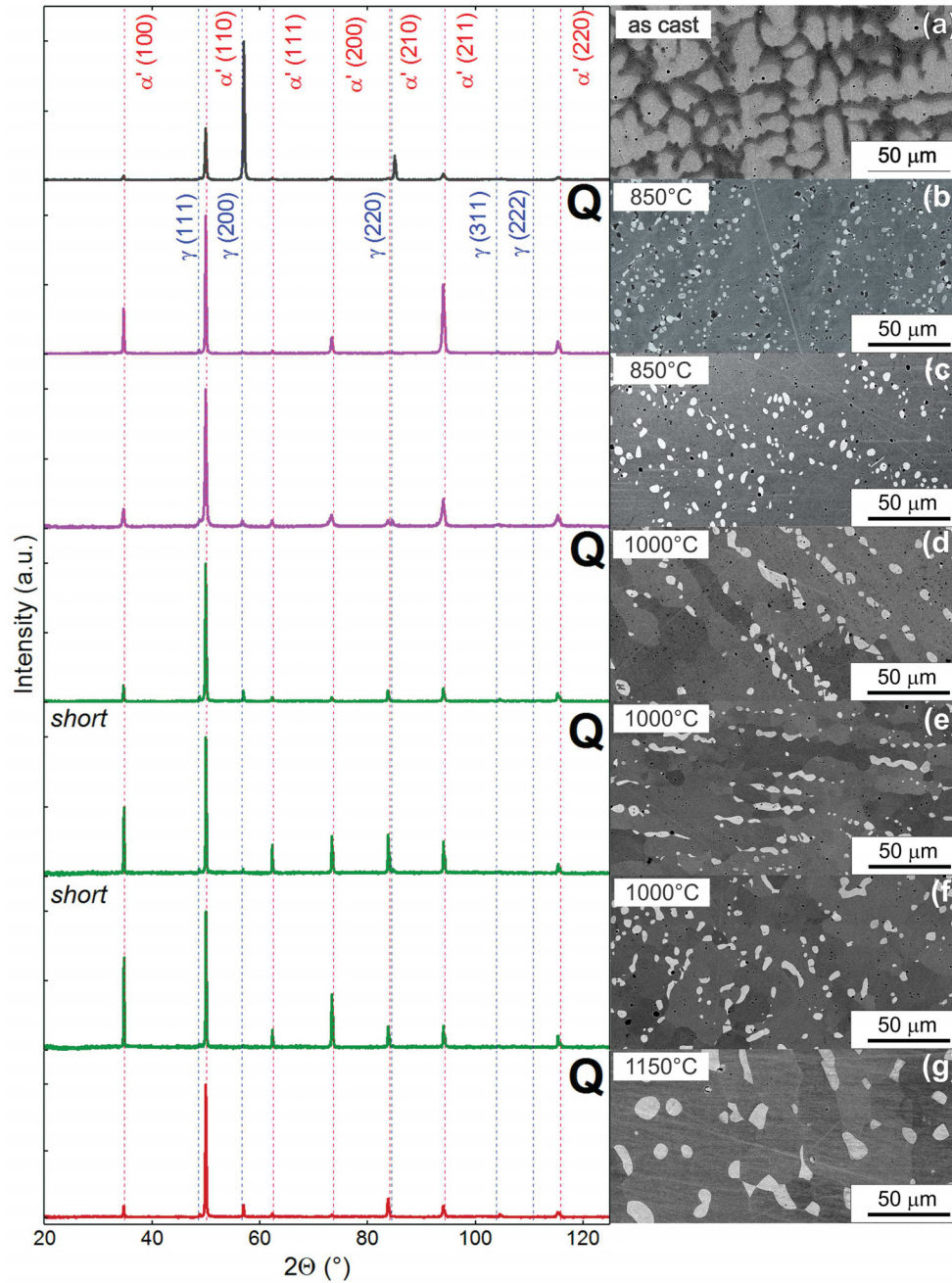


Figure 4.6 Room temperature X-ray diffraction patterns and SEM backscattered images of the as-cast and heat treated Ni-doped FeRh samples. The samples that were quenched are marked as Q. The samples annealed for 3 days are marked "short", in all other cases the annealing time was 14 days.

volume fraction of the minor γ -phase in the heat treated samples increases from 0.06 to 0.10 through annealing temperatures between 850°C and 1150°C and seems to be defined only by the annealing temperature without an influence of the cooling rate or the duration of annealing (see [Table 2](#)). This is the first attempt to define a distinguishable trend of the minor phase amount. However, it is possible that the volume fraction

determination at this stage is somewhat rough and can be done more precisely in the future: for example, covering a higher area of the sample (in this work about 10 %) or improving the image processing procedure.

The EDX results (Table 2) show that the Ni amount in the γ -phase is two times higher than in the α' -phase for all samples. This indicates that the actual amount of Ni in the magnetic matrix (α') is different from the one implied from the magnetic phase diagram [69]. It can be expected that the general trend of reduction of the transition temperature with increase of Ni-substitution may still apply, but probably with a lower actual Ni percent. However, it can be also possible that the excess of Ni is redistributed only towards the disordered γ -phase, allowing the same amount of Ni for the main α' -phase. In the present experiment, very small variations of the composition beyond the limits of the systematic error cannot be observed. Within the error, the composition of α' -phase appears to be exactly the same for all heat treated samples. Redistribution of the excess elements within the minor γ -phase seems to be regulated by an interplay of the growing volume fraction of the minor phase and its compositional change at different annealing temperatures. The disordered γ -phase exists in the whole compositional range and is not as demanding to the change in composition as the ordered α' -phase.

Since all the Ni-doped samples are FM at room temperature due to the low transition temperature or the absence of transition, it was possible to see a good magnetic contrast during MFM measurements (Fig. 4.7)*. Two different magnetic contrasts can be observed: small round non-magnetic grains of the minor γ -phase (the stripes are artefacts of the scanning process) and branched domain patterns of the major α' -phase. The α' -phase has the crystallographic cubic CsCl symmetry, so similar to α -Fe domain patterns should be expected. However, the observed domains are more cobalt-like, with a weak uniaxial anisotropy [189]. Sometimes distortions are observed around the non-magnetic inclusions, most prominent in Fig. 4.7c. These distortions can be related to the change of the magnetic matrix thickness in the out-of-plane dimension around the γ -grains.

It is certain that the type of the observed domains is not caused by the stress from the polishing procedure. However, the presence of a surface itself may play a role in the domain relaxation. Otherwise, it is not clear what would be the reason for this weak anisotropy of cubic FeRh-based alloys. It may be also attributed to the stress fields appearing during cooling of the two-phase sample from high annealing temperatures or to distortions caused by the presence of other elements (like Ni) in the lattice. This idea can be supported considering the (300) reflex of the magnetic α' -phase (see Table 2) that is at high angles and therefore can reveal tetragonal distortions by splitting of the peak. The presence of tetragonal distortions is only a hypothesis: to investigate this question further and detect small changes in the length of the unit cell sides, a complex

*Carried out by Katja Berger, IFW Dresden

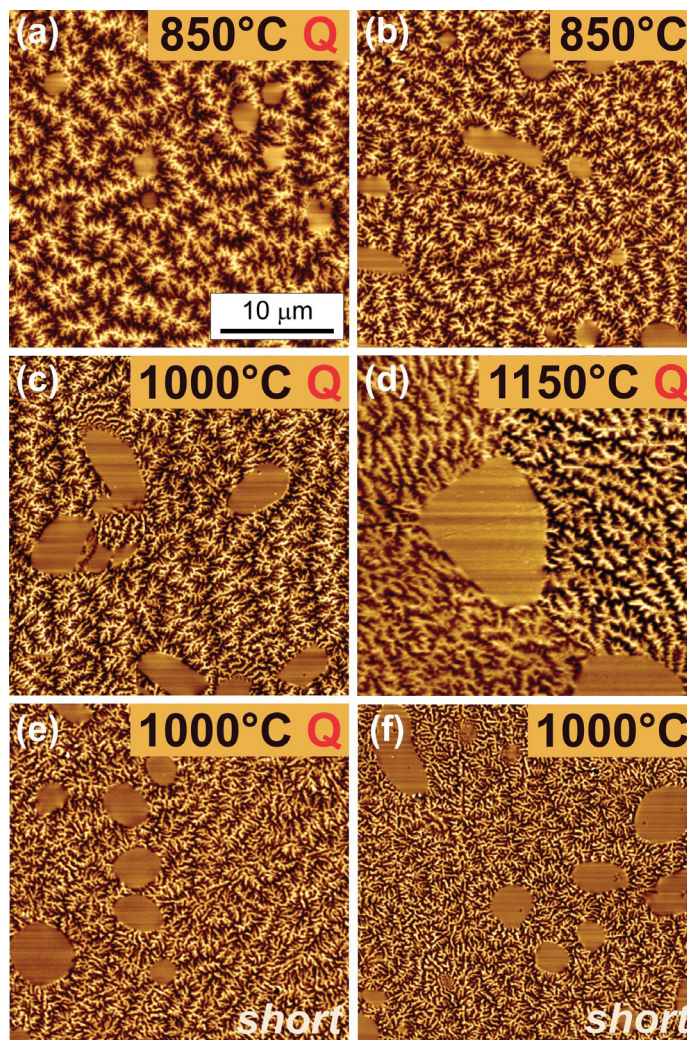


Figure 4.7 Room temperature magnetic force microscopy of heat treated (Fe,Ni)Rh: The samples that were quenched are marked by Q. The samples annealed for 3 days are marked "short", in all other cases the annealing time was 14 days.

experiment using particular reflections would have to be done [52].

The presented MFM images in Fig. 4.7 show a noticeable difference in the size of the domains. The size of the domains can be informative: the smaller the domains, the higher should be the stress. The characteristic domain size was estimated using an autocorrelation function at FWHM* and is given for all samples in Table 2. For example, comparing (a) and (b), the two samples annealed at 850°C for the same time, with a difference in the cooling rate only — the domain pattern looks similar in terms of shape, but scales down in the slowly cooled sample. The same can be observed for (e) and (f).

*Carried out by Dr. A. Volegov, Ural Federal University

Table 2 Properties of $(\text{Fe}_{0.965}\text{Ni}_{0.035})_{49}\text{Rh}_{52}$ samples annealed at different temperatures T_{ann} ; transition temperature T_{tr} in a 1 T field on heating (first run value in the brackets); annealing time; cooling rate; chemical composition (from EDX, error ± 1 at. %); lattice parameter a ; volume fraction V_f of the γ -phase (from quantitative metallography); characteristic domain size δ imaged by MFM; degree of chemical order $S_{\alpha'}$ of the α' -phase (from XRD) and shape of the α' -(300) peak.

T_{ann} [°C]	T_{tr} [K]	Time [days]	Cooling	Phase	Composition [at. %]			a [Å]	γ - V_f	δ [nm]	$S_{\alpha'}$	α' -(300)
					Fe	Rh	Ni					
as-cast	—	—	Quench	α'	49.0	48.8	2.2	2.994	0.50	—	—	—
850	146	14	Quench	α'	48.0	50.4	1.6	2.995	0.06	629	0.93	
	(158)			γ	33.4	64.2	2.4	3.753				
850	146	14	1°/min	α'	47.5	50.9	1.6	2.995	0.06	374	1.01	
	(164)			γ	33.2	64.4	2.4	3.752				
1000	—	14	Quench	α'	47.6	50.9	1.5	2.995	0.08	320	0.96	
	(—)			γ	35.3	61.8	2.8	3.763				
1000	—	3	Quench	α'	47.2	51.3	1.5	2.995	0.08	276	0.84	
	(—)			γ	34.8	62.4	2.8	3.763				
1000	122	3	1°/min	α'	47.0	51.5	1.5	2.995	0.08	216	0.79	
	(—)			γ	35.0	62.3	2.7	3.758				
1150	168	14	Quench	α'	47.6	50.9	1.5	2.995	0.10	506	0.87	
	(176)			γ	38.6	58.5	2.8	3.761				

4.2.3 Effects of hydrostatic pressure, tempering and thermal shock

As the AF–FM transition may depend on the mechanical interaction of the two phases, it is of interest to investigate how samples with different microstructure (for example, grain size) will behave under an application of hydrostatic pressure, a stress recovery annealing at lower temperature or a rapid cycling over the transition region.

For the experiments with hydrostatic pressure two samples were selected: heat treated at 850°C and 1150°C for 14 days followed by quenching (Fig. 4.6 b and g). These samples have a different grain size as well as a different volume fraction of the minor phase. The transition temperature is higher for the sample annealed at 1150°C.

The temperature dependences of the magnetization for 850°C and 1150°C heat treated samples at different pressures* are shown in Fig. 4.8 (a) and (b), respectively. The applied pressure is of the same range as the stress fields obtained by modeling (4.1.3), and results in a comparable shift of the transition temperature as the one detected after different annealing temperatures of FeRh — which may serve as an indirect proof of the stress field effects due to the heterogeneous microstructure. The transition temperature shift under pressure comprised 19 K/kbar and 16 K/kbar for 850°C and 1150°C respectively. Not only the transition temperature is affected but also the hysteresis width: the reduction of the hysteresis can be observed in Fig. 4.8 (c). This reduction appears to be more intense in the sample heat treated at 850°C. One can recall that according to the FEM simulations, the stress fields should be smaller when the microstructure is finer (after 850°C annealing).

After the pressure removal, the reverse FM–AF transition shifted to lower temperature, however the AF–FM transition remained unaffected (shown in Fig. 4.9 and Fig. 4.10) — this can be indicative of some irreversible changes occurring in the microstructure during the simultaneous pressure and field application.

Investigation of the AF–FM behavior under different thermal influences consisted of a stress recovery at a moderate temperature or a rapid cycling through the transition. The stress recovery has been done by a heat treatment for 3 hours at 450°C followed by furnace cooling with a rate of 1 K/min. Thermal shock treatment was done by immersing samples subsequently in a liquid nitrogen bath and a water bath at room temperature. Considering the transition temperature region, this procedure allows a rapid cycling through the transition. Overall, the following protocol was employed for all 6 samples: heat treatment — first magnetization — second magnetization — [pressure application and release – only for 2 samples] — stress free annealing — thermal shock. The results are summarized in Fig. 4.9 (samples heat treated for 2 weeks at 850°C) and Fig. 4.10 (one sample heat treated at 1150°C and two samples annealed at 1000°C for a short time).

*Carried out in collaboration with Dr. K. Nenkov, IFW Dresden

As can be seen from Fig. 4.9, during the first run (dashed line) for both samples annealed at 850°C the AF–FM transition occurs at different temperatures: at 158 K for the quenched sample and at 164 K for the furnace cooled. However, at the next field application, both samples, surprisingly, have the same transition temperature of 146 K. An assumption that the slowly cooled sample should have lower stress compared to the rapid quenching process would even be in accordance with the results of the FEM simulations, if one recalls how the stress affects the transition. In the binary compound, the highest stress from the heterogeneous microstructure resulted in the lowest T_{tr} , and in this case the quenched sample has a T_{tr} lower by 8 K. In fact, it is possible that the stress fields originate from multiple sources and can be of a long- and short-range, because already in the second run the samples shift from the original temperature and stabilize the transition at the same temperature of 146 K.

An experimental detection of strain requires a very fine polished surface free from a residual strain. In the case of FeRh, the material is rather soft and there is a presence of the secondary phase with higher density. The fcc phase tends to fall out during standard preparation procedures, leaving scratches, and the softness of the material in principle allows an easy deformation of the top layers, making it difficult to obtain the desired quality of the surface and limiting the techniques that can be used for the anal-

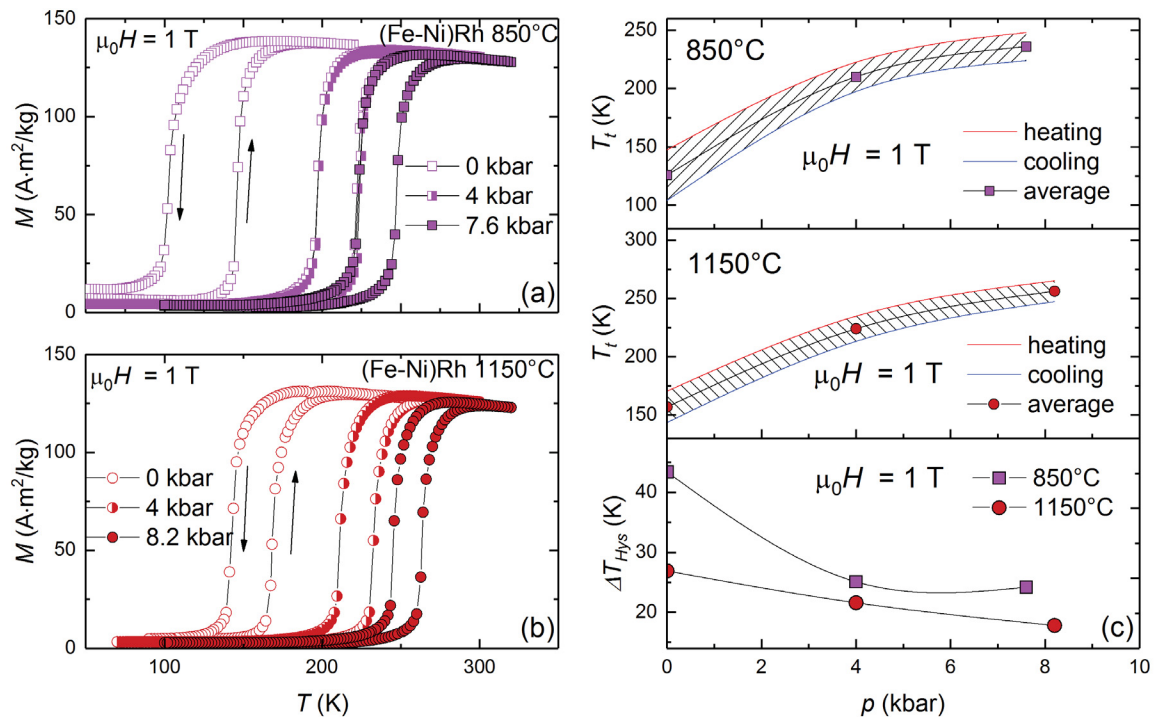


Figure 4.8 Temperature dependences of the magnetization under applied hydrostatic pressure up to 8.3 kbar for Ni-doped samples annealed for 2 weeks at (a) 850°C and (b) 1150°C; (c) pressure dependences of the transition temperature and the hysteresis.

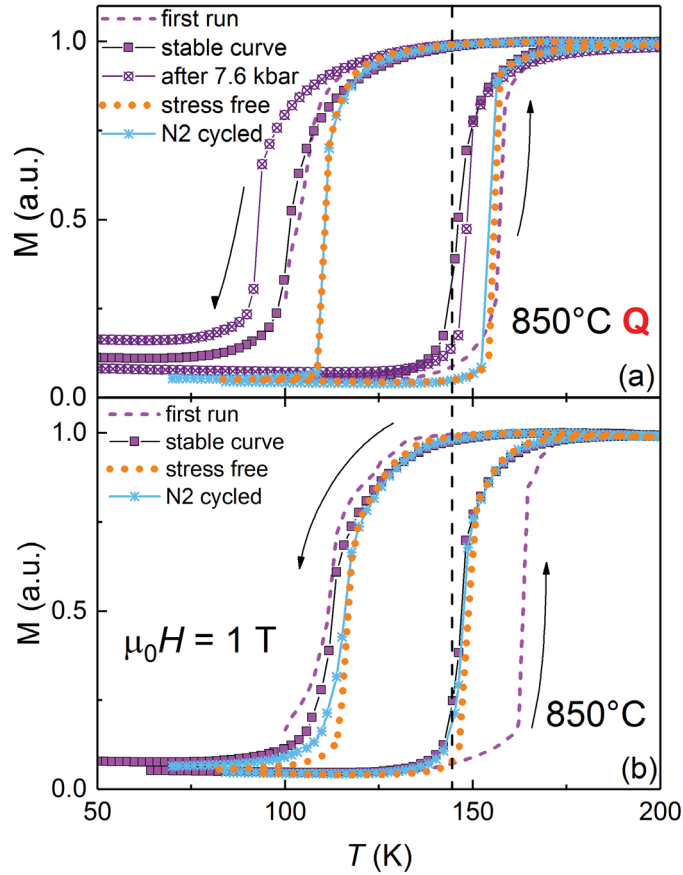


Figure 4.9 Evolution of the magnetostructural transition and hysteresis effect in two samples of $(\text{Fe}_{0.965}\text{Ni}_{0.035})_{49}\text{Rh}_{51}$ annealed at 850°C for 14 days with the only difference being the cooling rate: quenched (a) and furnace cooled (b). The quenched sample (a) has a magnetization dependence measured after the hydrostatic pressure application. The difference between the first and subsequent magnetization runs is shown for both samples, as well as the reaction to the stress free 3 h annealing at 450°C (orange dots) and liquid N_2 – room temperature cycling (30 cycles).

ysis. The FEM simulations in Section 4.1.3 have considered only the effects caused by the FM–AF transition – however, there is a similar effect that likely takes place due to the difference in the thermal expansion of the two phases while cooling down from high annealing temperatures, slowly or by quenching. The general consideration of the mechanical interaction should be similar, but then it is necessary to know the full temperature dependence of the thermal expansion coefficient of each phase from as high as 1000°C down to room temperature. Data from single-phase samples would be of interest, however the high temperature γ -phase does not exist at room temperature in this compositional range, and the magnetic CsCl phase often contains the overlooked retained γ -phase which makes the scarce available data questionable.

The pressure application has affected the transition as expected (Fig. 4.8), but seems

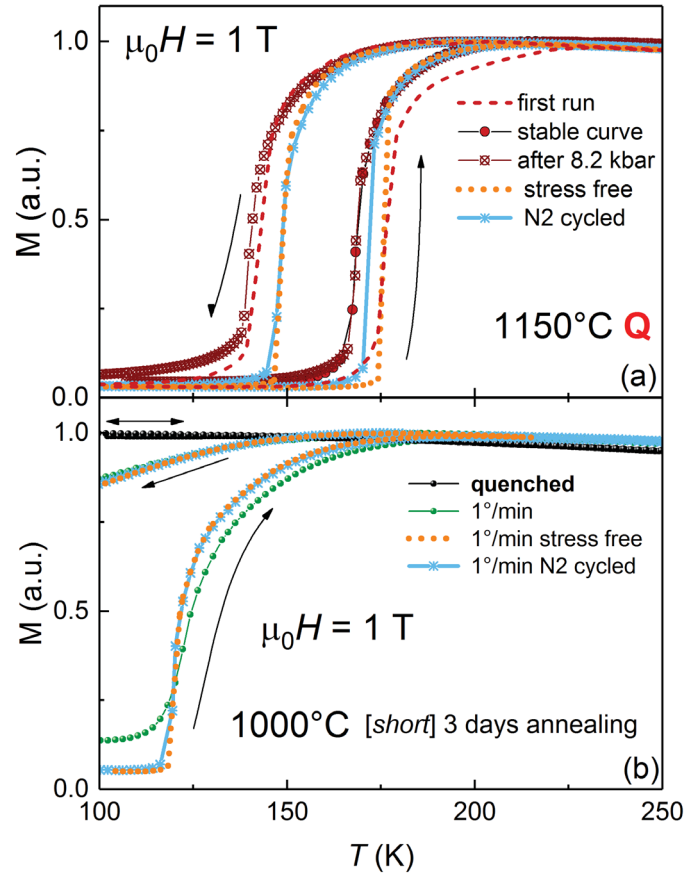


Figure 4.10 Evolution of the magnetostructural transition and hysteresis effect in $(\text{Fe}_{0.965}\text{Ni}_{0.035})_{49}\text{Rh}_{51}$ annealed at 1150°C (a) and in samples annealed at 1000°C (b). Effects of different annealing time and cooling rate can be observed in (b). Stress free 3 h annealing at 450°C and cycling between liquid N_2 and room temperature were applied to observe the reaction of the magnetic state to the thermal history.

to have caused some irreversible changes in the microstructure because the cooling curve shifted lower by almost 10 K and the amount of the retained FM phase increased (Fig. 4.9a, crossed circles). The heating curve, however, remained in the same "stable" place.

Further, the stress free annealing at 450°C (orange dots) returned the AF–FM transition in the quenched sample to the first-run-position, but the heating curve in the slowly cooled sample did not react. Both cooling curves were shifted to higher temperatures, which reduced the hysteresis and also removed the FM fraction in the low temperature state. This effect turned out to be very strong because a subsequent run did not change the transition position. After that, the samples were rapidly cycled between room and liquid nitrogen temperature (blue lines), but, surprisingly, that did not bring any significant changes to the stress-free curves either.

The sample annealed at 1150°C (Fig. 4.10a) showed a similar behavior: the transi-

tion temperature altered comparing the first and the subsequent field application, the cooling curve was also affected by the pressure experiment, and the initial transition temperature was recovered after the stress free heat treatment along with the reduction of the hysteresis. However, in this case the sample turned out to be more susceptible to the thermal shock treatment: the heating curve started shifting towards low temperatures (or in other words, the direction of larger tensile stress) while the cooling curve remained unaffected. Overall, the hysteresis was reduced from 33 K (initial curve) to 23 K after thermal cycles.

The mysterious case of the FM state after a 1000°C annealing was additionally investigated varying the duration of annealing and the cooling rate. Two extra samples were heat treated at 1000°C for 3 days and cooled by 2 different routes: quenching and furnace cooling. The quenched samples, regardless of the duration of the annealing, both became completely FM and did not react to the thermal shock treatment and stress free annealing. They have the same lattice parameters defined from XRD patterns and the same composition from EDX (for that reason in Fig. 4.10b only the sample annealed for 3 days is shown). The only slight difference appears in the degree of order. However, the slowly cooled sample exhibited a transition starting at 118 K on heating. At low temperature this sample had an initial FM fraction that was reduced after tempering (see Fig. 4.10b).

Summarizing the observed effects, the stress free annealing seems to have a strong influence on improving the AF–FM transition in terms of sharpness and reduction of the initial FM fraction, as well as shifting the transition towards higher temperatures which may signify a stress release. Therefore, there can be indeed strain stored in the material after cooling from a high temperature heat treatment. Considering the data of EDX and XRD analysis (Table 2), it is difficult to make any final conclusion what is the reason for the appearance of the FM state and how the cooling rate caused such a difference. One fact that stands out is the lattice parameter of the fcc γ -phase for the slowly cooled sample: it is smaller and the value is closer towards the parameters of the samples annealed at 850°C, so possibly during the slow cooling the γ -phase continues to form with parameters that are different to those at 1000°C. The systematic error of EDX does not allow to establish the composition more accurately than ± 1 at. %, but such a variation would result in significant effects even in the case of binary FeRh. Analysing the observed effects, the obtained parameters and microstructural specifics, one may assume that there is more than one mechanism (strain) affecting the magnetostructural transition, in particular, an effect of chemical composition or ordering. The degree of order is comparable for all quenched binary FeRh alloys, whereas for the Ni-doped alloys (Table 2) some difference can be observed.

4.3 Microstructure of FeRh alloys doped by d-metals

4.3.1 Microscopy, structural and elemental analysis

Due to an insufficient number of microstructural studies on FeRh, it is practically unknown how the phase content looks in the case of FeRh substituted by other *d*-elements. Strong effects on the magnetic behavior considered in the previous sections reveal the importance of the microstructure. Traditionally, when the minor γ -phase is neglected, the assumption is that the change in the behavior of the magnetic transition, usually observed by the change of the transition temperature, is caused by the introduction of other metals into the α' -FeRh lattice, affecting the electronic structure. It is clear though, that, with the presence of a secondary phase, the distribution of the elements may vary from the one expected from the nominal composition, since the γ -phase, as can be concluded from the results on the binary FeRh and Ni-doped FeRh in the previous sections, is Rh-rich and in the ternary case also contains twice as much Ni as the α' -phase.

In order to reveal the phase content and the elemental distribution within FeRh alloys modified by other *d*-metals, some selected pseudobinary FeRh alloys with additions of Cr, Pd, Ru, Re, (Ni, Pt) and (Pd, Pt) were investigated*. Magnetic measurements were combined with the phase analysis by XRD, SEM and EDX**. For all samples a one week heat treatment was performed at 1000°C followed by quenching into water.

The results of this study are summarized in Fig. 4.11 and Fig. 4.12. For each sample, a temperature dependence of magnetization on heating is given, in order to observe the transition temperature, the saturation magnetization and also the sharpness of the transition. The backscattered electron images are presented beside corresponding XRD patterns. The calculated lattice parameters and the results of the EDX analysis are summarized in a table where also the nominal composition values are given. The amount of the minor phase was estimated from quantitative metallography and the obtained amount is given in the tables of Fig. 4.11 and Fig. 4.12 as well.

All samples exhibit a quite different microstructure in terms of morphology, and surprisingly, the actual composition of the magnetic α' -phase is not at all in accordance with the nominal composition (see the tables in Fig. 4.11 and Fig. 4.12). In the case of the Re-doping (Fig. 4.11c), the doping element appears only in the minor γ -phase, both Ru and Cr also show a great preference for the fcc γ -phase. The samples containing Cr and Re were observed to be air sensitive compared to other FeRh-based alloys. There are some peaks of an unknown phase in the XRD pattern of Cr, possibly due to oxidation. Again a discrepancy in the amount of the fcc phase detected by XRD and SEM can be observed, for example, in the case of Cr-doping (Fig. 4.11a). As can be seen from the micrographs, the Pd-doping (Fig. 4.12 a,b) does not result in a large amount of the γ -phase. The

*Synthesized by Prof. Dr. N.V. Baranov, Ural Federal University

**SEM and EDX carried out in IFW Dresden together with Dr. Mikhail Gorshenkov, MISiS

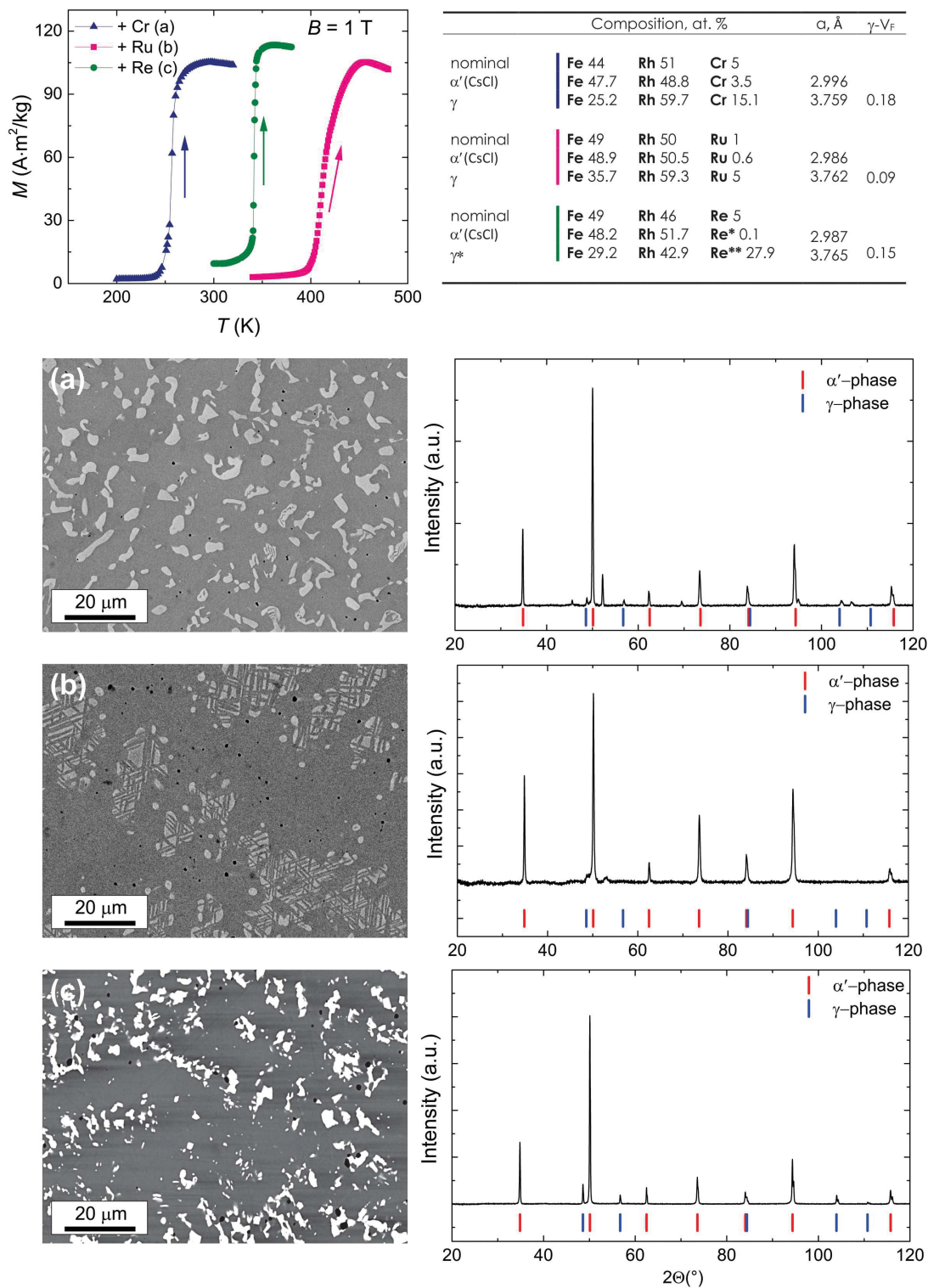


Figure 4.11 Backscattered electron images, temperature dependences of magnetization, XRD and EDX analysis, volume fraction of the fcc phase, as well as the nominal composition of the FeRh alloys doped with Re, Ru and Cr.

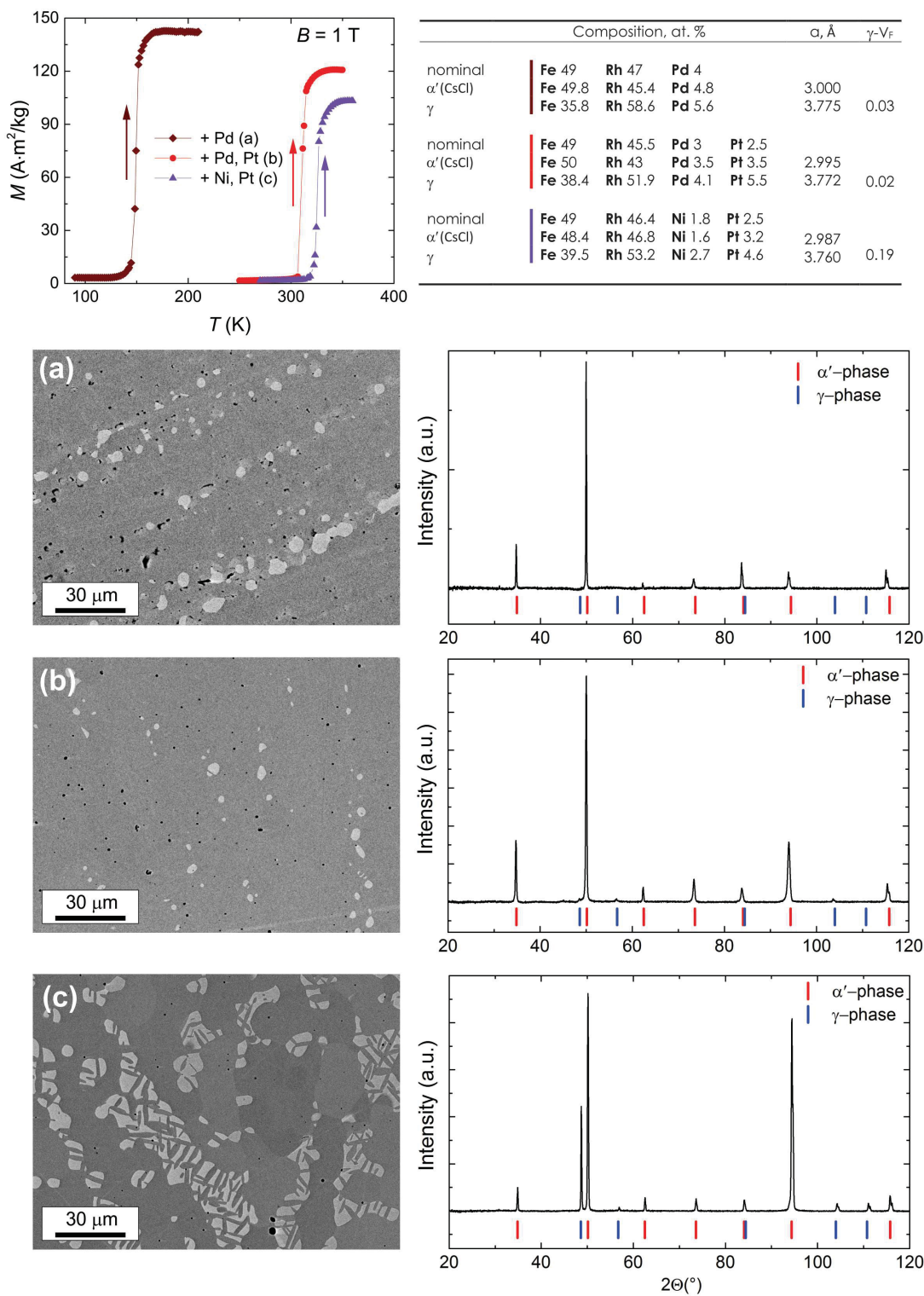


Figure 4.12 Backscattered electron images, temperature dependences of magnetization, XRD and EDX analysis, volume fraction of the fcc phase, as well as the nominal composition of the FeRh alloys doped with Ni, Pt and Pd.

morphology of the microstructure of the samples doped by (Ni, Pt) and Ru (Fig. 4.12c and Fig. 4.11b) is quite different from the globular one observed in other samples, including the binary and Ni-doped cases. The lattice parameters of the magnetic phase are surprisingly similar despite the presence of different doping elements, especially on recalling that at room temperature some alloys will be antiferromagnetic and some are ferromagnetic. It can account for the difference of 0.3 % when comparing the lattice parameters of FeRh alloys with different compositions. The actual difference in the lattice parameter depending on the substituting elements can be investigated further in temperature-controlled XRD setups in order to avoid mixed magnetic states.

4.3.2 Effect on magnetocaloric properties

Temperature dependences of the magnetization measured in magnetic fields up to 2 T have been used to estimate the magnetic entropy at the AF–FM transition (Fig. 4.13). Here and in the previous sections, the calculation was done in the usual way of ignoring the minor phase, i.e. without corrections for its mass (the effect on the magnetization value can be seen in Fig. 4.12 for the case of (Ni, Pt)-doping that has the largest non-magnetic phase fraction). For a comparison, the magnetic entropy of a binary alloy heat treated at 1000°C is also shown. The ΔS value and the shape of the Re-doped sample resemble the binary curve. Essentially, the magnetic α' -matrix is binary because all Re is situated in the fcc γ -phase. The change of the transition temperature must be caused by this fcc phase and the stress fields resulting from it, keeping in mind that it may differ mechanically from the binary γ -phase due to the Re-addition. This effect could be used in experiments concentrating on the mechanical interaction of the two phases because the α' -phase content would have been identical.

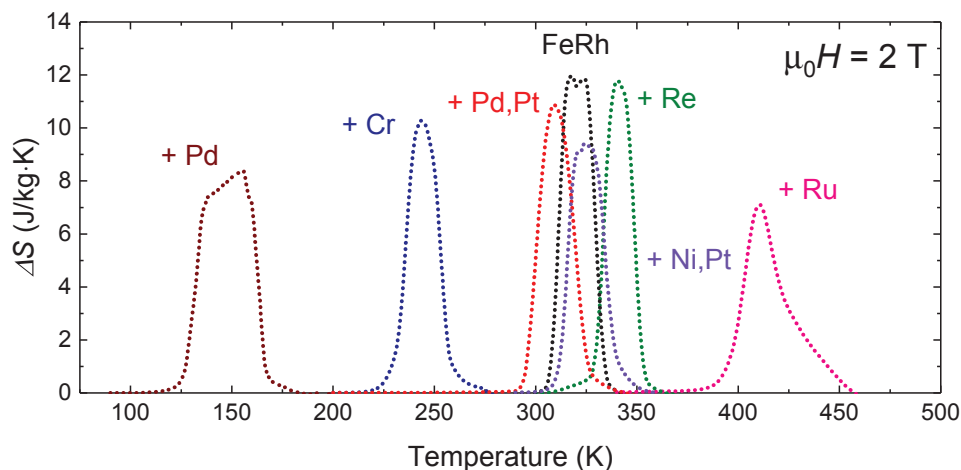


Figure 4.13 Magnetic entropy change in a magnetic field of 2 T for different *d*-metal doped FeRh alloys. The values were calculated using the total mass of the sample, without accounting for the amount of the fcc phase.

Naturally, it is important to account for the minor phase not only to estimate the entropy change occurring in the magnetic phase correctly, but also when building experimental models for both transition temperature and magnetic entropy [9, 107] on the base of average weighted valence band electrons ((s+d) electrons/atom), because until now the data has mostly been treated with the assumption that the nominal composition is the same as the actual one, which is not always the case as is seen from this study.

4.4 Conclusions

A heat treatment of FeRh alloys with a nominal composition of 52 at. % Rh at 850°C-1150°C resulted in a 50 K spread of the AF–FM transition temperature T_{tr} . An investigation by means of SEM and TEM revealed a formation of significantly different microstructures consisting of the paramagnetic γ -phase and the ordered, magnetic α' -phase. No gradient of atomic composition was detected from the phase boundary into the grains of α' - or γ -phase. The α' -phase in all heat treated samples is well ordered chemically and has the same lattice parameter and atomic composition. The microstructure of the samples shows large differences in chemical composition, size, shape and distribution of the γ -phase grains that depend on the annealing temperature. The FEM simulations indicate stress fields of different magnitude, extent and levels of interaction depending on the microstructure of the samples annealed at different temperatures. Depending on the annealing temperature, not only T_{tr} was affected, but also the thermal hysteresis. The lowest value of the thermal hysteresis was obtained for the highest annealing temperature. The heat treatment resulted in the changes of the maximal MCE and its region of reversibility.

A heat treatment of Ni-doped FeRh caused a stronger effect, completely suppressing the magnetostructural transition under certain annealing parameters. The investigation made under hydrostatic pressure combined with thermal shock and stress free heat treatments indicates that the FeRh system is sensitive to microstructural changes, some of them can be reversible and some occur only once. Both the hysteresis and the transition temperature react drastically to thermal treatments of different kind, therefore, these effects open new possibilities for tuning the magnetocaloric properties of materials.

The analysis of FeRh-based samples with an addition of other *d*-metals revealed significant differences in the morphology of microstructure depending on the substituting element. Moreover, EDX results show that the nominal composition and expected content of the doping element can be very different from the actual content in the magnetic matrix. Studies of the FeRh microstructure appear to be critical, since relying on XRD only may result in erroneous conclusions about the phase content. This, in its turn, can lead to wrong assumptions about the exact composition of the magnetic phase: the point which is crucial for the precise theoretical calculations.

SUMMARY AND OUTLOOK

Over 80 years of research on FeRh alloys are accompanied by discrepancies in the data of the AF–FM phase transition reported by different groups. A lack of attention to the heat treatment routes and the microstructural data created a problem with reproducibility of results, which complicates the solution of fundamental questions. As demonstrated in this work, the microstructural studies are crucial for the understanding of the magnetic properties of FeRh alloys. Heat treatment being a powerful instrument to tune the properties, if chosen randomly, can lead to discrepancies in the results obtained by different research groups.

A heat treatment of binary FeRh alloys at temperatures between 850°C and 1150°C for 14 days resulted in a dramatic spread of the transition temperature over 50 degrees. As the annealing temperature rises, the transition temperature falls. A thorough investigation by means of SEM and TEM revealed the formation of significantly different microstructures consisting of the ordered magnetic α' -phase and the minor paramagnetic γ -phase. The α' -phase obtained in all heat treated samples is well ordered chemically and has the same lattice parameters and atomic composition. No gradient of atomic composition was detected from the phase boundary into the grains of α' - or γ -phase. Composition, the lattice parameter, size, shape and distribution of the γ -phase were found to depend on the annealing temperature. As the γ -phase does not undergo a volume change during the metamagnetic transition, but the volume of the surrounding α' -phase changes by $\sim 1\%$, stress fields surrounding the γ -grains are likely to appear during the transition. The FEM simulations indicated that stress fields of different magnitude, extent and interaction would indeed be expected depending on the microstructure of the samples annealed at different temperatures. This mechanism is capable of explaining the observed shift in T_{tr} and the discrepancy of the reported data in the literature.

A further investigation of the heat treatment effect on the samples doped with different d -metals revealed a quite different microstructure depending on the doping element. The AF–FM transition temperature and the maximal entropy change were found to be affected as well. The results of the SEM and EDX investigation show that the amount of the doping element in the nominal composition and in the α' -phase of an annealed

sample can be quite different, redistributing itself between the two phases. Furthermore, in the samples substituted with 1.7 at. % Ni, a certain heat treatment can result in a complete suppression of the metamagnetic transition.

This draws attention to the importance of the microstructure in the case of FeRh alloys and proposes a careful phase analysis based on microscopy in order to determine accurate phase fractions. The γ -phase indeed carries no magnetic contribution but may affect the magnetic state of the investigated α' -phase mechanically, and, therefore, must be included in the analysis of the properties of the material. The microstructure can strongly affect the properties relevant for magnetocaloric research such as the transition temperature, the hysteresis, the maximal magnetic entropy change and the region where the reversible MCE is expected. It reveals a possibility of tuning the hysteresis via the microstructure, for example, by a particular heat treatment or an arranged phase segregation, and thus improve the magnetocaloric properties of a material.

A correct estimation of the large magnetocaloric effect in materials experiencing a first order magnetic transition is important for the development of magnetocaloric refrigerants to be used in solid state cooling. Experiments under cyclic conditions close to those in a potential magnetic refrigerator are necessary in order to avoid the overestimation that happens when only the first application of the magnetic field is considered. It was demonstrated by a quasi-dynamic method of direct measurements of ΔT_{ad} and a conventional determination of ΔS from quasi-static magnetic measurements that in FeRh in the magnetic field of 1.9 T under cyclic conditions accounting for the hysteresis, ΔT_{ad} is reduced to 6.2 K compared to the initial value 9.2 K. The reduced value is still 15 % higher than in Gd, the benchmark magnetocaloric material commonly used in prototypes of magnetic refrigerators. It demonstrates the potential of materials with a first order metamagnetic transition for magnetocaloric applications despite the presence of the hysteresis. The maximal value obtained for FeRh by direct measurements is lower than the maximal value expected from an ideal $H - T$ diagram, the suggestion is that it happens due to a distribution of the transition temperature in grains of the real sample, which lowers the MCE.

Substitution of an FeRh alloy by Ni shifts the transition temperature to 260 K and lowers the initial value of the adiabatic temperature change to 7.1 K, and the value under cycling to 4 K, which is still quite high. Direct measurements under cyclic conditions have proven that the MCE in FeRh-based alloys is reversible, and the reduction of the ΔT_{ad} after the first field application is only about 30%. During measurements in magnetic fields of a different sweep rate, the MCE effect in Ni-doped FeRh showed a dynamical dependence. The origin of this effect can be in the coupling of magnetic, lattice and electronic subsystems and their reaction time to the magnetic field of different rates.

OUTLOOK

- The qualitative effect of *d*-metal substitution for Fe or Rh has been known for a long time, but the exact characterization of the final compound remains challenging. Considerable technological advance brings the equipment that was not available to researchers a few decades ago. However, EDX methods still have an instrumental limitation, either the systematic error exceeding the searched elemental values, the unknown phase distribution measured automatically beneath the visible surface or the sample drift as in STEM. Perhaps other methods, such as high resolution STEM or WDX (Wavelength-dispersive X-ray spectroscopy) could elucidate the distribution of elements in FeRh.
- The phase diagram studies are to be continued: a more detailed investigation of the phase formation in FeRh alloys could be of great significance. This information is relevant not only for the Rh-rich FeRh compounds from the mixed ($\alpha' + \gamma$) region, but probably also for the pure α' -phase, since there were several indications [46, 59, 101] of the fcc precipitation in the FeRh alloys with less than 51 at. % Rh. Now it is clear that the secondary phase is more important for the magnetic properties than it has been believed so far, however, the mechanism of the phase interaction in FeRh is unknown, i.e. the instabilities, defects etc. A direct experimental proof of stress fields and information on the lattice distortions would be highly relevant.
- The understanding of the nature of the magnetocaloric effect in FeRh, or the interaction between magnetic, lattice and electronic subsystems can still be improved. The discussion about the leading roles in the entropy change of a particular subsystem is ongoing, but the analysis of a perfect model can be obstructed due to the lack of information about the microstructure. The macroeffects of a real sample may overrun a finer interaction of idealistic systems. Accounting for that, in the future it should be possible to explain the giant MCE in FeRh, its dynamical behavior and its reversibility.

BIBLIOGRAPHY

- [1] A. Smith, “Who discovered the magnetocaloric effect? Warburg, Weiss, and the connection between magnetism and heat,” *European Phys. J. H* **38**, 507–517 (2013).
- [2] V. K. Pecharsky and K. A. Gschneidner Jr, “Magnetocaloric effect and magnetic refrigeration,” *J. Magn. Magn. Mater.* **200**, 44–56 (1999).
- [3] O. Gutfleisch, T. Gottschall, M. Fries, D. Benke, I. Radulov, K. P. Skokov, H. Wende, M. Gruner, M. Acet, P. Entel, and M. Farle, “Mastering hysteresis in magnetocaloric materials,” *Philos. Trans. R. Soc. A Math. Phys. Eng. Sci.* **374**, 20150308 (2016), 1604.08487 .
- [4] S.A. Nikitin, G. Myalikhgulyev, A.M. Tishin, M.P. Annaorazov, K.A. Asatryan, and A.L. Tyurin, “The magnetocaloric effect in $Fe_{49}Rh_{51}$ compound,” *Phys. Lett. A* **148**, 363–366 (1990).
- [5] L. Muldawer and F. deBergevin, “Antiferromagnetic-ferromagnetic transformation in $FeRh$,” *J. Chem. Phys.* **35**, 1904 (1961).
- [6] X. Marti, I. Fina, C. Frontera, J. Liu, P. Wadley, Q. He, R. J. Paull, J. D. Clarkson, J. Kudrnovský, I. Turek, J. Kuneš, D. Yi, J-H. Chu, C. T. Nelson, L. You, E. Arenholz, S. Salahuddin, J. Fontcuberta, T. Jungwirth, and R. Ramesh, “Room-temperature antiferromagnetic memory resistor,” *Nat. Mater.* **13**, 367–374 (2014).
- [7] R. O. Cherifi, V. Ivanovskaya, L. C. Phillips, A. Zobelli, I. C. Infante, E. Jacquet, V. Garcia, S. Fusil, P. R. Briddon, N. Guiblin, A. Mougin, A. A. Ünal, F. Kronast, S. Valencia, B. Dkhil, A. Barthélémy, and M. Bibes, “Electric-field control of magnetic order above room temperature,” *Nat. Mater.* **13**, 345–51 (2014).
- [8] V. K. Pecharsky and K. A. Gschneidner, “Some common misconceptions concerning magnetic refrigerant materials,” *J. Appl. Phys.* **90**, 4614–4622 (2001).
- [9] R. Barua, F. Jiménez-Villacorta, and L. H. Lewis, “Predicting magnetostructural trends in $FeRh$ -based ternary systems,” *Appl. Phys. Lett.* **103**, 102407 (2013).

-
- [10] D. Kondepudi and I. Prigogine, [Modern thermodynamics](#) (John Wiley & Sons, Ltd, Chichester, UK, 2014).
- [11] B. Fultz, [Phase transitions in materials](#) (Cambridge University Press, Cambridge, 2014).
- [12] V. Franco, J.S. Blázquez, J.J. Ipus, J.Y. Law, L.M. Moreno-Ramírez, and A. Conde, “*Magnetocaloric effect: From materials research to refrigeration devices*,” [Progress in Materials Science](#) **93**, 112–232 (2018).
- [13] J.S. Amaral and V.S. Amaral, “*On estimating the magnetocaloric effect from magnetization measurements*,” [J. Magn. Magn. Mater.](#) **322**, 1552–1557 (2010).
- [14] A. Smith, C.R.H. Bahl, R. Bjork, K. Engelbrecht, K. K. Nielsen, and N. Pryds, “*Materials challenges for high performance magnetocaloric refrigeration devices*,” [Adv. Energy Mater.](#) **2**, 1288–1318 (2012).
- [15] V. Pecharsky, K. Gschneidner, A. Pecharsky, and A. Tishin, “*Thermodynamics of the magnetocaloric effect*,” [Phys. Rev. B](#) **64**, 144406 (2001).
- [16] K. A. Gschneidner Jr, V. K. Pecharsky, and A. O. Tsokol, “*Recent developments in magnetocaloric materials*,” [Reports on Progress in Physics](#) **68**, 1479–1539 (2005).
- [17] P. Papon, J. Leblond, and P. H.E. Meijer, [The physics of phase transitions](#) (Springer Berlin Heidelberg, Berlin, Heidelberg, 2006).
- [18] A.M. Tishin and Y.I. Spichkin, [The magnetocaloric effect and its applications](#) (2003).
- [19] V. Franco and A. Conde, “*Scaling laws for the magnetocaloric effect in second order phase transitions: From physics to applications for the characterization of materials*,” [Int. J. Refrig.](#) **33**, 465–473 (2010).
- [20] V. Franco, J. S. Blazquez, and A. Conde, “*Field dependence of the magnetocaloric effect in materials with a second order phase transition: A master curve for the magnetic entropy change*,” [Appl. Phys. Lett.](#) **89**, 222512 (2006).
- [21] R. Caballero-Flores, V. Franco, A. Conde, and L. F. Kiss, “*Influence of the demagnetizing field on the determination of the magnetocaloric effect from magnetization curves*,” [J. Appl. Phys.](#) **105**, 07A919 (2009).
- [22] C. Romero-Muñiz, J. J. Ipus, J. S. Blázquez, V. Franco, and A. Conde, “*Influence of the demagnetizing factor on the magnetocaloric effect: Critical scaling and numerical simulations*,” [Appl. Phys. Lett.](#) **104** (2014), 10.1063/1.4885110.
-

- [23] V. Franco, R. Caballero-Flores, A. Conde, Q.Y. Dong, and H.W. Zhang, “The influence of a minority magnetic phase on the field dependence of the magnetocaloric effect,” *J. Magn. Magn. Mater.* **321**, 1115–1120 (2009).
- [24] A. Smith, K. K. Nielsen, and C. R. H. Bahl, “Scaling and universality in magnetocaloric materials,” *Phys. Rev. B* **90**, 1–17 (2014).
- [25] J. S. Blázquez, V. Franco, A. Conde, T. Gottschall, K. P. Skokov, and O. Gutfleisch, “A unified approach to describe the thermal and magnetic hysteresis in Heusler alloys,” *Appl. Phys. Lett.* **109**, 122410 (2016).
- [26] O. Tegus, E. Brück, K. H. J. Buschow, and F. R. de Boer, “Transition-metal-based magnetic refrigerants for room-temperature applications.” *Nature* **415**, 150–152 (2002).
- [27] V. Franco, J. Blázquez, B. Ingale, and A. Conde, “The magnetocaloric effect and magnetic refrigeration near room temperature: Materials and models,” *Annu. Rev. Mater. Res.* **42**, 305–342 (2012).
- [28] K. G. Sandeman, “Magnetocaloric materials: The search for new systems,” *Scr. Mater.* **67**, 566–571 (2012).
- [29] J. Liu, T. Gottschall, K. P. Skokov, J. D. Moore, and O. Gutfleisch, “Giant magnetocaloric effect driven by structural transitions,” *Nat. Mater.* **11**, 620–626 (2012).
- [30] J. Lyubina, O. Gutfleisch, M.D. Kuz'min, and M. Richter, “ $La(Fe,Si)_{13}$ -based magnetic refrigerants obtained by novel processing routes,” *J. Magn. Magn. Mater.* **321**, 3571–3577 (2009).
- [31] J. Liu, J.D. Moore, K.P. Skokov, M. Krautz, K. Löwe, A. Barcza, M. Katter, and O. Gutfleisch, “Exploring $La(Fe,Si)_{13}$ -based magnetic refrigerants towards application,” *Scr. Mater.* **67**, 584–589 (2012).
- [32] J. Liu, M. Krautz, K. Skokov, T. G. Woodcock, and O. Gutfleisch, “Systematic study of the microstructure, entropy change and adiabatic temperature change in optimized $LaFeSi$ alloys,” *Acta Mater.* **59**, 3602–3611 (2011).
- [33] V. Franco, K. Pirota, V. Prida, A. Neto, A. Conde, M. Knobel, B. Hernando, and M. Vazquez, “Tailoring of magnetocaloric response in nanostructured materials: Role of anisotropy,” *Phys. Rev. B* **77**, 104434 (2008).
- [34] A. Waske, E. Lovell, A. Funk, K. Sellschopp, A. Rack, L. Giebeler, P. F. Gostin, S. Fähler, and L. F. Cohen, “The impact of surface morphology on the magnetovolume transition in magnetocaloric $LaFe_{11.8}Si_{1.2}$,” *APL Materials* **4** (2016), 10.1063/1.4963840.

-
- [35] V. V. Khovaylo, V. V. Rodionova, S. N. Shevyrtaiov, and V. Novosad, “Magnetocaloric effect in ”reduced” dimensions: Thin films, ribbons, and microwires of Heusler alloys and related compounds,” *Phys. Status Solidi (B)* **251**, 2104–2113 (2014).
- [36] A. Waske, L. Giebeler, B. Weise, A. Funk, M. Hinterstein, M. Herklotz, K. Skokov, S. Fähler, O. Gutfleisch, and J. Eckert, “Asymmetric first-order transition and interlocked particle state in magnetocaloric $\text{La}(\text{Fe},\text{Si})_{13}$,” *Phys. Status Solidi - RRL* **9**, 136–140 (2015).
- [37] E. Lovell, A. M. Pereira, A. D. Caplin, J. Lyubina, and L. F. Cohen, “Dynamics of the first-order metamagnetic transition in magnetocaloric $\text{La}(\text{Fe},\text{Si})_{13}$: Reducing hysteresis,” *Adv. Energy Mater.* **5**, 1–9 (2015).
- [38] M. Krautz, A. Funk, K. P. Skokov, T. Gottschall, J. Eckert, O. Gutfleisch, and A. Waske, “A new type of $\text{La}(\text{Fe},\text{Si})_{13}$ -based magnetocaloric composite with amorphous metallic matrix,” *Scr. Mater.* **95**, 50–53 (2015).
- [39] A. Funk, J. Freudenberger, A. Waske, and M. Krautz, “Getting magnetocaloric materials into good shape: Cold-working of $\text{La}(\text{Fe},\text{Co},\text{Si})_{13}$ by powder-in-tube-processing,” *Mater. Today Energy* **9**, 223–228 (2018).
- [40] J. Lyubina, “Recent advances in the microstructure design of materials for near room temperature magnetic cooling (invited),” *J. Appl. Phys.* **109**, 0–6 (2011).
- [41] T. Gottschall, K. P. Skokov, B. Frincu, and O. Gutfleisch, “Large reversible magnetocaloric effect in Ni-Mn-In-Co ,” *Appl. Phys. Lett.* **106**, 021901 (2015).
- [42] M. Fallot, “Les Alliages du fer avec les métaux de la famille du platine,” *Ann. Phys. (Paris)*. **10**, 291–331 (1938).
- [43] C. C. Chao, “Metastable fcc Fe-Rh alloys and the Fe-Rh phase diagram,” *J. Appl. Phys.* **42**, 4282 (1971).
- [44] H. Okamoto, “Fe-Rh (Iron-Rhodium),” *J. Phase Equilibria Diffus.* **32**, 472–472 (2011).
- [45] L.J. Swartzendruber, “The FeRh (Iron-Rhodium) system,” *Bull. Alloy Phase Diagrams* **5**, 456–462 (1984).
- [46] M. Takahashi and R. Oshima, “Annealing effect on phase transition of equiatomic FeRh alloy,” *Mater. Trans. JIM* **36**, 735–742 (1995).
- [47] O. Kubaschewski, *Iron – Binary phase diagrams* (Springer Science & Business Media, 2013).
-

- [48] I. Ohnuma, T. Gendo, R. Kainuma, G. Inden, and K. Ishida, “Phase equilibria and thermodynamic evaluation approximating short-range ordering energy in the FeRh binary system,” *ISIJ Int.* **49**, 1212–1219 (2009).
- [49] Chloe Baldasseroni, *UC Berkeley Mater. Sci. Eng.*, Ph.D. thesis (2013).
- [50] J. Balun, L. Eleno, and G. Inden, “Phase equilibria in the FeRhTi system I. Experimental results,” *Intermetallics* **15**, 1237–1247 (2007).
- [51] A.I. Zakharov, A.M. Kadomtseva, P.Z. Levitin, and E.G. Ponyatovskii, “Magnetic and magnetoelastic properties of a metamagnetic iron-rhodium alloy,” *J. Exp. Theor. Phys.* **19**, 1348–1353 (1964).
- [52] A.I. Zakharov, “Crystal lattice parameter and structural distortions in Fe-Rh alloy at phase transitions,” *Fiz. Met. i Metalloved.* **24**, 84–90 (1967).
- [53] G. Shirane, C. W. Chen, P. A. Flinn, and R. Nathans, “Hyperfine Fields and Magnetic Moments in the FeRh System,” *J. Appl. Phys.* **34**, 1044–1045 (1963).
- [54] N. Kunitomi, M. Kohgi, and Y. Nakai, “Diffuse scattering of neutrons in the antiferromagnetic phase of FeRh,” *Phys. Lett. A* **37**, 333–334 (1971).
- [55] G. Shirane, R. Nathans, and C.W. Chen, “Magnetic moments and unpaired spin densities in the Fe-Rh alloys,” *Phys. Rev.* **134**, A1547–A1553 (1964).
- [56] M. Gruner, E. Hoffmann, and P. Entel, “Instability of the rhodium magnetic moment as the origin of the metamagnetic phase transition in α -FeRh,” *Physical Review B* **67**, 064415 (2003).
- [57] V. L. Moruzzi and P. M. Marcus, “Antiferromagnetic-ferromagnetic transition in FeRh,” *Phys. Rev. B* **46**, 2864–2873 (1992).
- [58] R. Gu and V. Antropov, “Dominance of the spin-wave contribution to the magnetic phase transition in FeRh,” *Phys. Rev. B* **72**, 012403 (2005).
- [59] M. Castiella, C. Gatel, J. F. Bobo, N. Ratel-Ramond, R. Tan, M. Respaud, and M. J. Casanove, “Structural investigation of magnetic FeRh epitaxial films,” *Mater. Res. Express* **2**, 086401 (2015).
- [60] E.M. Hofer and P. Cucka, “Magnetic properties of Rh-rich FeRh alloy,” *J. Phys. Chem. Solids* **27**, 1552–1555 (1966).
- [61] J. S. Kouvel and C. C. Hartelius, “Anomalous magnetic moments and transformations in the ordered alloy FeRh,” *J. Appl. Phys.* **33**, 1343 (1962).

-
- [62] R. Wayne, "Pressure dependence of the magnetic transitions in Fe-Rh alloys," *Phys. Rev.* **170**, 523–527 (1968).
- [63] J. Ivarsson, G.R. Pickett, and J. Tóth, "The electronic heat capacity of nearly stoichiometric ordered FeRh alloys," *Phys. Lett. A* **35**, 167–168 (1971).
- [64] C. J. Schinkel, R. Hartog, and F. H. A. M. Hochstenbach, "On the magnetic and electrical properties of nearly equiatomic ordered FeRh alloys," *J. Phys. F Met. Phys.* **4**, 1412–1422 (1974).
- [65] J. S. Kouvel, "Unusual Nature of the abrupt magnetic transition in FeRh and its pseudobinary variants," *J. Appl. Phys.* **37**, 1257 (1966).
- [66] P. H. L. Walter, "Exchange inversion in ternary modifications of iron rhodium," *J. Appl. Phys.* **35**, 938 (1964).
- [67] P. Tu, "Mechanism for the first-order magnetic transition in the FeRh system," *J. Appl. Phys.* **40**, 1368 (1969).
- [68] S. Yuasa, Y. Otani, H. Miyajima, and A. Sakuma, "Magnetic properties of bcc FeRh_{1-x}M_x Systems," *IEEE Transl. J. Magn. Japan* **9**, 202–209 (1994).
- [69] N.V. Baranov and E.A. Barabanova, "Electrical resistivity and magnetic phase transitions in modified FeRh compounds," *J. Alloys Compd.* **219**, 139–148 (1995).
- [70] S. Yuasa, M. Nývlt, T. Katayama, and Y. Suzuki, "Exchange coupling of NiFe/FeRhIr thin films," *J. Appl. Phys.* **83**, 6813–6815 (1998).
- [71] L.H. Lewis, C.H. Marrows, and S. Langridge, "Coupled magnetic, structural, and electronic phase transitions in FeRh," *J. Phys. D. Appl. Phys.* **49**, 323002 (2016).
- [72] Y. Khwaja and M. Nauciel-Bloch, "Off-stoichiometry effects in the antiferromagnetic FeRh alloy," *Phys. Status Solidi* **83**, 413–424 (1977).
- [73] J. B. Staunton, R. Banerjee, M. Dos Santos Dias, A. Deak, and L. Szunyogh, "Fluctuating local moments, itinerant electrons, and the magnetocaloric effect: Compositional hypersensitivity of FeRh," *Phys. Rev. B* **89**, 054427 (2014).
- [74] D. Odkhuu, "Magnetization reversal of giant perpendicular magnetic anisotropy at the magnetic-phase transition in FeRh films on MgO," *Phys. Rev. B* **93**, 1–6 (2016).
- [75] S. Polesya, S. Mankovsky, D. Ködderitzsch, J. Minár, and H. Ebert, "Finite-temperature magnetism of FeRh compounds," *Phys. Rev. B* **93**, 024423 (2016), 1509.03581 .
-

-
- [76] P. Kushwaha, P. Bag, R. Rawat, and P. Chaddah, “First-order antiferromagnetic transition in $Fe_{49}(Rh_{0.93}Pd_{0.07})_{51}$ under simultaneous application of magnetic field and external pressure.” *J. Phys. Condens. Matter* **24**, 096005 (2012).
- [77] E.A. Rozenberg and A.V. Chetverikov, “Peculiarities of the fluctuational aftereffect following first order magnetostructural phase transition in $(Fe,Ni)Rh$ alloy,” *J. Magn. Magn. Mater.* **111**, 11–18 (1992).
- [78] M. Manekar and S. B. Roy, “Nucleation and growth dynamics across the antiferromagnetic to ferromagnetic transition in $(Fe_{0.975}Ni_{0.025})_{50}Rh_{50}$: analogy with crystallization,” *J. Phys. Condens. Matter* **20**, 325208 (2008).
- [79] M. Manekar, M. K. Chattopadhyay, and S. B. Roy, “Glassy dynamics in magnetization across the first order ferromagnetic to antiferromagnetic transition in $Fe_{0.955}Ni_{0.045}Rh$,” *J. Phys. Condens. Matter* **23**, 086001 (2011).
- [80] C. Stamm, J.-U. Thiele, T. Kachel, I. Radu, P. Ramm, M. Kosuth, J. Minár, H. Ebert, H. Dürr, W. Eberhardt, and C. Back, “Antiferromagnetic-ferromagnetic phase transition in $FeRh$ probed by x-ray magnetic circular dichroism,” *Phys. Rev. B* **77**, 184401 (2008).
- [81] P. Kushwaha, A. Lakhani, R. Rawat, and P. Chaddah, “Low-temperature study of field-induced antiferromagnetic-ferromagnetic transition in Pd-doped Fe-Rh,” *Phys. Rev. B* **80**, 174413 (2009).
- [82] J. B. McKinnon, D. Melville, and E. W. Lee, “The antiferromagnetic-ferromagnetic transition in iron-rhodium alloys,” *J. Phys. C Solid State Phys.* **3**, S46–S58 (1970).
- [83] V.K. Ponomarev, “Investigation of the antiferro-ferromagnetism transition in an $FeRh$ alloy in a pulsed magnetic field up to 300 kOe,” *J. Exper. Theor. Phys.* **36**, 105–107 (1973).
- [84] L. Pál, G. Zimmer, J. C. Picoch, and T. Tarnóczy, “The magnetic field dependence of the antiferromagnetic-ferromagnetic transition temperature in $FeRh$,” *Acta Phys. Acad. Sci. Hungaricae* **32**, 135–140 (1972).
- [85] M.I. Bartashevich, T. Goto, T. Tomita, N.V. Baranov, S.V. Zemlyanski, G. Hilscher, and H. Michor, “AF–FRI metamagnetic transition in itinerant $Mn_{2x}Co_xSb$ system: high-field and high-pressure effects,” *Phys. B Condens. Matter* **318**, 198–210 (2002).
- [86] J. A. Ricodeau and D. Melville, “Model of the antiferromagnetic-ferromagnetic transition in $FeRh$ alloys,” *J. Phys. F Met. Phys.* **2**, 337–350 (1972).
-

-
- [87] N. V. Baranov, Y. V. Sinitsyn, A. I. Kozlov, and Y. A. Barabanova, “Magnetic phase transitions induced by magnetic field in FeRh-based alloys,” *Fiz. Met. Metalloved.*, 100–106 (1991).
- [88] J-U. Thiele, M. Buess, and C. H. Back, “Spin dynamics of the antiferromagnetic-to-ferromagnetic phase transition in FeRh on a sub-picosecond time scale,” *Appl. Phys. Lett.* **85**, 2857 (2004).
- [89] G. Ju, J. Hohlfeld, B. Bergman, R. van de Veerdonk, O. Mryasov, J-Y. Kim, X. Wu, D. Weller, and B. Koopmans, “Ultrafast generation of ferromagnetic order via a laser-induced phase transformation in FeRh thin films,” *Phys. Rev. Lett.* **93**, 197403 (2004).
- [90] B. Bergman, G. Ju, J. Hohlfeld, R. van de Veerdonk, J-Y. Kim, X. Wu, D. Weller, and B. Koopmans, “Identifying growth mechanisms for laser-induced magnetization in FeRh,” *Phys. Rev. B* **73**, 060407 (2006).
- [91] I. Radu, C. Stamm, N. Pontius, T. Kachel, P. Ramm, J.-U. Thiele, H. A. Dürr, and C. H. Back, “Laser-induced generation and quenching of magnetization on FeRh studied with time-resolved x-ray magnetic circular dichroism,” *Phys. Rev. B* **81**, 104415 (2010).
- [92] F. Quirin, M. Vattilana, V. Shymanovich, A-E. El-Kamhawy, A. Tarasevitch, J. Hohlfeld, D. von der Linde, and K. Sokolowski-Tinten, “Structural dynamics in FeRh during a laser-induced metamagnetic phase transition,” *Phys. Rev. B* **85**, 020103 (2012).
- [93] S. O. Mariager, F. Pressacco, G. Ingold, A. Caviezel, E. Möhr-Vorobeva, P. Beaud, S. L. Johnson, C. J. Milne, E. Mancini, S. Moyerman, E. E. Fullerton, R. Feidenhans'l, C. H. Back, and C. Quitmann, “Structural and magnetic dynamics of a laser induced phase transition in FeRh,” *Phys. Rev. Lett.* **108**, 087201 (2012).
- [94] J. Barker and R. W. Chantrell, “Higher-order exchange interactions leading to metamagnetism in FeRh,” *Phys. Rev. B* **92**, 094402 (2015), 1405.3043 .
- [95] V.L. Moruzzi and P.M. Marcus, “Giant magnetoresistance in FeRh: A natural magnetic multilayer,” *Phys. Rev. B* **46**, 14198–14200 (1992).
- [96] S. Mankovsky, S. Polesya, K. Chadova, H. Ebert, J. B. Staunton, T. Gruenbaum, M. A.W. Schoen, C. H. Back, X. Z. Chen, and C. Song, “Temperature-dependent transport properties of FeRh,” *Phys. Rev. B* **95**, 1–9 (2017).
-

- [97] Y. Kobayashi, K. Muta, and K. Asai, “The Hall effect and thermoelectric power correlated with the giant magnetoresistance in modified FeRh compounds,” *J. Phys. Condens. Matter* **13**, 3335–3346 (2001).
- [98] C. Koenig, “Self-consistent band structure of paramagnetic, ferromagnetic and anti-ferromagnetic ordered FeRh,” *J. Phys. F Met. Phys.* **12**, 1123–1137 (1982).
- [99] A. X. Gray, D. W. Cooke, P. Krüger, C. Bordel, A. M. Kaiser, S. Moyerman, E. E. Fullerton, S. Ueda, Y. Yamashita, A. Gloskovskii, C. M. Schneider, W. Drube, K. Kobayashi, F. Hellman, and C. S. Fadley, “Electronic structure changes across the metamagnetic transition in FeRh via hard X-ray photoemission,” *Phys. Rev. Lett.* **108**, 257208 (2012).
- [100] P. A. Algarabel, M. R. Ibarra, C. Marquina, A. del Moral, J. Galibert, M. Iqbal, and S. Askenazy, “Giant room-temperature magnetoresistance in the FeRh alloy,” *Appl. Phys. Lett.* **66**, 3061 (1995).
- [101] J. van Driel, R. Coehoorn, G. J. Strijkers, E. Brück, and F. R. de Boer, “Compositional dependence of the giant magnetoresistance in Fe_xRh_{1-x} thin films,” *J. Appl. Phys.* **85**, 1026 (1999).
- [102] R. Gómez Abal, A. Llois, and M. Weissmann, “Calculation of the magnetoresistance in RhFe.” *Phys. Rev. B. Condens. Matter* **53**, R8844–R8847 (1996).
- [103] N.V. Baranov, P.E. Markin, S.V. Zemlyanski, H. Michor, and G. Hilscher, “Giant magnetoresistance in antiferromagnetically ordered FeRh and Mn_2Sb based alloys,” *J. Magn. Magn. Mater.* **157-158**, 401–402 (1996).
- [104] K. Kreiner, H. Michor, G. Hilscher, N.V. Baranov, and S.V. Zemlyanski, “Evolution of the electronic specific heat and magnetic order in $(Fe_{1-x}Ni_x)Rh$,” *J. Magn. Magn. Mater.* **177-181**, 581–582 (1998).
- [105] B. Fogarassy, T. Kemény, L. Pál, and J. Tóth, “Electronic specific heat of iron-rhodium and iron-rhodium-iridium alloys,” *Phys. Rev. Lett.* **29**, 288–291 (1972).
- [106] J. M. Lommel, “Thermodynamics of the first-order transition in FeRh,” *J. Appl. Phys.* **40**, 3880–3881 (1969).
- [107] R. Barua, F. Jiménez-Villacorta, and L. H. Lewis, “Towards tailoring the magnetocaloric response in FeRh-based ternary compounds,” *J. Appl. Phys.* **115**, 17A903 (2014).
- [108] S. Inoue and T. Suzuki, “Magnetic properties of single-crystalline FeRh alloy thin films,” *IEEE Trans. Magn.* **44**, 2875–2878 (2008).

-
- [109] D. W. Cooke, F. Hellman, C. Baldasseroni, C. Bordel, S. Moyerman, and E. E. Fullerton, “*Thermodynamic measurements of Fe-Rh alloys*,” *Phys. Rev. Lett.* **109**, 255901 (2012).
- [110] C. Kittel, “*Model of exchange-inversion magnetization*,” *Phys. Rev.* **120**, 335–342 (1960).
- [111] R. Z. Levitin and K. Ponomarev, “*Magnetostriction of the metamagnetic iron-rhodium alloy*,” *J. Exper. Theor. Phys.* , 0–2 (1966).
- [112] M. P. Annaorazov, S. A. Nikitin, A. L. Tyurin, K. A. Asatryan, and A. Kh. Dovletov, “*Anomalously high entropy change in FeRh alloy*,” *J. Appl. Phys.* **79**, 1689 (1996).
- [113] L. M. Sandratskii and P. Mavropoulos, “*Magnetic excitations and femtomagnetism of FeRh: A first-principles study*,” *Phys. Rev. B* **83**, 174408 (2011).
- [114] E. Stern-Taulats, A. Planes, P. Lloveras, M. Barrio, J.-L. Tamarit, S. Pramanick, S. Majumdar, C. Frontera, and L. Mañosa, “*Barocaloric and magnetocaloric effects in Fe₄₉Rh₅₁*,” *Phys. Rev. B* **89**, 214105 (2014).
- [115] W. He, H. Huang, and X. Ma, “*First-principles calculations on elastic and entropy properties in FeRh alloys*,” *Mater. Lett.* **195**, 156–158 (2017).
- [116] P. M. Derlet, “*Landau-Heisenberg Hamiltonian model for FeRh*,” *Phys. Rev. B* **85**, 174431 (2012).
- [117] M. Wolloch, M. E. Gruner, W. Keune, P. Mohn, J. Redinger, F. Hofer, D. Suess, R. Podloucky, J. Landers, S. Salamon, F. Scheibel, D. Spoddig, R. Witte, B. Roldan Cuenya, O. Gutfleisch, M. Y. Hu, J. Zhao, T. Toellner, E. E. Alp, M. Siewert, P. Entel, R. Pentcheva, and H. Wende, “*Impact of lattice dynamics on the phase stability of metamagnetic FeRh: Bulk and thin films*,” *Phys. Rev. B* **94**, 1–17 (2016), 1608.04268 .
- [118] E. Mendive-Tapia and T. Castán, “*Magnetocaloric and barocaloric responses in magnetovolumic systems*,” *Phys. Rev. B* **91**, 224421 (2015).
- [119] V. K. Pecharsky and K. A. Gschneidner, “*Tunable magnetic regenerator alloys with a giant magnetocaloric effect for magnetic refrigeration from ~20 to ~290 K*,” *Appl. Phys. Lett.* **70**, 3299–3301 (1997).
- [120] V.K. Pecharsky and K.A. Gschneidner, Jr., “*Giant magnetocaloric effect in Gd₅(Si₂Ge₂)*,” *Phys. Rev. Lett.* **78**, 4494–4497 (1997).
-

-
- [121] M.P. Annaorazov, K.A. Asatryan, G. Myalikgulyev, S.A. Nikitin, A.M. Tishin, and A.L. Tyurin, “Alloys of the Fe-Rh system as a new class of working material for magnetic refrigerators,” *Cryogenics* **32**, 867–872 (1992).
- [122] A.M. Tishin, Y.I. Spichkin, V.I. Zverev, and P.W. Egolf, “A review and new perspectives for the magnetocaloric effect: New materials and local heating and cooling inside the human body,” *Int. J. Refrig.* **68**, 177–186 (2016).
- [123] M. Manekar and S. B. Roy, “Reproducible room temperature giant magnetocaloric effect in FeRh,” *J. Phys. D. Appl. Phys.* **41**, 192004 (2008).
- [124] K. Nishimura, Y. Nakazawa, L. Li, and K. Mori, “Magnetocaloric effect of $Fe(Rh_{1-x}Pd_x)$ alloys,” *Mater. Trans.* **49**, 1753–1756 (2008).
- [125] S.A. Nikitin, G. Myalikgulyev, M.P. Annaorazov, A.L. Tyurin, R.W. Myndyev, and S.A. Akopyan, “Giant elastocaloric effect in FeRh alloy,” *Phys. Lett. A* **171**, 234–236 (1992).
- [126] Y. Liu, L. C. Phillips, R. Mattana, M. Bibes, A. Barthélémy, and B. Dkhil, “Large reversible caloric effect in FeRh thin films via a dual-stimulus multicaloric cycle,” *Nat. Commun.* **7**, 11614 (2016).
- [127] E.G. Poniatovskiy and A.R. Kutsar, “On the possibility of a peculiar triple point on the p - T diagram of the FeRh alloy [in Russian],” *Cristallography* **12**, 79–83 (1967).
- [128] L.I. Vinokurova, A.V. Vlasov, N.I. Kulikov, and M. Pardavi-Horváth, “Pressure-induced antiferromagnetism in ferromagnetic $Fe_{51.5}Rh_{48.5}$ alloy,” *J. Magn. Magn. Mater.* **25**, 201–206 (1981).
- [129] K. Kamenev, Z. Arnold, J. Kamarád, and N.V. Baranov, “Pressure induced antiferromagnetism in $(Fe_{1-x}Ni_x)_{49}Rh_{51}$ alloys,” *J. Alloys Compd.* **252**, 1–5 (1997).
- [130] K. Kamenev, Z. Arnold, J. Kamarád, and N. V. Baranov, “Pressure induced giant volume magnetostriction in the $(Fe_{1-x}Ni_x)_{49}Rh_{51}$ alloys,” *J. Appl. Phys.* **81**, 5680 (1997).
- [131] V. I. Kamenev, K. V. Kamenev, B. M. Todris, E. A. Zavadskii, V. N. Varyukhin, and N. V. Baranov, “Effect of pressure on magnetic phases of $(Fe_{1-x}Ni_x)_{49}Rh_{51}$,” *High Press. Res.* **23**, 195–199 (2003).
- [132] M.E. Gruner and P. Entel, “Simulation of the (p,T) phase diagram of the temperature-driven metamagnet α -FeRh,” *Phase Transitions* **78**, 209–217 (2005).
- [133] L. Vinokurova and M. Pardavi-Horváth, “Pressure dependence of the magnetic transitions in an FeRhIr Alloy,” *Phys. Status Solidi* **48**, K31–K33 (1971).
-

-
-
- [134] G. T. Dubovka, “Effect of pressure on magnetic transformations in an iron-rhodium alloy,” *J. Exper. Theor. Phys.* **38**, 1140 (1973).
- [135] C. Hargitai, “On the aligned magnetic moment of the Rh atoms in the FeRh alloy,” *Phys. Lett.* **17**, 4–5 (1965).
- [136] L. I. Vinokurova, A. V. Vlasov, and M. Pardavi-Horváth, “Pressure effects on magnetic phase transitions in FeRh and FeRhIr alloys,” *Phys. status solidi* **78**, 353–357 (1976).
- [137] Y. Ohtani and I. Hatakeyama, “Features of broad magnetic transition in FeRh thin film,” *J. Magn. Magn. Mater.* **131**, 339–344 (1994).
- [138] S. Maat, J.-U. Thiele, and E. Fullerton, “Temperature and field hysteresis of the antiferromagnetic-to-ferromagnetic phase transition in epitaxial FeRh films,” *Phys. Rev. B* **72**, 214432 (2005).
- [139] J.P. Ayoub, C. Gatel, C. Roucau, and M.J. Casanove, “Structure and chemical order in FeRh nanolayers epitaxially grown on MgO(001),” *J. Cryst. Growth* **314**, 336–340 (2011).
- [140] C. Bordel, J. Juraszek, D. W. Cooke, C. Baldasseroni, S. Mankovsky, J. Minár, H. Ebert, S. Moyerman, E. E. Fullerton, and F. Hellman, “Fe spin reorientation across the metamagnetic transition in strained FeRh thin films,” *Phys. Rev. Lett.* **109**, 117201 (2012).
- [141] I. Suzuki, T. Koike, M. Itoh, T. Taniyama, and T. Sato, “Stability of ferromagnetic state of epitaxially grown ordered FeRh thin films,” *J. Appl. Phys.* **105**, 07E501 (2009).
- [142] C. W. Barton, T. A. Ostler, D. Huskisson, C. J. Kinane, S. J. Haigh, G. Hrkac, and T. Thomson, “Substrate induced strain field in FeRh epilayers grown on single crystal MgO (001) substrates,” *Sci. Rep.* **7**, 1–9 (2017).
- [143] Y. Ding, D. A. Arena, J. Dvorak, M. Ali, C. J. Kinane, C. H. Marrows, B. J. Hickey, and L. H. Lewis, “Bulk and near-surface magnetic properties of FeRh thin films,” *J. Appl. Phys.* **103**, 07B515 (2008).
- [144] C. Baldasseroni, C. Bordel, A. X. Gray, A. M. Kaiser, F. Kronast, J. Herrero-Albillos, C. M. Schneider, C. S. Fadley, and F. Hellman, “Temperature-driven nucleation of ferromagnetic domains in FeRh thin films,” *Appl. Phys. Lett.* **100**, 262401 (2012).
- [145] T. A. Ostler, C. Barton, T. Thomson, and G. Hrkac, “Modeling the thickness dependence of the magnetic phase transition temperature in thin FeRh films,” *Phys. Rev. B* **95**, 064415 (2017).
-

- [146] J. M. Lommel and J. S. Kouvel, “Effects of mechanical and thermal treatment on the structure and magnetic transitions in FeRh,” *J. Appl. Phys.* **38**, 1263–1264 (1967).
- [147] E. Navarro, M. Multigner, A. R. Yavari, and A. Hernando, “The spin glass state of metastable fcc FeRh,” *Europhys. Lett.* **35**, 307–312 (1996).
- [148] V. Kuncser, R. Nicula, U. Ponkratz, A. Jianu, M. Stir, E. Burkel, and G. Filoti, “Structural phase transition induced in Fe₅₀Rh₅₀ alloys by high pressure,” *J. Alloys Compd.* **386**, 8–11 (2005).
- [149] M. Takahashi and R. Oshima, “Stress induced phase transition of iron-rhodium alloys,” *Le J. Phys. IV* **05**, C8–491–C8–496 (1995).
- [150] K. Aikoh, A. Tohki, S. Okuda, Y. Saitoh, T. Kamiya, T. Nakamura, T. Kinoshita, A. Iwase, and T. Matsui, “Study on ferromagnetic ordering of FeRh thin films induced by energetic heavy ion irradiation by means of X-ray Magnetic Circular Dichroism,” *Nucl. Instr. Methods Phys. Res. Sect. B* **314**, 99–102 (2013).
- [151] N. Fujita, S. Kosugi, Y. Saitoh, Y. Kaneta, K. Kume, T. Batchuluun, N. Ishikawa, T. Matsui, and A. Iwase, “Magnetic states controlled by energetic ion irradiation in FeRh thin films,” *J. Appl. Phys.* **107**, 09E302 (2010).
- [152] N. Fujita, T. Matsui, S. Kosugi, T. Satoh, Y. Saitoh, K. Takano, M. Koka, T. Kamiya, S. Seki, and A. Iwase, “Micrometer-sized magnetic patterning of FeRh films using an energetic ion microbeam,” *Jpn. J. Appl. Phys.* **49**, 060211 (2010).
- [153] S. Kosugi, N. Fujita, T. Matsui, F. Hori, Y. Saitoh, N. Ishikawa, Y. Okamoto, and A. Iwase, “Effect of high temperature annealing on ferromagnetism induced by energetic ion irradiation in FeRh alloy,” *Nucl. Instruments Methods Phys. Res. Sect. B Beam Interact. with Mater. Atoms* **269**, 869–872 (2011).
- [154] V. Rodionov, V. Rodionova, and M. Annaorazov, “Phase transitions in Fe-Rh alloys induced by temperature,” *Acta Phys. Pol. A* **127**, 445–447 (2015).
- [155] J. M. Lommel, “Magnetic and electrical properties of FeRh thin films,” *J. Appl. Phys.* **37**, 1483 (1966).
- [156] J. Cao, N. T. Nam, S. Inoue, H. Y. Y. Ko, N. N. Phuoc, and T. Suzuki, “Magnetization behaviors for FeRh single crystal thin films,” *J. Appl. Phys.* **103**, 07F501 (2008).
- [157] J. Rodríguez-Carvajal, “Recent advances in magnetic structure determination by neutron powder diffraction,” *Phys. B Condens. Matter* **192**, 55–69 (1993).

-
- [158] J.C. Lashley, M.F. Hundley, A. Migliori, J.L. Sarrao, P.G. Pagliuso, T.W. Darling, M. Jaime, J.C. Cooley, W.L. Hults, L. Morales, D.J. Thoma, J.L. Smith, J. Boerio-Goates, B.F. Woodfield, G.R. Stewart, R.A. Fisher, and N.E. Phillips, “Critical examination of heat capacity measurements made on a Quantum Design physical property measurement system,” *Cryogenics* **43**, 369–378 (2003).
- [159] H. Suzuki, A. Inaba, and C. Meingast, “Accurate heat capacity data at phase transitions from relaxation calorimetry,” *Cryogenics* **50**, 693–699 (2010).
- [160] J. Wosnitza, A. D. Bianchi, J. Freudenberger, J. Haase, T. Herrmannsdörfer, N. Kozlova, L. Schultz, Y. Skourski, S. Zherlitsyn, and S. A. Zvyagin, “Dresden pulsed magnetic field facility,” *J. Magn. Magn. Mater.* **310**, 2728–2730 (2007).
- [161] S. Zherlitsyn, A. D. Bianchi, T. Herrmannsdörfer, F. Pobell, Y. Skourski, A. Sytcheva, S. Zvyagin, and J. Wosnitza, “Coil design for non-destructive pulsed-field magnets targeting 100 T,” *IEEE Trans. Appl. Supercond.* **16**, 1660–1663 (2006).
- [162] M. Ghorbani Zavareh, C. Salazar Mejía, A. K. Nayak, Y. Skourski, J. Wosnitza, C. Felser, and M. Nicklas, “Direct measurements of the magnetocaloric effect in pulsed magnetic fields: The example of the Heusler alloy $Ni_{50}Mn_{35}In_{15}$,” *Appl. Phys. Lett.* **106** (2015), 10.1063/1.4913446.
- [163] C. Mudivarthi, S. M. Na, R. Schäfer, M. Laver, M. Wuttig, and A. B. Flatau, “Magnetic domain observations in Fe-Ga alloys,” *J. Magn. Magn. Mater.* **322**, 2023–2026 (2010).
- [164] K. P. Skokov, K. H. Müller, J. D. Moore, J. Liu, A. Yu. Karpenkov, M. Krautz, and O. Gutfleisch, “Influence of thermal hysteresis and field cycling on the magnetocaloric effect in $LaFe_{11.6}Si_{1.4}$,” *J. Alloys Compd.* **552**, 310–317 (2013).
- [165] K. P. Skokov, V. V. Khovaylo, K. H. Müller, J. D. Moore, J. Liu, and O. Gutfleisch, “Magnetocaloric materials with first-order phase transition: thermal and magnetic hysteresis in $LaFe_{11.8}Si_{1.2}$ and $Ni_{2.21}Mn_{0.77}Ga_{1.02}$ (invited),” *J. Appl. Phys.* **111**, 07A910 (2012).
- [166] I. A. Radulov, K. P. Skokov, D. Yu. Karpenkov, T. Gottschall, and O. Gutfleisch, “On the preparation of $La(Fe,Mn,Si)_{13}H_x$ polymer-composites with optimized magnetocaloric properties,” *J. Magn. Magn. Mater.* **396**, 228–236 (2015).
- [167] L. Caron, Z.Q. Ou, T.T. Nguyen, D.T. Cam Thanh, O. Tegus, and E. Brück, “On the determination of the magnetic entropy change in materials with first-order transitions,” *J. Magn. Magn. Mater.* **321**, 3559–3566 (2009).

-
- [168] E. M. Levin, V. K. Pecharsky, and K. A. Gschneidner, “Unusual magnetic behavior in $Gd_5(Si_{1.5}Ge_{2.5})$ and $Gd_5(Si_2Ge_2)$,” *Phys. Rev. B* **62**, R14625–R14628 (2000).
- [169] V. V. Khovaylo, K. P. Skokov, O. Gutfleisch, H. Miki, T. Takagi, T. Kanomata, V. V. Koledov, V. G. Shavrov, G. Wang, E. Palacios, J. Bartolomé, and R. Burriel, “Peculiarities of the magnetocaloric properties in Ni-Mn-Sn ferromagnetic shape memory alloys,” *Phys. Rev. B* **81**, 214406 (2010).
- [170] N. A. Zarkevich and D. D. Johnson, “FeRh ground state and martensitic transformation,” *Phys. Rev. B* **97**, 014202 (2018), 1710.04199 .
- [171] A.M. Chirkova, A.S. Volegov, D.S. Neznakhin, E.A. Stepanova, and N.V. Baranov, “Pressure induced AF - F - AF magnetic phase transformations in Pd substituted FeRh compound,” *Solid State Phenom.* **190**, 299–302 (2012).
- [172] R. Mahendiran, A. Maignan, S. Hébert, C. Martin, M. Hervieu, B. Raveau, J. Mitchell, and P. Schiffer, “Ultrasharp magnetization steps in perovskite manganites,” *Phys. Rev. Lett.* **89**, 286602 (2002).
- [173] V. Hardy, S. Majumdar, M. Lees, D. Paul, C. Yaicle, and M. Hervieu, “Power-law distribution of avalanche sizes in the field-driven transformation of a phase-separated oxide,” *Phys. Rev. B* **70**, 104423 (2004).
- [174] S. Nishihara, W. Doi, H. Ishibashi, Y. Hosokoshi, X. M. Ren, and S. Mori, “Appearance of magnetization jumps in magnetic hysteresis curves in spinel oxide FeV_2O_4 ,” *J. Appl. Phys.* **107**, 7–10 (2010).
- [175] L. V. B. Diop, O. Isnard, and J. Rodríguez-Carvajal, “Ultrasharp magnetization steps in the antiferromagnetic itinerant-electron system $LaFe_{12}B_6$,” *Phys. Rev. B* **93**, 014440 (2016).
- [176] L. V. B. Diop and O. Isnard, “Giant spontaneous magnetization jumps in $LaFe_{12}B_6$,” *Appl. Phys. Lett.* **108**, 132401 (2016).
- [177] L. V. B. Diop and O. Isnard, “Multiple magnetization steps and plateaus across the antiferromagnetic to ferromagnetic transition in $La_{1-x}Ce_xFe_{12}B_6$: Time delay of the metamagnetic transitions,” *Phys. Rev. B* **97**, 014436 (2018).
- [178] A. Handstein, D. Eckert, K.-H. Müller, B. Wall, and W. Rodewald, “Jumps of magnetic polarization in Sm_2Co_{17} -based magnets,” *IEEE Trans. Magn.* **30**, 598–600 (1994).
- [179] D. S. Neznakhin, A. S. Bolyachkin, A. S. Volegov, P. E. Markin, S. V. Andreev, and N. V. Kudrevatykh, “Magnetization jumps in nanostructured Nd-Fe-B alloy at low temperatures,” *J. Magn. Magn. Mater.* **377**, 477–479 (2015).
-

-
-
- [180] H.-B. Braun, J. Kyriakidis, and D. Loss, “Macroscopic quantum tunneling of ferromagnetic domain walls,” *Phys. Rev. B* **56**, 8129–8137 (1997).
- [181] N.V. Baranov, E.V. Sinitsyn, E.A. Ignatyev, and S.V. Andreev, “Magnetization reversal of Nd-Fe-B sintered magnets at low temperatures,” *J. Magn. Magn. Mater.* **130**, 133–137 (1994).
- [182] V. Hardy, S. Hébert, A. Maignan, C. Martin, M. Hervieu, and B. Raveau, “Staircase effect in metamagnetic transitions of charge and orbitally ordered manganites,” *J. Magn. Magn. Mater.* **264**, 183–191 (2003), 0303610 [cond-mat] .
- [183] M. G. Ghorbani-Zavareh, Y. Skourski, K.P. Skokov, D.Yu. Karpenkov, L. Zvyagina, A. Waske, D. Haskel, M. Zhernenkov, J. Wosnitza, and O. Gutfleisch, “Direct measurement of the magnetocaloric effect in $\text{La}(\text{Fe},\text{Co},\text{Si})_{13}$ compounds in pulsed magnetic fields,” *Phys. Rev. Appl.* **8**, 014037 (2017).
- [184] R.Z. Levitin, V.V. Snegirev, A.V. Kopylov, A.S. Lagutin, and A. Gerber, “Magnetic method of magnetocaloric effect determination in high pulsed magnetic fields,” *J. Magn. Magn. Mater.* **170**, 223–227 (1997).
- [185] T. Gottschall, K. P. Skokov, F. Scheibel, M. Acet, M. Ghorbani Zavareh, Y. Skourski, J. Wosnitza, M. Farle, and O. Gutfleisch, “Dynamical effects of the martensitic transition in magnetocaloric Heusler alloys from direct ΔT_{ad} measurements under different magnetic-field-sweep rates,” *Phys. Rev. Appl.* **5**, 1–8 (2016).
- [186] F. Scheibel, T. Gottschall, K. Skokov, O. Gutfleisch, M. Ghorbani-Zavareh, Y. Skourski, J. Wosnitza, Ö. Çakır, M. Farle, and M. Acet, “Dependence of the inverse magnetocaloric effect on the field-change rate in Mn_3GaC and its relationship to the kinetics of the phase transition,” *J. Appl. Phys.* **117**, 233902 (2015).
- [187] P. Kushwaha, A. Lakhani, R. Rawat, and P. Chaddah, “Influence of thermal annealing and magnetic field on first order magnetic transition in Pd substituted FeRh,” *J. Phys. Conf. Ser.* **200**, 032038 (2010).
- [188] N. V. Baranov, S. V. Zemlyanski, and K Kamenev, “Electrical Resistivity and Phase Transitions in FeRh Based Compounds: Influence of Spin Fluctuations,” in *Itiner. Electron Magn. Fluct. Eff.*, Vol. 55 (Springer Netherlands, Dordrecht, 1998) pp. 345–351.
- [189] A. Hubert and R. Schäfer, *Magnetic domains: the analysis of magnetic microstructures* (Springer Science & Business Media, 2008).

OWN PUBLICATIONS

N. Pérez, **A. Chirkova**, K.P. Skokov, T.G. Woodcock, O. Gutfleisch, N.V. Baranov, K. Nielsch, and G. Schierning, *Thermoelectric determination of electronic entropy change in Ni-doped FeRh*, submitted.

A. Chirkova, F. Bittner, K. Nenkov, N.V. Baranov, L. Schultz, K. Nielsch, T.G. Woodcock, *The effect of the microstructure on the antiferromagnetic to ferromagnetic transition in FeRh alloys*, Acta Materialia **131**, 31 (2017).

A. Chirkova, K. P. Skokov, L. Schultz, N. V. Baranov, O. Gutfleisch, and T. G. Woodcock, *Giant adiabatic temperature change in FeRh alloys evidenced by direct measurements under cyclic conditions*, Acta Materialia **106**, 15 (2016).

A.D. Shishkin, A. V. Proshkin, N. V. Selezneva, E. G. Gerasimov, P. B. Terentev, **A. Chirkova**, K. Nenkov, L. Schultz, and N. V. Baranov, *Effect of rapid quenching on the magnetic state, electrical resistivity and thermomagnetic properties of Gd₃Co*, Journal of Alloys and Compounds **647**, 481 (2015).

A.M. Chirkova, A.S. Volegov, D.S. Neznakhin, E.A. Stepanova, N.V. Baranov, *Pressure Induced AF - F - AF Magnetic Phase Transformations in Pd substituted FeRh compound*, Solid State Phenomena **190**, 299 (2012).

ACKNOWLEDGMENTS

This work could not be completed without precious contributions of different kinds from many people. I would like to thank all who contributed to my research and from whom I learned, all who believed in me and saw the successful ending of this undertaking.

I am deeply grateful to Prof. Dr. Ludwig Schultz for accepting me in the Institute for Metallic Materials of IFW Dresden, his agreement to supervise my doctoral study and permanent support. The time spent in the group of Dr. Thomas G. Woodcock helped me establish a solid foundation for understanding the connection of microstructure and magnetic properties, and I am grateful for Tom's advice, patience and protection during my PhD, as well as the scientific collaboration and sharing his knowledge and experience. I thank Prof. Dr. Nikolai V. Baranov for sparking an initial interest towards the magnetic refrigeration and FeRh alloys, as well as teaching me the fundamentals and supporting me along the whole scientific path.

I had a good time in the Magnetic Materials group and benefited greatly from communication with Dr. Torsten Mix and Dr. Florian Bittner, who were helping me out in science and organization. I appreciate the scientific interest and advice from Dr. Juliane Thielsch, her optimism and brightness. I thank the technicians of Magnetic Materials who were always ready to help: Bernhard Gebel, Monika Herrich and Kerstin Pittruff, and in particular, Katja Berger for her excellence and scientific approach in sample preparation and microscopy. Many thanks to Dr. Konstantin Nenkov for his assistance with magnetic measurements and his good mood. I am very appreciative of Dr. Mikhail Gorshenkov who inspired me for one section of the chapter on microstructure during his stay in the group. I am extremely thankful for the support and encouragement of Dr. Karl-Hartmut Müller, and his knowledge and stories – very happy to have met him.

I do appreciate the extension of my stay at IFW provided by Prof. Dr. Kornelius Nielsch, as well as his attention to my progress and attempts to accelerate it.

I am very grateful to Prof. Dr. Victorino Franco for agreeing to be the referee of my thesis: in 2010 attending his talk on the magnetocaloric effect in my home town, I could not imagine that one day he will review my PhD work. I really enjoyed attending the lectures of Prof. Dr. Werner Skrotzki, and I thank him for being one of the examiners.

I thank from the heart Prof. Dr. Oliver Gutfleisch for the generous introduction in his group at the final stage of my work, Dr. Konstantin Skokov for his constant excitement about science, efficient collaboration and making papers happen, and also the awesome Functional Materials team.

Many thanks to Dr. Yurii Skourski for his scientific expertise, nice collaboration at Helmholtz-Zentrum Dresden-Rossendorf and his great sense of humour.

I am grateful for the opportunity to be a part of MACS group – I thank Dr. Anja Waske and Dr. Maria Krautz for the interest in my research, their support was much appreciated; Alexander Funk and Bruno Weise for sharing their expertise and opinion and discussing my results. Many thanks to Alex for inspiring the liquid nitrogen experiment and for his kind heart.

For introduction and intensive discussions on the difficult and interesting topic of magnetic domains, many thanks to Prof. Dr. Rudolf Schäfer and Dr. Ivan Soldatov. I also thank Ivan for being supportive beyond expectations during the tough time of writing my thesis and for discussing universal matters.

Very grateful to Dr. Olga Shuleshova and Dr. Ivan Kaban for catching me on the last stage and allowing me to complete my transformation. Many thanks to Olga for sharing her knowledge on the solidification processes, excellent explanations, awesome experiments with the electromagnetic levitation, ongoing collaboration, great resourcefulness and possibility of looking deeper into the topic of FeRh in the future.

I am thankful to meet Dr. Yulia Krupskaya who supervised my stay with a DAAD scholarship prior to my enrollment as a PhD student and took care of me in the beginning of my stay at IFW. Beside that, I thank her and Margarita Iakovleva for the activity going beyond work. I thank Dr. Ksenia Zhuravleva for sharing her experience about life and science, her amazing stories, creativity and introducing me to photography.

I would like to heartfully thank everyone who shared their knowledge and expertise and spent their time on the problems of FeRh: Dr. Wolfgang Löser, Dr. Sabine Wurmehl, Dr. Anja Wolter-Giraud, Dr. Lars Giebeler and Dr. Sebastian Fähler. I additionally thank Dr. Fähler for allowing me to try the thin film production, and so fulfilling my dream about going nanoscale with FeRh. I thank Almut Pöhl for her dedication during the preparation of my TEM sample, and Dr. Bernd Rellinghaus for helping us to get started.

The suggestions received from those who read this work in parts or completely were greatly appreciated and paid a lot of attention.

Last but not least, many thanks to the scientists from Institute of Natural Sciences and Mathematics (UrFU): Dr. Dmitry Zaitsev, Dr. Alexey Volegov and Dr. Dmitry Neznakhin for being open to discussions and experimenting, support, vigour and optimism.

Finally, from all my heart I thank my dear family and close friends for their invaluable support and faith.

VERSICHERUNG

Hiermit versichere ich, Alisa Chirkova, geboren am 09.02.1986 in Jekaterinburg (Russland), in Rahmen meines Promotionsverfahrens an der Fakultät Mathematik und Naturwissenschaften der Technischen Universität Dresden, dass

- ich die vorliegende Arbeit ohne unzulässige Hilfe Dritter und ohne Benutzung anderer als der angegebenen Hilfsmittel angefertigt habe; die aus fremden Quellen direkt oder indirekt übernommenen Gedanken sind als solche kenntlich gemacht. Die Arbeit wurde bisher weder im Inland noch im Ausland in gleicher oder ähnlicher Form einer anderen Prüfungsbehörde vorgelegt.
- ich die vorliegende Arbeit am Leibniz-Institut für Festkörper- und Werkstoffforschung unter der wissenschaftlichen Betreuung von Prof. Dr. Ludwig Schultz, angefertigt habe.
- mir die geltende Promotionsordnung (Stand 23.02.2011, Fakultät Mathematik und Naturwissenschaften der TU Dresden) bekannt ist und ich diese anerkenne.

Alisa Chirkova
Dresden, den 01.10.2018